

Diameter Dependence of Transport through Nuclear Pore Complex Mimics Studied Using Optical Nanopores

Nils Klughammer^{1†}, Anders Barth^{1†}, Maurice Dekker², Alessio
Fragasso^{1§}, Patrick R. Onck², Cees Dekker^{1*}

***For correspondence:**

c.dekker@tudelft.nl (CD)

[†]These authors contributed
equally to this work.

Present address:

[§]Department of Biology and
Institute of Chemistry,
Engineering and Medicine for
Human Health, Stanford
University, Palo Alto, CA 94305,
USA

¹Department of Bionanoscience, Kavli Institute of Nanoscience, Delft
University of Technology, Van der Maasweg 9, 2629 HZ, Delft, The
Netherlands; ²Zernike Institute for Advanced Materials, University of
Groningen, Groningen, The Netherlands

Abstract

The nuclear pore complex (NPC) regulates the selective transport of large biomolecules through the nuclear envelope. As a model system for nuclear transport, we construct NPC mimics by functionalizing the pore walls of freestanding palladium zero-mode waveguides with the FG-nucleoporin Nsp1. This approach enables the measurement of single-molecule translocations through individual pores using optical detection. We probe the selectivity of Nsp1-coated pores by quantitatively comparing the translocation rates of the nuclear transport receptor Kap95 to the inert probe BSA over a wide range of pore sizes from 35 nm to 160 nm. Pores below 55 ± 5 nm show significant selectivity that gradually decreases for larger pores. This finding is corroborated by coarse-grained molecular-dynamics simulations of the Nsp1 mesh within the pore, which suggest that leakage of BSA occurs by diffusion through transient openings within the dynamic mesh. Furthermore, we experimentally observe a modulation of the BSA permeation when varying the concentration of Kap95. The results demonstrate the potential of single-molecule fluorescence measurements on biomimetic NPCs to elucidate the principles of nuclear transport.

Introduction

The nuclear pore complex (NPC) forms the sole connection across the nuclear envelope that regulates all transport between the cytoplasm and nucleus. The central channel of this large protein complex (52 MDa in yeast to about 120 MDa in humans, *Reichelt et al. (1990); Kim et al. (2018)*) is lined with intrinsically disordered proteins that are rich in phenylalanine–glycine (FG) repeats, termed FG-Nups. The central transporter mesh constituted by these FG-Nups forms a selective barrier that facilitates the transport of dedicated nuclear transport receptors while blocking other proteins (*Kim et al., 2018*). Recently, it has been discovered that the inner diameter of the central transporter is variable and can dilate from 40 nm to 70 nm under different stress conditions (*Zimmerli et al., 2021; Akey et al., 2022*). How NPC dilation affects the efficiency and selectivity of nuclear transport remains an open question.

Despite extensive structural knowledge of the NPC scaffold, the mechanism of the selective barrier formed by the disordered FG-Nups remain highly debated (*Lim et al., 2015; Schmidt and Görlich, 2016; Jovanovic-Talisman and Zilman, 2017*). Remarkably, the NPC poses this selective barrier while enabling very high transport rates of ~1000 molecules per second that traverse the pore, referred to as the ‘transport paradox’ (*Beck and Hurt, 2017*). Whereas small molecules pass through the NPC channel without much obstruction, translocation of larger biomolecules is increasingly hindered and effectively blocked above a diameter of ~5 nm or a mass of ~30 kDa to 40 kDa unless they specifically interact with the FG-Nups mesh (*Schmidt and Görlich, 2016; Mohr et al., 2009; Keminer and Peters, 1999*). The efficient transport of large cargoes that carry a nuclear localization signal is facilitated by nuclear transport receptors (NTRs) which engage in multivalent interactions with the FG-repeats in the central transporter (*Aramburu and Lemke, 2017*). One of the most studied systems is the Kap95–Kap60 system in yeast (Imp β –Imp α in humans), responsible for the import of proteins into the nucleus (*Görlich and Kutay, 1999*).

Over the years, many models have been proposed to explain the selective properties of the central transporter, often originating from in vitro studies of isolated FG Nups (*Rout et al., 2003; Frey et al., 2006; Frey and Görlich, 2007; Yamada et al., 2010; Schleicher et al., 2014; Kapinos et al., 2014, 2017*). Following early models that explained the selectivity solely based on the properties of the FG Nups, more recent ‘Kap-centric’ models suggested a central role of NTRs as an active component of the selective barrier (*Schleicher et al., 2014; Kapinos et al., 2014, 2017; Fragasso et al., 2022*), supported by the presence of a large amount of strongly interacting transport receptors within the central transporter that engage in multivalent interactions with the FG repeats (*Kim et al., 2018*). This ‘slow phase’ is essentially immobile due to the high affinity of NTRs to the FG-Nup mesh. As the

66 FG-mesh is saturated with NTRs, a mobile phase of NTRs emerges that is thought to diffuse
67 along dedicated channels (*Schleicher et al., 2014*). So far, however, the dependence of
68 transport rates and selectivity on the concentration of NTRs has hardly been studied
69 directly.

70 Much research on the transport mechanism is carried out using in vitro experiments,
71 since direct studies on the native NPC in its full complexity remain challenging. Using
72 minimal biomimetic systems, it has been shown that a selective barrier with similar prop-
73 erties as the native NPC can be reconstituted using even a single native FG-Nup (*Frey
74 and Görlich, 2007; Jovanovic-Talisman et al., 2008; Kowalczyk et al., 2011; Ananth et al.,
75 2018; Celetti et al., 2019*) or artificial mimics thereof (*Fragasso et al., 2021; Ng et al.,
76 2021*). Probing translocations through the FG-Nup mesh using solid-state nanopores
77 grafted with FG-Nups was pioneered by *Jovanovic-Talisman et al. (2008)* using optical
78 detection of fluorescently tagged molecules. However, this approach was limited to bulk
79 measurements of transport through porous membranes that contained many such pores
80 in parallel, thus lacking single-pore and single-molecule resolution. This limitation was
81 subsequently addressed by measuring the electric current through individual functional-
82 ized SiN_x nanopores (*Kowalczyk et al., 2011; Ananth et al., 2018; Fragasso et al., 2021*).
83 While this approach offers single-molecule sensitivity, the current-based readout remains
84 unspecific (i.e. cannot distinguish different proteins), requires the application of a bias
85 voltage which may influence the transport rate and speed of the translocations, and offers
86 limited signal-to-noise ratio. It remains therefore restricted to pore sizes around 30 nm
87 to 50 nm where the translocation of single molecules leads to a detectable current drop.
88 For larger pores, the relative current blockage caused by a translocating molecule is too
89 small compared to the noise, while the conductance of smaller coated pores is too low to
90 detect translocation events.

91 Here, we implement a fluorescence-based assay for the multiplexed detection of single-
92 molecule translocations through solid-state metal nanopores made of palladium, based
93 on our previous work (*Klughammer and Dekker, 2021*). The translocation of individual
94 molecules that were fluorescently labeled in multiple colors is monitored by a focused
95 laser beam at a single nanopore which selectively excites molecules that exit from the
96 pore (*Figure 1 A*). The <200 nm nanopores act as zero-mode waveguides (ZMW, *Levene
97 et al. (2003)*) that block the propagation of the 485 nm to 640 nm wavelength excitation
98 light through the metal membrane. Notably, this method does not require a bias voltage
99 as it relies solely on the free diffusion of the fluorescent molecules, nor does the detection
100 efficiency depend on the pore diameter. We developed robust protocols for efficient
101 passivation of open pores and functionalization of the palladium surface with the FG-Nup
102 Nsp1 to build a functional NPC mimic. After establishing a baseline for the translocation

of fluorescently labeled proteins through open pores, we probe the selectivity of the biomimetic NPCs over a range of pore diameters from 35 nm to 160 nm by comparing the event rates of the transporter Kap95 to that of the inert probe BSA. We find that the selectivity of Nsp1-coated pores decreases with pore diameter, with the main loss of selectivity happening at about a diameter of 55 nm. We observe that smaller pores were selective, because Kap95 proteins can efficiently cross the pore while BSA transport is hindered. For larger pores, transport selectivity is gradually lost as both Kap95 and BSA were observed to cross the pore. Coarse-grained molecular dynamics simulations reproduce these experimental findings and show that the loss of selectivity is due to the formation of voids within the Nsp1 mesh of comparable size to BSA molecules. Upon increasing the concentration of the transporter Kap95 in the experiment, we observe a moderate increase of the transport selectivity for pores with a diameter below 50 nm. Intriguingly, we find that the event rate of BSA translocations for large pores *increases* with Kap95 concentration, suggesting that filling the FG-Nup mesh with NTRs reduces the selective volume. These results highlight the potential of our approach to unravel the physical principles underlying nuclear transport.

Results

Fabrication, surface grafting, and measurement setup

Our experimental approach is based on a free-standing palladium membrane into which nanopores were drilled using focused ion beam (FIB) milling (**Figure 1 B**). Fabrication of the metal membranes was achieved by evaporating a layer of Pd onto a SiN_x membrane (20 nm thickness) that was subsequently removed by reactive ion etching (in a process that was slightly adapted from **Klughammer and Dekker (2021)**, see section **Fabrication of freestanding Pd ZMWs** for details). After processing, the Pd membrane had a thickness of ≈90 nm. To functionalize the metal surface we applied standard thiol chemistry which is well established for metals such as gold or palladium (**Love et al., 2003; Jiang et al., 2004**). After the FIB-milling step, a cleaning step was required to remove impurities from the Pd surface prior to thiol binding to ensure efficient surface grafting. Since previous protocols relied on freshly prepared surfaces, we developed a gentle cleaning protocol that used either hydrogen peroxide or boiling ethanol, inspired by **Majid et al. (2003)** (see **Methods and Appendix 1**). The cleaning step ensured that the Pd surface was competent for thiol binding, as validated by quartz crystal microbalance with dissipation monitoring (QCM-D) experiments (see **Appendix 1**—**Figures 1–3**) and surface plasmon resonance measurements (**Andersson et al., 2022**). We additionally confirmed that the cleaning procedure does not alter the pore shape or closes the pores by transmission electron

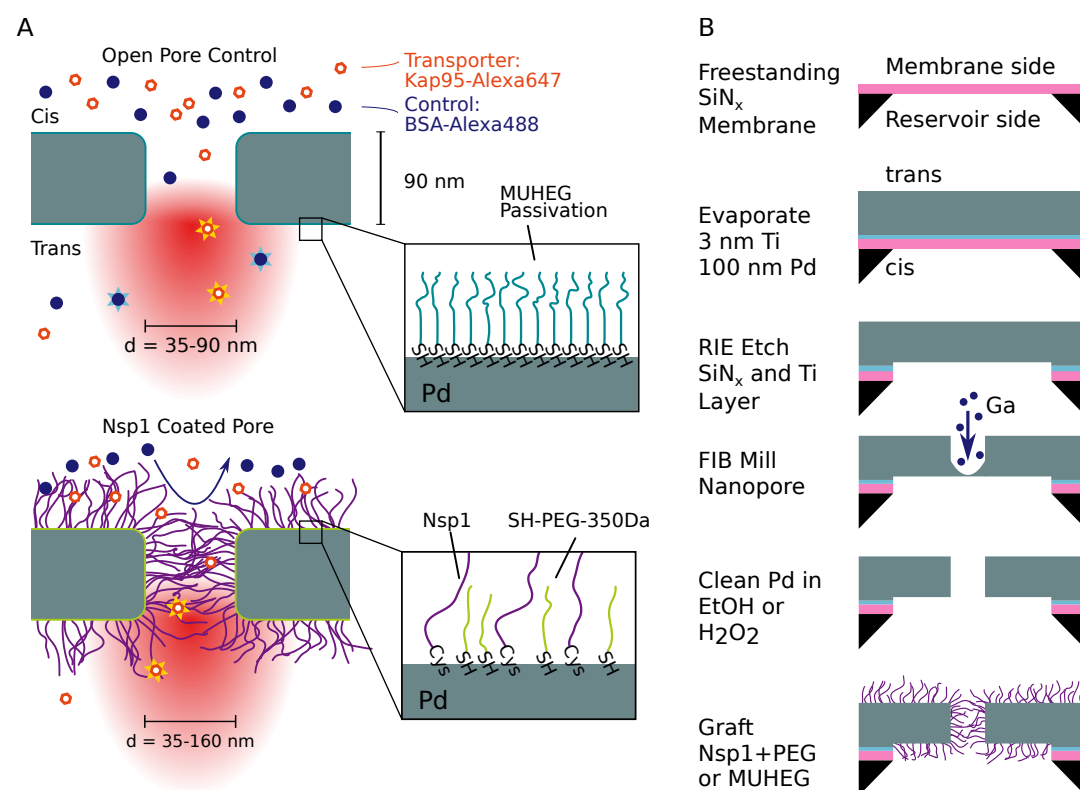


Figure 1. Experimental principle and nanofabrication. (A) Sketch of the experimental principle. Nanopores in a metal membrane block light from traversing if the pore diameter is small compared to the wavelength of light. The selectivity of Nsp1-coated metal nanopores is probed by measuring the translocation rate of fluorescently labeled proteins from the top reservoir (cis) to the detection (trans) side, where they rapidly diffuse out of the laser focus. Measurements on open pores (top) serve as a control where both the NTR Kap95 and the inert protein probe BSA pass unhindered. Nsp1-coated pores are expected to block the translocation of BSA while still allowing Kap95 to translocate. Zooms at bottom right illustrate the passivation of open pores with MUHEG (top) and functionalization of the palladium surface with the FG-nucleoporin Nsp1 and 350 Da SH-PEG (bottom), achieved via thiol-palladium chemistry. (B) Fabrication of nanopores in a free-standing palladium membrane was performed by physical vapor deposition of palladium onto silicon nitride (SiN_x), reactive ion etching (RIE), and focused-ion-beam (FIB) milling of the nanopores. The palladium surface was then cleaned either with H_2O_2 or ethanol to remove contaminants before the functionalization step.

138 microscopy (TEM), cf. images shown at *Klughammer et al. (2023b)*).

139 To prevent unspecific sticking of proteins to the metal surface, the control open pores
140 were passivated using 1-mercaptopundec-11-yl)hexa(ethylene glycol) (MUHEG), which
141 forms a self-assembled monolayer by thiol-Pd binding enhanced with a dense packing due
142 to the hydrophobic interactions between the alkane groups while providing a hydrophilic
143 surface through the terminal hexaethylene glycol groups (*Prime and Whitesides, 1993*)
144 (*Figure 1 A*, top). Coating of the biomimetic pores was performed with Nsp1 containing a
145 C-terminal cysteine at a concentration of 1 μ M. We expect a lower limit for the grafting
146 distance in the pore of 6.5 nm as measured previously by surface plasmon resonance
147 experiments on flat gold surfaces (*Fragasso et al., 2022*). Additional passivation of the
148 remaining free area between Nsp1 molecules was achieved using short thiolated 350 Da
149 PEG molecules (*Jovanovic-Talisman et al., 2008, 2014*) (*Figure 1 A*, bottom).

150 After functionalization, the palladium membrane was mounted in a flow cell made
151 of polydimethylsiloxan (PDMS) which provides a reservoir on the upper side for the
152 addition of analyte, as well as a flow channel on the lower detection side to which a
153 constant flow was applied to avoid accumulation of fluorescently labeled molecules
154 (*Figure 2 A*). By diffusion, single proteins travelled through the pore upon which their
155 attached fluorophore got excited by the laser. The fluorescence signal of molecules
156 exiting the pore on the lower side was measured using a two-color confocal fluorescence
157 microscope. A high-numerical aperture objective lens with a long working distance was
158 used to focus the picosecond pulsed lasers in a diffraction-limited spot on the pore exit.
159 The fluorescence signal was detected on single-photon avalanche photodiodes after
160 passing through a pinhole and bandpass filter. For accurate and unbiased detection of
161 the signal spikes originating from single-molecule translocation, we adapted a change
162 point detection algorithm (*Watkins and Yang, 2005*) that takes full advantage of the single
163 photon information, as described previously in *Klughammer and Dekker (2021)*. To avoid
164 biases in the event detection, we ensured that experimental parameters such as the event
165 duration and the photons per molecule did not vary between experiments, e.g. due to
166 variations of the laser intensity or setup alignment (see *Data analysis* for more details).

167 The metal membrane was thick enough to prevent the incident laser light from reaching
168 the other side, which served to suppress the background fluorescence coming from
169 the reservoir side. Additionally, the nanopore acted as a zero-mode waveguide (ZMW),
170 resulting in an evanescent wave within the pore that exponentially decays on a length
171 scale of 10 nm to 20 nm, depending on the pore size (*Levene et al., 2003*). To obtain more
172 detailed insights into the optical properties in the proximity of the freestanding ZMW,
173 we performed finite-difference time-domain simulations of the excitation electric field
174 intensity and fluorescence emission (*Figure 2 C,D* and *Appendix 2—Figure 1*). As expected,

the propagation of the excitation light is effectively blocked by the nanoaperture and the electric field intensity $|E|^2$ decays exponentially within the nanopore. Interestingly, the presence of the reflecting metal surface also affects the intensity distribution further away from the nanopore, leading to the formation of a standing wave pattern. This effect is most visible for plane wave excitation (see **Appendix 2—Figure 3**), but is also present for focused excitation (**Figure 2 C** and **Appendix 2—Figure 2**). Molecules exiting the pore were hence mostly detected in the first lobe of the excitation profile and will likely diffuse away laterally before reaching intensity maxima further away from the membrane. To fully model the detected fluorescence signal $S(z)$, it is necessary to account for the modulation of the fluorescence quantum yield due to enhancement of the radiative and non-radiative rates by the metal nanostructure, as well as for the fraction of the signal that is emitted towards the upper side and thus cannot be detected (see Methods and **Appendix 2—Figure 4**). This further improves the blocking capability of the ZMW such that background signal from the reservoir is effectively suppressed even for large pores of 150 nm diameter (**Figure 2 D**). The detected fluorescence signal thus originates predominantly from molecules that exit from the pore and diffuse into the surrounding solution, which were excited by the truncated excitation volume below the pore.

Since the nanopores block the propagation of the excitation light across the membrane, they were not visible in a bright-field optical image. To facilitate the precise localization of the nanopores, we hence added a grid of *partially* milled markers centered around each pore that were easily visible on the microscope (**Figure 2 B**). To improve the throughput of the measurements, a linear array of eight pores of varying size was milled into the palladium membrane, and these pores were probed consecutively during the experiments. Crosstalk between pores was minimized by applying a flow orthogonal to the pore array, resulting in a false detection rate of less than 2 % (**Appendix 3**).

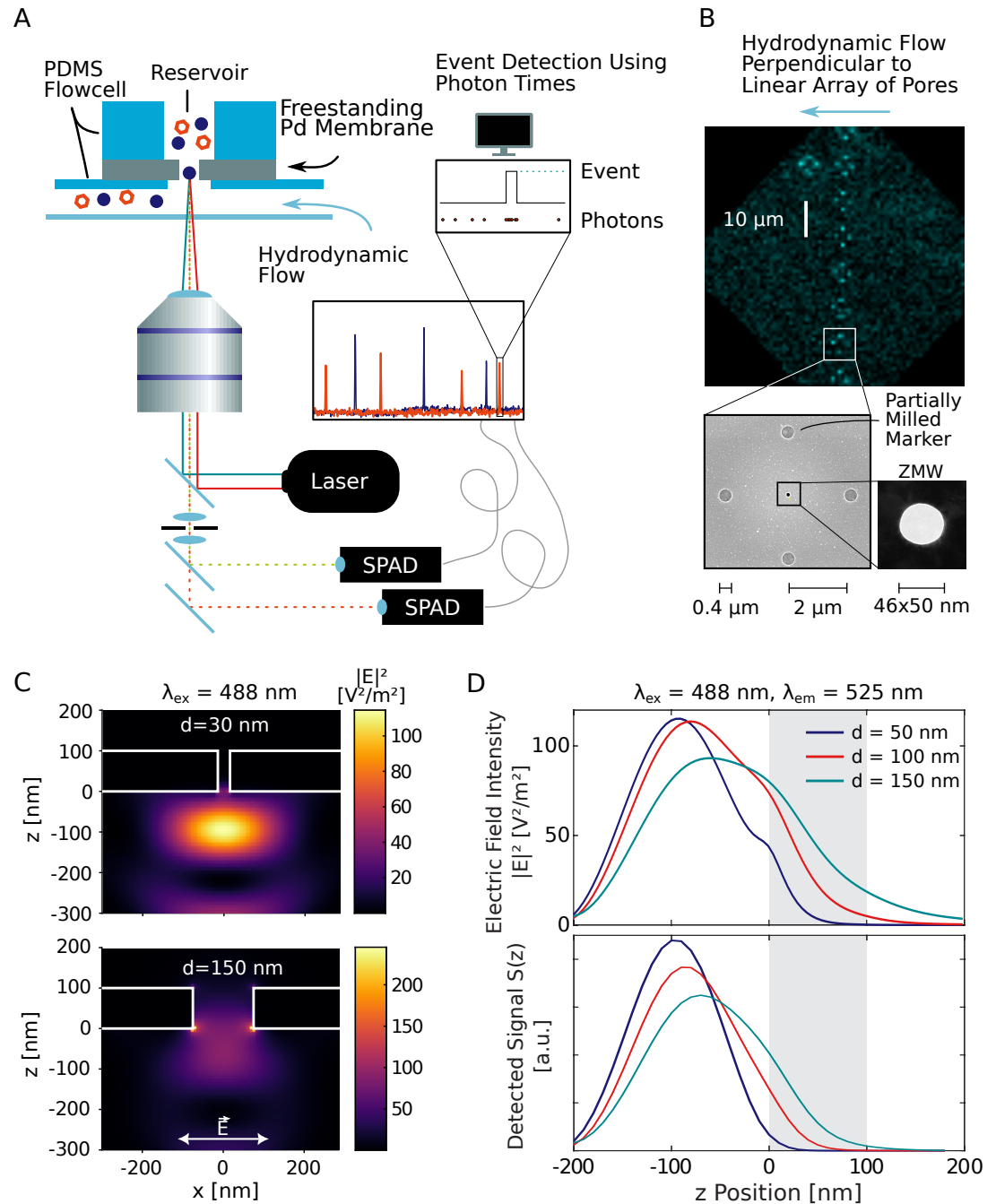
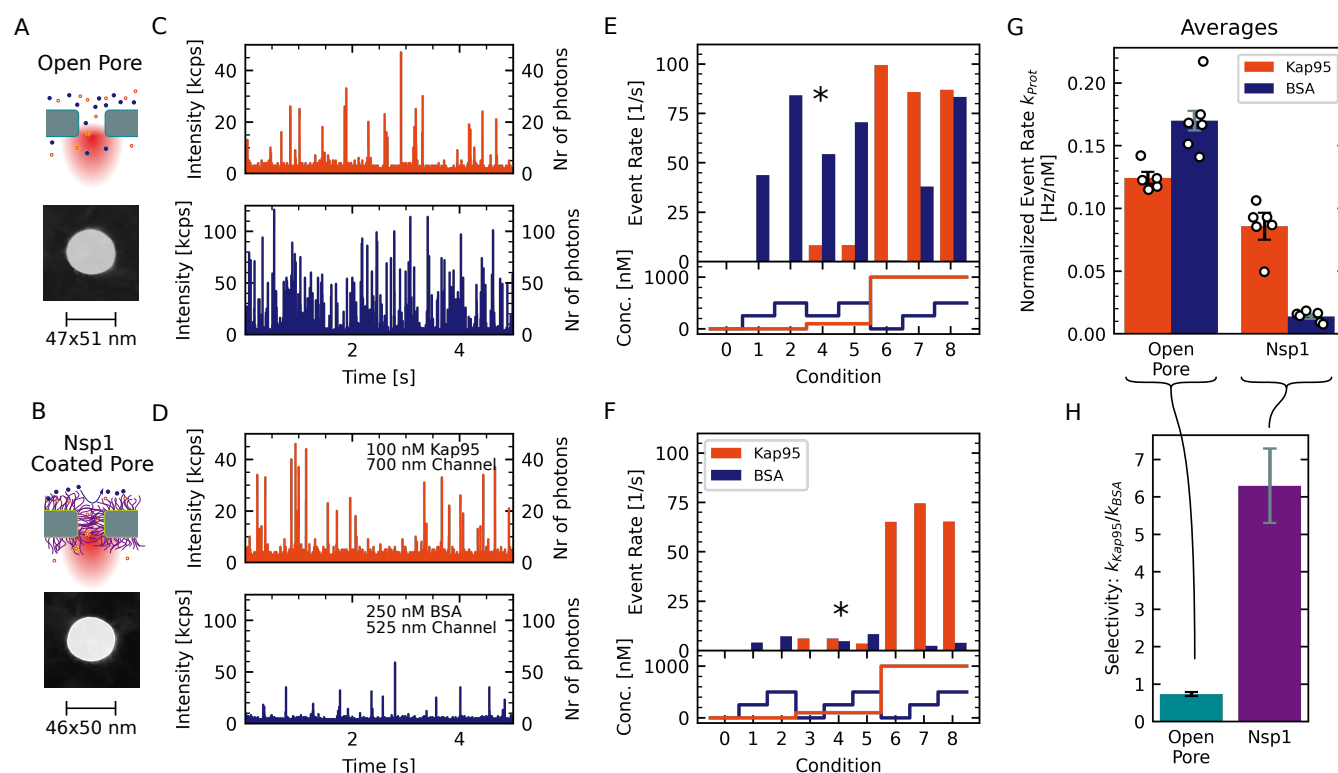


Figure 2. Experimental setup. (A) A free-standing Pd membrane containing the nanopores was mounted on a confocal microscope using a PDMS flow cell with a reservoir of $\approx 3 \mu\text{L}$ on the dark (cis) side and a flow channel on the detection (trans) side that faced the objective lens. A constant flow in the channel avoided the accumulation of analytes on the detection side. The lasers were focused onto the nanopore by a high NA objective lens and the fluorescence signal was detected on single-photon avalanche photodiodes. From the recorded photon arrival times, fluorescence bursts were detected using a change point detection algorithm. (B) A total of eight pores were milled into the Pd membrane, each surrounded by partially milled markers that facilitate the localization of the nanopores in a bright-field image (top). An additional marker was added such that the individual pores in the array could be identified. A scanning electron microscope image of a single pore with markers is shown below. The size and shape of each ZMW pore used in this study was determined using transmission electron microscopy (bottom right). (C) Simulated electric field intensity distributions in the xz plane near a freestanding ZMW for pore diameters of 30 (top) and 150 nm (bottom). A Gaussian laser beam was focused on the pore at a wavelength of 488 nm, polarized in the x-direction. See [Appendix 2—Figure 1](#) for different pore sizes and excitation at 640 nm. (D) Electric field intensity $|E^2|$ (top) and total detected signal $S(z)$ (bottom) as a function of the z-position along the center of the pore for an excitation wavelength of 488 nm and an emission wavelength of 525 nm, corresponding to the blue detection channel, for pores of 50, 100, and 150 nm diameter. The palladium membrane is indicated by the gray shaded area. See [Appendix 2—Figure 4](#) for the corresponding plots for the red channel.

NPC mimics show transport selectivity

To illustrate the workflow for estimating the transport selectivity of Nsp1-coated pores, we first describe our experiments on a pore with a diameter of 50 nm for which selectivity has previously been reported with Nsp1 in conductance measurements ([Ananth et al., 2018](#)) as shown in [Figure 3 A,B](#). The recorded time traces of Kap95 labeled with the Alexa Fluor 647 dye (Alexa647, orange) at a concentration of 100 nM and BSA labeled with the Alexa Fluor 488 dye (Alexa488, blue) at a concentration of 250 nM show efficient translocations for both proteins through the open pore ([Figure 3 C](#)). While Kap95 still translocated through the Nsp1-coated pore at a high rate, BSA was clearly hindered as is evident from the reduction of the number of signal spikes in the time trace ([Figure 3 D](#)).

For each pore, we probed a total of three different concentrations of BSA (0 nM, 250 nM, 500 nM) and Kap95 (0 nM, 100 nM, 1000 nM), and all combinations thereof. This resulted in nine different conditions that were tested consecutively (see [Figure 3 E–F](#), bottom), which allowed us to assess the linearity of the measured event rates with respect to the analyte concentration. Since Kap95 interacts strongly with the Nsp1 mesh, we performed a step-wise increase of the Kap95 concentration throughout the measurement while



probing the BSA response at every step (see [Appendix 4](#)). Importantly, this scheme enables us to test the influence of the Kap95 concentration on the event rates of BSA, as will be discussed below.

The measured event rates for Kap95 and BSA at the probed concentrations are shown in [Figure 3 E–F](#), confirming the reduction of the BSA translocation for the Nsp1-coated pore. To quantify the selectivity, we computed the concentration-normalized event rate k_{Kap95} or k_{BSA} in units of Hz/nM as the average over all probed conditions and corrected for the degree of the fluorescent labeling (1 for BSA and 0.7 for Kap95, [Figure 3 G](#)). Finally, we define the selectivity of the pore as the ratio of the average normalized event rates for Kap95 and BSA, $\frac{k_{\text{Kap95}}}{k_{\text{BSA}}}$, which should be independent of the pore diameter for open pores. High selectivity values indicate that Kap95 translocates at a higher rate compared to BSA. For the open pore, we find an selectivity of 0.73 ± 0.05 . A selectivity value between 0.7 and 0.8 is expected due to the smaller size and thus faster diffusivity of BSA, leading to a higher translocation rate compared to Kap95 (see [Appendix 5—Figure 1 E](#)). By contrast, the Nsp1-coated pore shows a significantly higher value of 6.3 ± 1.0 , indicating a clear selectivity induced by the Nsp1 coating.

Selectivity is lost at large pore diameters

Given recent reports on the dilation of the NPC central channel under stress conditions ([Zimmerli et al., 2021](#)), we set out to investigate the dependence of the transport selectivity on the pore diameter. Importantly, our approach allows us to measure pore sizes well above 60 nm that were previously inaccessible in conductance-based experiments ([Kowalczyk et al., 2011](#); [Ananth et al., 2018](#); [Fragasso et al., 2021](#)). We measured the normalized event rates and apparent selectivity of a total of 46 pores with diameters ranging from 35 nm to 160 nm, which were either open or coated with Nsp1 ([Figure 4](#)). Note that for pores above 80 nm diameter, it was necessary to reduce the fraction of labeled proteins five-fold in order to avoid too high event rates that would lead to non-linearity in the event detection due to overlapping events. This dilution is accounted for in the reported normalized event rates. We made sure that all data sets showed the same average molecular brightness (i.e., fluorescence signal per molecule). Data sets with lower average molecular brightness, which could occur due to sub-optimal alignment or trapping of air bubbles in the flow cell, were removed from further analysis (see [Data analysis](#) for details).

We measured protein translocation rates versus pore diameter for transport of both Kap95 and BSA through both open pores and Nsp1-coated pores, see [Figure 4](#). According to Fick's law of diffusion, the absolute translocation rate κ_{Prot} is expected to scale linearly with the concentration difference Δc between the cis and the trans side, and with the

diffusivity of the probe, D . Additionally it scales linearly with the cross-sectional area of the pore, given by $A = \pi r^2$ and thus it scales quadratically with the pore radius r . Further on, it scales inversely with the length of the pore, L . This results in a protein dependent translocation rate,

$$\kappa_{\text{Prot}} = AD \frac{\Delta c}{L} = \pi r^2 D \frac{\Delta c}{L}. \quad (1)$$

As a guide to the eye and for numerical comparison, we fitted the normalized event rates versus pore radius with such a quadratic function,

$$k_{\text{Prot}} = \alpha (r - r_{\text{Prot}})^2, \quad (2)$$

where k_{Prot} is the concentration-normalized event rate, r is the pore radius, and r_{Prot} is the radius of the protein (Kap95 in this case). Note that this equation accounts for a reduction of the effective cross-sectional pore area due to the fact that a protein has a finite volume and hence its center can not fully reach the rim of the pore. The only free parameter in the model is the multiplicative scaling factor α which combines the effects of the pore length, concentration gradient, and protein diffusivity, as well as any experimental factors arising from event detection and protein-pore interaction (see [Appendix 6](#) for further details). Note that this simple model does not include the pore diameter-dependent reduction of the diffusivity due to confinement ([Dechadilok and Deen, 2006](#)) which is discussed in [Appendix 5](#).

For Kap95, the translocation rate through Nsp1-coated pores was reduced by only about 10 percent compared to open pores, see [Figure 4](#) and [Appendix 6—Figure 2 E](#). In other words, we observed *no* significant reduction of the normalized event rate for Nsp1-coated pores compared to open pores ([Figure 4 A,C](#)). While this is remarkable, since one might a priori expect a reduction of the rate as an Nsp1-filled pore might obstruct protein transport, this finding signals the optimized properties of the Kap95 that interacts in a highly dynamic way with the FG repeats in Nsp1, which facilitate efficient transport. Our finding is in agreement with previous results on pores smaller than 30 nm ([Jovanovic-Talisman et al., 2008](#)). Interestingly, we also observed no reduced diffusivity of Kap95 molecules on the pore exit side, as quantified by fluorescence correlation spectroscopy (FCS) ([Appendix 7—Figure 1 A,B](#)). However, we observed a shortening of the fluorescence lifetime of Kap95–Alexa647 for Nsp1-coated pores compared to open pores, which was not observed for BSA–Alexa488 ([Appendix 7—Figure 1 C,D](#)). As the fluorescence lifetime is shortened in the proximity of the metal nanostructure (see [Appendix 2—Figure 4](#)), this indicates that Kap95 resides longer in the Nsp1 mesh compared to BSA.

For BSA, the normalized event rates for Nsp1-coated pores were, by contrast, significantly reduced, especially at small pore diameters ([Figure 4 B,D](#)). More specifically, we observed an approximate 10-fold reduction of the event rate for Nsp1-coated pores with

a diameter of 35 nm, whereas only a two-fold reduction was observed for pores with a diameter of 100 nm, which further decreases for larger pores (**Appendix 6—Figure 2 E**). Normalized event rates for open pores were well described by the quadratic function **Equation 2**. However, the BSA data for Nsp1-coated pores could not be described using the quadratic dependence with a single scaling factor over the whole range of pore diameters due to the steep increase of the event rate for larger pores (**Appendix 6—Figure 2 B,D**). We hence introduced an additional fit parameter b , which shifts the onset of the curve to higher pore diameters:

$$k_{\text{Prot}} = \alpha (r - r_{\text{Prot}} - b)^2. \quad (3)$$

The parameter b reduces the effective pore diameter accessible to BSA and can be seen as an estimate of the amount of Nsp1 inside the pore. From the fit, we obtained $b = 11.5 \pm 0.4$ nm (error is SD estimated from the fit), which indeed is comparable to the height of Nsp1 brushes on flat surfaces (**Wagner et al., 2015**).

Next, we calculated the selectivity ratio $\frac{k_{\text{Kap95}}}{k_{\text{BSA}}}$ to facilitate a direct comparison of pores with different diameters (**Figure 4 E**). For open pores, we find a selectivity ratio of 0.70 ± 0.02 , independent of the pore diameter. This agrees well with predicted selectivity values of 0.7 to 0.8 for open pores, based on Fick's law for the different pore diameters (see **Appendix 5—Figure 1**). Note that the value of 0.70 deviates from 1 due to the different size of the two proteins which leads to different diffusion coefficients. For Nsp1-coated pores below 50 nm, selectivity ratios of individual pores ranged between 2.1 ± 0.4 and 6.3 ± 1.0 , which is three to nine times higher than for open pores. This observed selectivity for smaller pores originates predominantly from a blockage of BSA translocations by the Nsp1 mesh, while the Kap translocation rates remain largely unaffected. For pores larger than 60 nm, we see a gradual decrease of the selectivity ratio with increasing pore diameter from 1.7 ± 0.2 to a value of 0.7 ± 0.2 for the largest pores, that approaches the selectivity ratio of open pores. The finite selectivity for large pores suggests that the Nsp1 coating on the pore walls still hindered the translocation of BSA, even after most of the selectivity was lost. The remaining selectivity decreased gradually with the pore diameter because the relative amount of Nsp1 molecules per pore cross-sectional area is reduced, as will be discussed in more detail below.

While the event rates were adequately described by the quadratic function, we observed a large variability between pores of similar size, even for open pores (**Figure 4 A–D**). As the variation of the event rate of Kap95 and BSA showed a high degree of correlation (see **Appendix 8—Figure 1**), the spread of the selectivity ratio was markedly reduced for open pore experiments. However, the spread remained high for Nsp1-coated pores (**Figure 4 E**), which we estimate to be due to pore-to-pore variations of the grafting density.

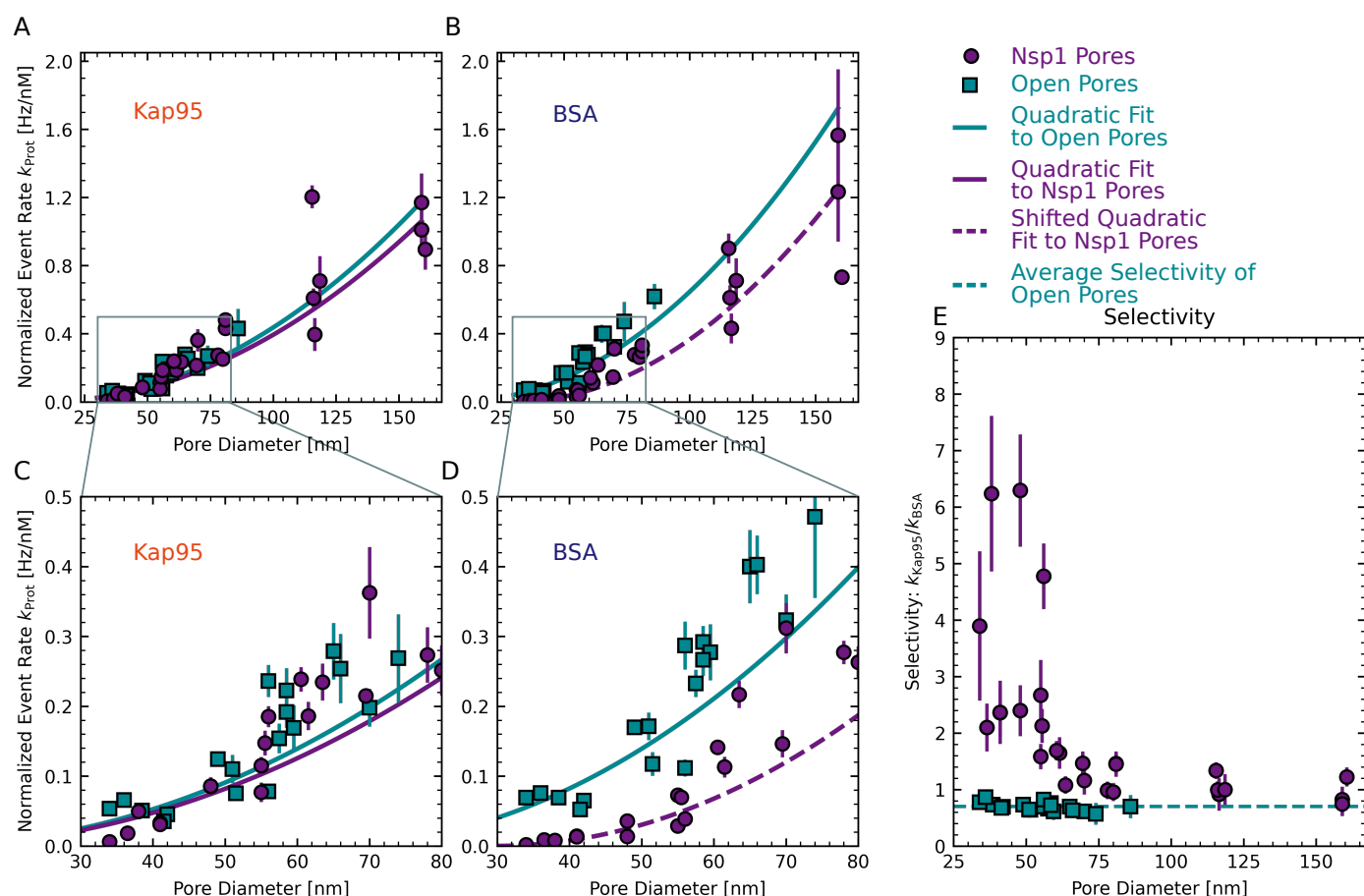


Figure 4. Dependence of translocation rates and selectivity on pore diameter (A–D) Concentration-normalized event rate of Kap95 (A) and BSA (B) as a function of pore diameter for open pores (cyan squares) and Nsp1-coated pores (purple circles). While the normalized event rate for Kap95 did not change significantly between open and Nsp1-coated pores, a clear reduction was observed for BSA, which was most pronounced at small pore sizes. Solid lines are fits to a quadratic function given in [Equation 2](#). To model the size dependence of BSA translocations through Nsp1 pores, an offset was introduced that shifts the onset of the quadratic curve to higher diameters (dashed line, [Equation 3](#)). (C, D) Zoom-ins of the indicated regions in A,B. In A–D, the error bars represent the standard error of the mean of the normalized event rates obtained at different protein concentrations. (E) Apparent selectivity versus pore diameter. The data show that selectivity was lost for Nsp1-coated pores with increasing diameter. The average selectivity for open pores of 0.70 ± 0.01 is shown by the dashed cyan line. Error bars indicate the propagated error from the normalized event rates shown in A–D.

We note that the variability was not due to chip-to-chip variation as a similar spread is also seen within pores that were measured together on one chip in the same experiment (see [Appendix 9—Figure 1](#)).

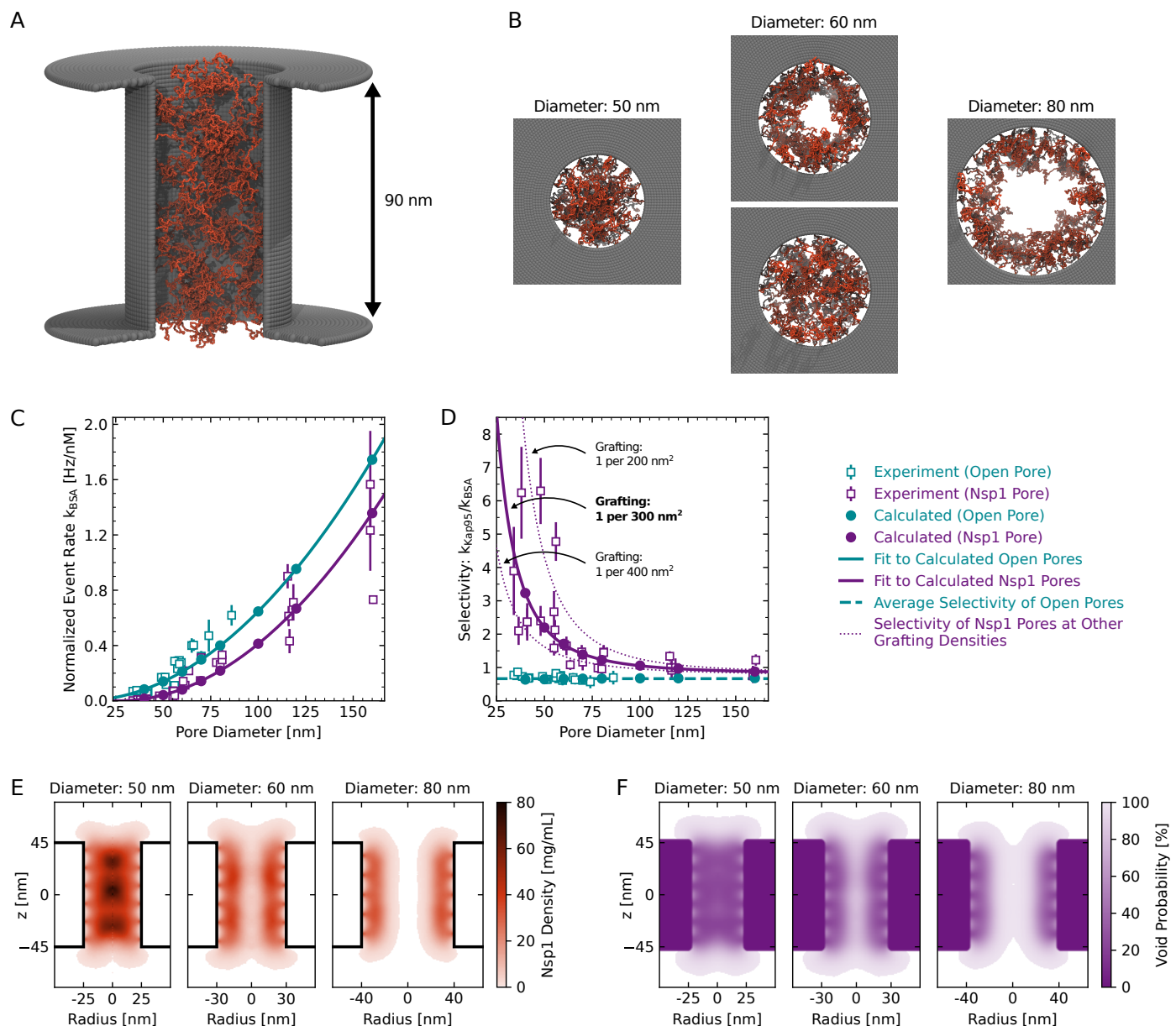
Coarse-grained modeling reveals transition of the Nsp1 mesh

To gain a microscopic understanding of the structure and dynamics of the Nsp1 meshwork, we performed coarse-grained molecular dynamics (CGMD) simulations of BSA transport across Nsp1-coated nanopores over a range of diameters and grafting densities. We used an earlier-developed residue-scale model ([Ghavami et al., 2013, 2014](#); [Dekker et al., 2022](#)) that has been used to study Nsp1-functionalized nanopores ([Ketterer et al., 2018](#); [Ananth et al., 2018](#); [Fragasso et al., 2022](#)) and liquid-liquid phase separation of FG-Nups ([Dekker et al., 2022](#)). Within the microsecond time scale of our CGMD simulations, we found that passive diffusion of BSA through the nanopore channel was a rare event, especially at the smaller-size pores. To obtain statistically meaningful estimates of the translocation rates, we applied a void analysis method developed by [Winogradoff et al. \(2022\)](#). Rather than explicitly simulating translocation events, we used this theoretical approach to predict translocation rates based on the equilibrium fluctuations of the Nsp1 mesh. Because this method uses the entire simulation volume to characterize the energy barrier that a translocating protein such as BSA would need to overcome, the resulting event rates have much better statistical sampling than can be obtained from brute-force passive diffusion simulations. In brief, we estimated the energy barrier for the translocation of inert probes with the size of BSA from simulations of the Nsp1 mesh alone by quantifying the occurrence of openings ('voids') within the mesh that can accommodate the inert probe without steric clashes. The resulting probability distribution of the occupancy along the pore axis can then be converted into a potential of mean force (PMF) using Boltzmann inversion, which represents the energy barrier for translocation. From this, protein translocation rates were computed by relating the energy barrier to $k_B T$ using the Arrhenius relation.

We performed simulations of nanopores with a length of 90 nm and diameters in the range of 40 nm to 160 nm. Nsp1 proteins were anchored at their C-terminus to the interior wall of the nanopore scaffold in a close-packed triangular distribution ([Figure 5 A](#)). From the equilibrium trajectories, we computed the PMF and use that to estimate the energy barrier, ΔE , that BSA proteins need to overcome during translocation as the average value of the PMF at the center of the pore ([Appendix 10—Figure 2](#)). Translocation rates were then obtained using the Arrhenius relation:

$$k_{BSA} = k_{0,BSA} \exp(-\Delta E/k_B T), \quad (4)$$

where $k_{0,BSA}$ is a proportionality constant to match the experimental event rates for open



356 pores (see [Appendix 10—Figure 1](#)). While $k_{0,BSA}$ is the same for open and Nsp1-coated
 357 pores of any diameter, ΔE is calculated for each individual pore using the void analysis
 358 method.

359 As the precise grafting density of Nsp1 proteins within the pore in the experiment is not
 360 known accurately, we treated it as the only tunable parameter in the simulations to match
 361 the experimental BSA translocation rates. Using a previously estimated grafting density
 362 of 1 Nsp1 per 28 nm² for 20 nm thick solid state nanopores ([Ananth et al., 2018](#)), the
 363 calculated BSA translocation rates significantly underestimated the experimental values
 364 (not shown here), which prompted us to probe much lower grafting densities between
 365 1 Nsp1 per 200–400 nm². The best match between the experimental and calculated BSA

Figure 5. Coarse-grained modeling of Nsp1-coated pores. (A) One-bead-per-residue representation of an Nsp1-coated nanopore. (B) Top views of the Nsp1 meshwork in pores of 50 nm, 60 nm and 80 nm diameter (for a grafting density of 1 Nsp1 per 300 nm²). For pores with a diameter below 60 nm the Nsp1 meshwork was closed throughout the entire simulation, while for pores with diameters \approx 60 nm transient openings were observed in the center of the pore, that were persistent for diameters \geq 80 nm. (C) Calculated event rate of BSA as a function of pore diameter for open pores (cyan filled dots) and Nsp1-coated pores (purple dots) for a grafting density of 1 Nsp1 per 300 nm². The calculated event rates are in good agreement with the experimental event rates (open squares). Solid lines are fits to the calculated event rates using the quadratic function given in (2) for open pores and (3) for Nsp1-coated pores. (D) Calculated selectivity versus pore diameter, showing that the selectivity is lost for Nsp1-coated pores with increasing diameter. The average selectivity for open pores is shown as a green dashed line. The effect of grafting density on the apparent selectivity is indicated by the purple dotted lines that depict the results for grafting densities of 1 Nsp1 per 200 nm² and 1 Nsp1 per 400 nm² (see [Appendix 10—Figure 3](#)). (E) Axi-radial and time-averaged protein density distributions inside Nsp1-coated pores of 50 nm, 60 nm and 80 nm diameter at a grafting density of 1 Nsp1 per 300 nm². For pore diameters below 60 nm, we observed the highest protein density along the pore axis, while for diameters \geq 60 nm, the highest density was found near the pore walls. This observation was valid for each of the probed Nsp1 grafting densities (see [Appendix 10—Figure 4](#)). (F) Axi-radial and time-averaged void distributions inside Nsp1-coated pores of 50 nm, 60 nm and 80 nm diameter at a grafting density of 1 Nsp1 per 300 nm². The void distributions suggest that for pores of 50 nm diameter there is no preferred pathway for the BSA proteins, while for larger pores the translocations happen mostly along the central axis.

Figure 5—video 1. Video of the top view of the pores presented in B for 40 ns of the simulation.

event rates over the whole range of probed diameters was obtained at a grafting density of 1 Nsp1 per 300 nm² ([Figure 5 D](#) and [Appendix 10—Figure 3 A,B](#)). Note that the estimated grafting density is approximately one order of magnitude lower compared to 20 nm-thick NPC mimics ([Ananth et al., 2018](#)). Yet, we still obtain comparable protein densities of 50–150 mg/mL because the relatively long channel of the ZMW pores prevents the Nsp1 molecules from spilling out of the pore as in the case for 20 nm thick SiN nanopores. Indeed, these FG-Nup densities are comparable to densities of 30–300 mg/ml found in simulations of full NPCs ([Ghavami et al., 2014](#); [Winogradoff et al., 2022](#)).

The calculated BSA translocation rates continuously increased with increasing diameter and reproduced the trend of the experimental data well ([Figure 5 C](#)). Similar to the experimental data, we observed a delayed onset of the BSA translocation rate for Nsp1-coated pores with an offset of 9.9 ± 0.1 nm, which compares quite well to the experimental value of 11.5 ± 0.4 nm. To compute the selectivity ratio from the BSA translocation rates, we assumed that the Kap95 translocation rate through Nsp1-coated pores is equal to that for open pores, as we did not observe any significant hindrance of Kap95 translocation by the Nsp1 mesh in the experiment ([Figure 4 A,C](#)). The computed selectivity ratios for a grafting density of 1 Nsp1 per 300 nm² are in good agreement with the experimental values ([Figure 5 D](#)), especially given that we basically only employ a single fitting parameter.

Similar to the experiments, we observed a strong decrease of the selectivity with pore

diameter that gradually approached the open pore base line. Additionally, we found that the selectivity ratio is highly sensitive to variations of the grafting density, suggesting that the considerable variation in the experimental data might originate from variations of the grafting density between 1 Nsp1 per 200 nm² to 1 Nsp1 per 400 nm² (**Figure 5 D**).

The simulations provide a microscopic view of the structure of the Nsp1 mesh within the pore (**Figure 5 A,B,E**, and **Figure 5—video 1**). At pore diameters below 60 nm, the Nsp1 mesh remained closed over the entire duration of the simulation and the highest protein density was found along the central axis. This is facilitated by the high cohesiveness of the N-terminal domains of Nsp1 which contain a large amount of hydrophobic amino acids (**Dekker et al., 2022**). For pore diameters above 60 nm, however, the highest protein density was found at the pore walls (**Figure 5 E**) and we observed the transient formation of a central channel that became persistent at pore diameters above 80 nm (**Figure 5 B,E**). Despite the transient appearance of a central channel at pore diameters of 60 nm and the shift of the highest protein density away from the center, the predicted translocation rates increased continuously and followed the quadratic model over the whole range of probed diameters (**Figure 5 C**). This finding is in contrast to an instantaneous onset of translocations as one might expect from a static opening of a central channel. As the pore diameter increased, the selectivity ratio became less dependent on the grafting density (**Figure 5 D**) because BSA translocated mainly through the wide central channel (**Figure 5 B,C**).

To estimate the pathways through which proteins can permeate the Nsp1 mesh, we determined the spatial distribution of the voids that can accommodate BSA, which represents the potential occupancy of BSA in the pore (**Figure 5 F**). For diameters below 60 nm, the distribution of the voids was homogeneous across the Nsp1 mesh, suggesting the absence of a preferred pathway. Surprisingly, the potential occupancy of BSA was not markedly reduced along the pore axis compared to the periphery, despite the high protein density in this region. For diameters above 60 nm, the distribution of voids closely followed the time-averaged protein density inside the pores, confirming that most BSA translocations occur through the central channel of the Nsp1 mesh. Although this central channel was not continuously present in the 60 nm pores, the void distribution confirms that most translocations still occurred through the center at this diameter.

Kap95 modulates the permeability for BSA

In the context of Kap-centric models of nuclear transport, it has recently been shown that depletion of Kaps from the FG-Nup mesh reduces the selectivity of the NPC in cells (**Kalita et al., 2022**). To test if a similar effect was present in our data, we averaged the concentration-normalized event rates for the two BSA concentrations (of 250 nM

and 500 nM) measured at Kap95 concentrations of either 0 nM, 100 nM, or 1000 nM, and denoted them as $k_{\text{BSA},0}$, $k_{\text{BSA},100}$, and $k_{\text{BSA},1000}$ (**Figure 6 A**). To minimize the dependence of the rates on the pore diameter, we assessed the relative rates with respect to the event rate in the absence of Kap95, $\frac{k_{\text{BSA},100}}{k_{\text{BSA},0}}$ and $\frac{k_{\text{BSA},1000}}{k_{\text{BSA},0}}$, which serve as a measure for Kap-induced changes of the permeability of the pore for BSA (**Figure 6 B,C**). In other words, a factor of 1 for this ratio would indicate that BSA transport does not depend on the Kap95 concentration.

We found no significant change of the BSA event rate at 100 nM Kap95 compared to the absence of Kap95 ($\frac{k_{\text{BSA},100}}{k_{\text{BSA},0}} = 1.2 \pm 0.1$) (**Figure 6 B**), which is similar to the value measured for open pores ($\frac{k_{\text{BSA},100}}{k_{\text{BSA},0}} = 1.3 \pm 0.1$). However, at a Kap95 concentration of 1000 nM, we observed a clear increase of the BSA leakage for pores larger than 60 nm ($\frac{k_{\text{BSA},1000}}{k_{\text{BSA},0}} = 1.6 \pm 0.2$), and a small reduction of the BSA translocation rates for smaller Nsp1-coated pores ($\frac{k_{\text{BSA},1000}}{k_{\text{BSA},0}} = 0.8 \pm 0.1$) similar to the data for open pores ($\frac{k_{\text{BSA},1000}}{k_{\text{BSA},0}} = 0.9 \pm 0.1$), see **Figure 6 C**. The increase of the BSA translocation rate at a high concentration of Kap95 seems counter-intuitive given that the accumulation of Kap95 in the Nsp1 mesh is expected to obstruct BSA translocations by steric hindrance. However, we thus observed the opposite effect, where a high concentration of Kap95 appeared to increase the event rates of BSA. Since this effect was not observed for open pores, it must have been induced by a rearrangement of the Nsp1 mesh.

Next, we computed the selectivity ratio based on the normalized event rates of BSA measured at the different Kap95 concentrations (**Figure 6 D**). Note that for the calculation of the selectivity ratio, we assumed that the normalized event rate of Kap95 is independent of the Kap95 concentration by using the average normalized event rate over all concentrations, k_{Kap95} , which is an approximation for the more complex behavior discussed in (**Appendix 11—Figure 1**). For small pores (<50 nm), we observed a moderate increase of the selectivity ratio at 1000 nM Kap95 compared to lower concentrations of Kap95 (**Figure 6 E**). Interestingly, we found an almost two-fold increase of the Kap95 translocation rate for small pores at 1000 nM compared to 100 nM, which was absent for large pores (see **Appendix 11—Figure 1**). Combined, the reduction of the translocation rate for BSA and the increase for Kap95 resulted in an increase of the apparent selectivity for small pores to 7.1 ± 1.6 at a Kap95 concentration of 1000 nM. No effect of the BSA concentration on the translocation rates of Kap95 was observed (**Appendix 11—Figure 1**). This suggests that the binding of Kap95 to the FG-Nup mesh increased the selectivity of Nsp1-coated pores, leading to a reduction of the BSA translocation rate, whereas no such effect was seen for open pores. In contrast, larger pores above 60 nm showed a lower selectivity at all Kap95 concentration compared to small Nsp1 pores (**Figure 6 D**). While this difference was small for Kap95 concentrations of 0 nM and 100 nM, a considerable

reduction to almost the bare pore selectivity was observed for 1000 nM Kap95. After this initial step, we found a gradual decrease of the selectivity with the pore diameter, which is expected because the amount of Nsp1 deposited on the pore wall scales only linearly with the pore diameter while the pores cross-sectional area scales quadratically.

As suggested by the MD simulations, the loss of selectivity for pores above 60 nm may be explained by the opening of a central channel that allows BSA to pass unhindered. To obtain an estimate for the size of such a channel, we devised a simple model to estimate the fraction of the cross-sectional pore area that is occupied by the selective FG-Nup phase (**Figure 6 F**). The selective area fraction was obtained from the measured selectivity ratio under the assumption that large Nsp1-coated pores are divided into selective and non-selective areas, where the selective area was assumed to have a selectivity equivalent to the value measured for small pores. We related the selective area fraction to the structural change of the Nsp1 brush by assuming that each Nsp1 molecule renders a certain volume $V_{\text{selective}}$. At a given grafting density σ on the pore wall of diameter r , the selective area fraction $\frac{A_{\text{Nsp1}}}{A}$ is then given by:

$$\frac{A_{\text{Nsp1}}}{A} = \sigma V \frac{2}{r}, \quad (5)$$

where the factor σV was the only fit parameter. The unit of the product σV is a length which can be related to the apparent Nsp1 layer thickness at the pore wall (see **Appendix 11** for the details of the model). From the selective area fraction, we computed the apparent selectivity of a pore and estimated the factor σV by fitting it to the experimentally obtained selectivities (**Figure 4 D and G**). The estimated thickness in the absence of Kap95 of ~ 12 nm agrees well with measurements on flat surfaces (**Wagner et al., 2015**). While no significant change was detected at 100 nM Kap95, we observed a drastic decrease of the estimated layer thickness by a factor of ≈ 2 at 1000 nM Kap95 compared to the absence of Kap95 (**Figure 4 G**), suggesting that the Nsp1 layer collapsed as it was occupied by Kap95.

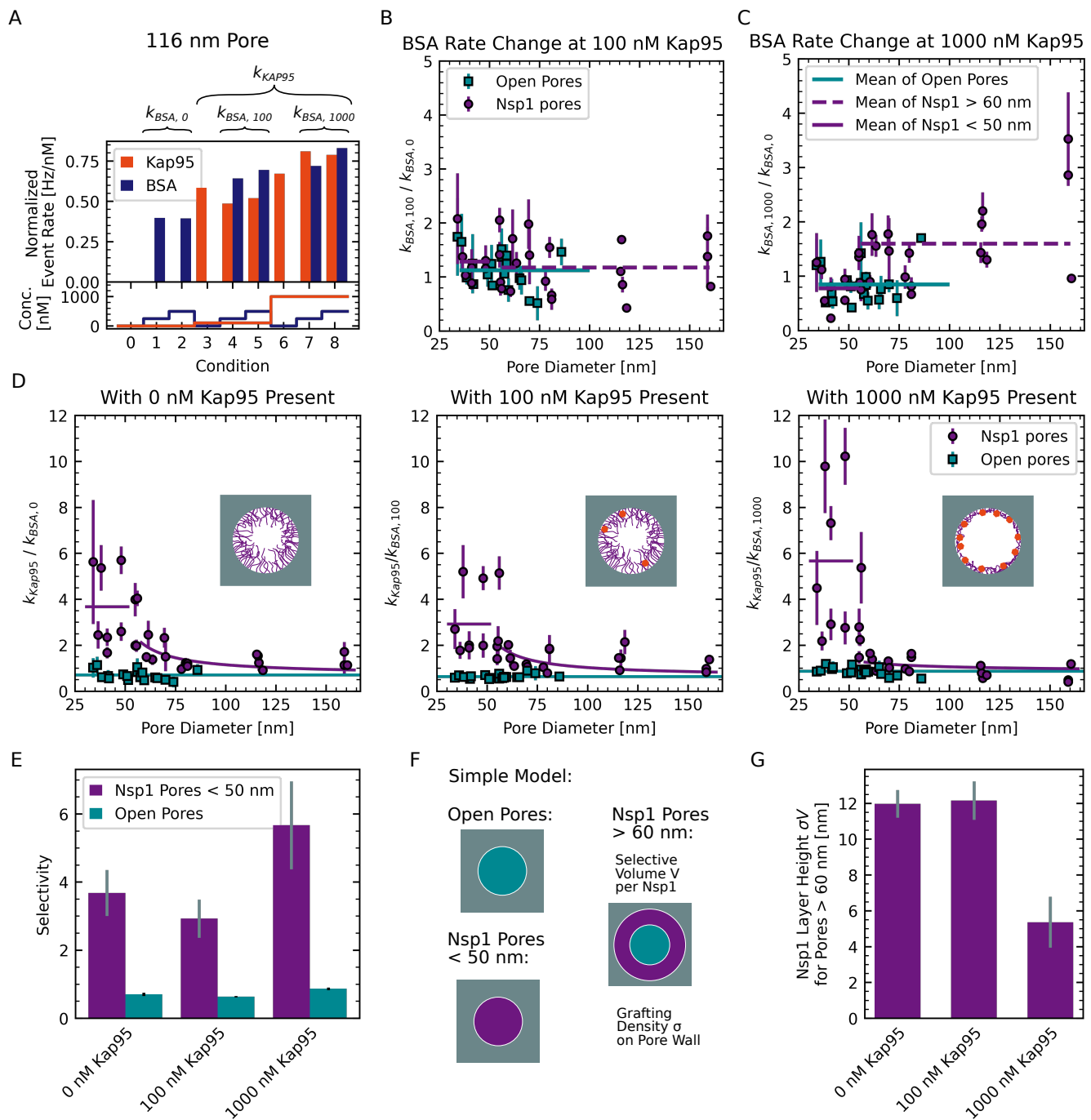


Figure 6. BSA permeation depends on Kap95 concentration. (A) BSA event rates measured at the different Kap95 concentrations of 0 nM, 100 nM, and 1000 nM were averaged to obtain the Kap95-concentration dependent event rates $k_{\text{BSA},0}$, $k_{\text{BSA},100}$ and $k_{\text{BSA},1000}$. Data shown were obtained using an Nsp1-coated pore with a diameter of 116 nm. (B,C) Plots of the relative change of the BSA event rate measured at 100 nM and 1000 nM Kap95 compared to no Kap95, i.e. $\frac{k_{\text{BSA},100}}{k_{\text{BSA},0}}$ and $\frac{k_{\text{BSA},1000}}{k_{\text{BSA},0}}$, versus pore diameter. A considerable increase of the BSA event rate is observed for large pores in the presence of 1000 nM Kap95. (D) Plots of the selectivity ratio, defined as the ratio of the normalized BSA event rate measured at a given Kap95 concentration to the average normalized Kap95 event rate of the pore, i.e. $\frac{k_{\text{BSA},i}}{k_{\text{Kap95}}}$ for $i = 0, 100$ and 1000, against the pore diameter. The average selectivity ratio of open pores (cyan) and Nsp1-coated pore smaller than 50 nm (purple) are shown as a horizontal line. Data of large Nsp1-coated pores above 60 nm diameter were fitted to the selective area model function (purple lines, see [Equation 5](#)). (E) Average selectivity defined as $\frac{k_{\text{BSA},i}}{k_{\text{Kap95}}}$ for open pores and Nsp1-coated pores below 50 nm. Error bars represent standard deviations estimated from fitting horizontal lines. A moderate increase of the selectivity of Nsp1-coated pores is observed at 1000 nM Kap95. (F) Simple model for the selectivity of Nsp1-coated pores. We assume large Nsp1-coated pores ≥ 60 nm to separate into unselective and selective areas with selectivities equivalent to that of open pores or small Nsp1-coated pores, respectively. (G) The parameter σV quantifies the thickness of the Nsp1 layer, which decreases in the presence of 1000 nM Kap95. Error bars represent standard deviations estimated from the fits.

Discussion

In this study, we present an assay to measure the selectivity of nanopore-based NPC mimics at single molecule resolution using optical detection. Our assay is based on nanopores drilled into freestanding palladium membranes that act as zero-mode waveguides to block the propagation of the excitation light. This allows the localized and selective detection of fluorescently labeled molecules that exit from the pore. We build on our previous work which established palladium nanopores as a viable tool for single-molecule studies ([Klughammer and Dekker, 2021](#)) by functionalizing the nanopores with the FG-Nup Nsp1 to build a minimal biomimetic system of the NPC. To this end, we developed a gentle cleaning protocol that leaves the pore shape unaltered while rendering the metal surface susceptible for efficient thiol binding.

Our approach offers several advantages compared to conductance-based nanopore measurements ([Kowalczyk et al., 2011](#); [Ananth et al., 2018](#); [Fragasso et al., 2021, 2022](#)), namely a superior signal-to-noise ratio, an excellent specificity for the labeled analyte that enables multiplexed detection of different components, higher throughput by measuring multiple pores in a single experiment, no limitations on pore size, and the potential to add unlabeled components while still investigating their effects. Importantly, our approach also allows us to measure translocations by free diffusion in the absence of an external electric field which may potentially bias the experiment. Compared to previous optical approaches ([Jovanovic-Talisman et al., 2008](#)), our assay offers the capability to follow

single molecules through individual pores. On the technological side, one could increase the throughput of our approach by moving towards a camera-based readout which would enable the simultaneous reading of hundreds of pores. Despite the many benefits of our approach, some differences remain when comparing our biomimetic ZMW pores to the NPC, as e.g. the 90 nm long channel used here is approximately three times longer (Kim *et al.*, 2018), and FG-Nups are grafted to the entire metal surface rather than being limited to the pore walls. In spite of these differences, the in vitro biomimetic approaches remain useful to study key elements of nuclear transport.

To evaluate the performance and sensitivity of our approach, it is relevant to compare the absolute event rates through open pores to theoretical expectations. Compared to Fick's law of diffusion, the absolute event rates for BSA and Kap95 through open pores were underestimated by approximately a factor of 3, as estimated from the scaling factors (Appendix 5—Figure 1). Additionally, we had previously found that repeated detection of the same molecule leads to an overestimation of the event rate compared to the actual translocation rate by approximately a factor of 2 (Klughammer and Dekker, 2021). Combined, this resulted in a ≈ 6 -times lower translocation rate compared to what is predicted from Fick's law, potentially due to the hydrodynamic pressure applied in our experiments (Auger *et al.*, 2014), protein-pore interactions, and missing of low-signal events by the detection algorithm.

Compared to the study of Jovanovic-Talisman *et al.* (2008), who report values of 0.003 Hz/nM obtained from bulk studies on 30 nm pores, we find an order of magnitude higher event rates of approximately 0.04 Hz/nM for pores of similar size. This discrepancy can be explained by the fact that the functionalized pores used by Jovanovic-Talisman *et al.* (2008) were placed at the ends of 6 μ m long channels which is expected to considerably reduce the translocation rates. When comparing with conductance-based nanopore measurements in 20 nm thick silicon nitride membranes, previous studies have reported rates of 0.0003 Hz/nM for 30 nm pores (Fragasso *et al.*, 2021) and 0.00005 Hz/nM for 42 nm to 46 nm pores (Kowalczyk *et al.*, 2011). Both these values are many orders of magnitude lower compared to what is predicted by Fick's law, indicating that a large fraction of potential translocation events was previously not detected, cf. Plesa *et al.* (2013). On the other hand, Ananth *et al.* (2018) measured event rates of Kap95 through open 48 nm pores of 0.017 Hz/nM, which is much closer to our measurements of 0.08 Hz/nM compared to other conductance-based studies. The system in conductance-based experiments is more complex, however, with an interplay of diffusion and electro-osmotic and electro-phoretic forces. This illustrates that our optical approach offers a higher detection efficiency of translocation events and provides a better mimic of the diffusion driven transport through the real NPC, compared to conductance-based nanopore experiments.

We implemented an experimental scheme to assess the selectivity of single Nsp1-coated pores by measuring the concentration-dependent translocation rates of the inert probe BSA and the NTR Kap95. To elucidate the size dependence of the selectivity, we scanned a wide range of pore diameters from 35 nm to 160 nm, which was previously not possible in conductance-based approaches. We found a steep decrease of the selectivity with the pore diameter, where the BSA event rate approaches its open pore value for large pore diameters. For small diameters, the BSA event rate was decreased 10-fold compared to open pores, similar to a 5-fold decrease reported for pores smaller than 30 nm by *Jovanovic-Talisman et al. (2008)*. For large pores, BSA translocation was only hindered by a factor of 1.4 (**Appendix 6—Figure 2 E**). On the other hand, translocation rates for Kap95 were unaffected by the Nsp1 coating (reduction factor of 1.1), in agreement with previous reports (*Jovanovic-Talisman et al., 2008; Kowalczyk et al., 2011; Ananth et al., 2018; Fragasso et al., 2021*). Notably, our data reveals a gradual decrease of the selectivity rather than a threshold-like behavior, in line with the results of *Jovanovic-Talisman et al. (2008)* who found a gradual decrease of the selectivity for three distinct pore sizes of 30 nm, 50 nm, and 100 nm.

Coarse-grained molecular dynamics simulations allowed us to reproduce the experimental selectivities for a grafting density of $1/(300 \text{ nm}^2)$. While this value is lower compared to previous reports on silicon nitride nanopores (*Fragasso et al., 2021*), we still achieve similar protein densities at the center of the 90 nm-long channel. Similar to the experimental data, the steepest decrease of the selectivity occurred at small diameters. In addition, simulations at varying grafting density revealed that stochastic variation of the surface grafting efficiency is a likely cause for the pore-to-pore variation of the event rates observed in the experiment. The simulations reveal the opening of a central channel in the Nsp1 mesh for pore diameters above 60 nm. However, the event rates predicted by the void analysis showed a continuous decrease of the selectivity with pore diameter even before a central channel was observed in the Nsp1 mesh. This suggests that the formation of a stable transport conduit is not required for the permeation of BSA through the Nsp1 mesh, but may also occur efficiently through transient openings. The absence of a discrete step in the experimental selectivity at a specific pore diameter is thus at odds with a static picture of either an extended or collapsed Nsp1-mesh but rather supports a dynamic transition between both states for intermediate pore diameters. For larger pore diameters, a central channel opened and only a peripheral ring was occupied by Nsp1. This occurred due to the following factors. First, the increased entropic cost of extension for the Nsp1 molecules to interact across the pore. Second, the amount of Nsp1 molecules per pore volume decreases with pore diameter, as the volume increases quadratically while the number of molecules increases linearly. Last, while increasing the diameter,

576 also the curvature decreases which reduces the lateral constraint of neighbouring Nsp1.

577 We found experimentally that the main loss of selectivity falls in a size range between
578 40 nm to 60 nm. Intriguingly, it has recently been reported that the inner ring diameter
579 of the NPC can be significantly larger in situ at 60 nm compared to 40 nm for isolated
580 NPCs (*Akey et al., 2022*). Furthermore, NPC dilation is modulated in cellulo in response to
581 stress conditions such as energy depletion or osmotic shock (*Zimmerli et al., 2021*). This
582 suggests that the dilation of the NPC might be a way for the cell to tune the permeability
583 of the NPC under stress to increase the selectivity at the cost of lower transport rate .

584 In light of Kap-centric models of nuclear transport (*Lim et al., 2015*), we also tested
585 the influence of the Kap95 concentration on the selectivity and permeability of Nsp1-
586 coated pores. Small pores below 50 nm showed a moderate increase in selectivity at
587 a Kap95 concentration of 1 μ M compared to the absence of Kap95, caused by a slight
588 reduction of the permeability of the pores for BSA. A comparable effect was described by
589 *Jovanovic-Talisman et al. (2008)*, who found that the BSA flux through 30 nm pores halved
590 when 2 μ M of the nuclear transport factor NTF2 was present. In contrast, we observed
591 an almost 2-fold increase of the BSA translocation rate for large pores above 60 nm by
592 increasing the Kap95 concentration from 0 μ M to 1 μ M. This result seems counterintuitive
593 considering that Kap95 occupancy within the pore should pose an additional hindrance for
594 the translocation of BSA. Quantification of this effect, however, showed that the selective
595 area fraction within the pore was significantly reduced at 1 μ M Kap95, which we attribute
596 to a compaction of the Nsp1 layer. From our data, we found a 2-fold reduction of the
597 cross-sectional area of the Nsp1 layer inside the pore. A much smaller Kap-induced
598 compaction of 16 nm high Nsp1 brushes on flat surfaces of <10 % was observed in SPR
599 measurements at a Kap95 concentration of 100 nM by *Wagner et al. (2015)*, where however
600 only a fragment of the extended domain of Nsp1 was used. The stark change of the Nsp1
601 layer thickness seen in our experiments could be a consequence of the pore geometry,
602 which resembles the actual NPC much better than flat surfaces. Here, our measurements
603 on large pores above 100 nm diameter provide an effective bridge between nanopore
604 studies and surface techniques such as QCM-D and SPR. Note that the reported height
605 change of the Nsp1 brushes serves as an approximate quantification due to the high
606 pore-to-pore variability in the dataset. Additionally, we acknowledge that 1 μ M of Kap95 is
607 still considerably below physiological Kap95 concentrations of around 4 μ M (*Kalita et al.,*
608 *2022*), so it is hard to relate the effect we observed to the physiological NPC.

609 We have limited this study to a case study with single combination of FG-Nup (Nsp1) and
610 NTR (Kap95), but our approach could easily be expanded to other FG-Nups, transporters,
611 or control proteins. The NPC contains two main classes of FG-Nups that differ in their
612 cohesiveness, amino acid composition and localization within the central channel. For

instance, FxFG-type FG-Nups, such as Nsp1, contain mainly FxFG repeats and have a high content of charged amino acids in its extended domain. Consequently, they are more extended and do not phase separate (Yamada et al., 2010; Dekker et al., 2022) but instead form percolating hydrogels at high concentration (Frey et al., 2006). These FxFG-Nups are predominantly anchored on the nuclear and cytosolic side of the NPC, with Nsp1 being an exception that is also located in the center (Kim et al., 2018). On the other hand, GLFG-type FG-Nups contain a low amount of charged amino acids and, as a result, are more cohesive and prone to phase separation (Schmidt and Görlich, 2015; Dekker et al., 2022). They are localized mainly at the central channel of the NPC, where they might be necessary to form the selective barrier (Strawn et al., 2004; Adams et al., 2016). While we observed moderate selectivity ratios of 2 to 6 for Nsp1, we expect that more cohesive GLFG-type FG-Nups, such as Nup100 in yeast or Nup98 in humans, would form a tighter, more selective barrier with lower permeability for BSA. While we did not observe a significant obstruction of the diffusion of Kap95 through the Nsp1 mesh, the dense FG-Nup phase formed by GLFG-type FG-Nups could pose a tighter barrier for Kap95 diffusion. Recent efforts have also focused on designing FG-Nups with desired properties from the bottom up, where our assay could provide important information on the relation between protein properties and transport selectivity and kinetics (Fragasso et al., 2021; Ng et al., 2021, 2022).

Finally, our approach could be used to study the full systems for protein import or export with all required cofactors, including, for example, the Ran system that provides directionality to molecular transport across the nuclear envelope (Görlich and Kutay, 1999). In particular, by using specific labeling coupled with multicolor detection it will be possible to simultaneously follow different components of the transport machinery, providing direct mechanistic insights into important steps of the transport cycle, such as cargo release or transport factor recycling. An open question in the field also regards how large cargoes such as mRNA (De Magistris, 2021) or even viral particles (Burdick et al., 2020; Zila et al., 2021) can pass through the NPC, which could be readily tested with our assay. We envision that NPC mimics based on metal nanopores will continue to provide important answers to key questions on the mechanism of nucleocytoplasmic transport.

Methods and Materials

Fabrication of freestanding Pd ZMWs

Fabrication of nanopores in freestanding palladium membranes was performed as shown in Figure 1 based on the procedures described in Klughammer and Dekker (2021) with minor modifications. Freestanding 20 nm SiN_x membranes were manufactured as de-

scribed in *Janssen et al. (2012)* and cleaned using oxygen plasma for 2 min at 100 W at an oxygen flow rate of 200 ml/min using a PVA Tepla 300 plasma cleaner. As an adhesion layer, 3 nm titanium was deposited onto the SiN_x membrane at 0.05 nm/sec under a base pressure of 3×10^{-6} torr in a Temescal FC2000 e-gun evaporator, immediately followed by a 100 nm layer of Pd at 0.1 nm/sec to 0.2 nm/sec with a base pressure below 2×10^{-6} torr without venting the chamber in between.

The SiN_x and Ti layers were removed by dry etching using CHF₃ at a flow of 50 SCCM and O₂ at a flow of 2.5 SCCM for 10 min at 52 W power in a Sentech Etchlab 200 plasma etcher, resulting in an effective chamber pressure of 1.2 Pa. To ensure that the SiN_x and Ti layers are completely removed, the etch time was chosen to partly etch into the Pd layer, resulting in a palladium membrane thickness of 90 nm after etching, estimated by cutting a slit into the palladium membrane using FIB milling and measuring the resulting wall thickness using an SEM on a FEI Helios G4 CX microscope. On the same FIB/SEM we developed a protocol to reproducibly mill circular nanopores into Pd membranes: After adjusting the eucentric height, the ion column for a 1.1 pA Ga beam at 30 kV acceleration voltage was automatically aligned on a reference sample of gold sputtered on carbon.

A test pore was then milled and inspected for circularity at high magnification using the immersion mode of the SEM. If the test pore was not circular due to astigmatism of the Ga beam, the ion column alignment was repeated. Linear pore arrays with surrounding markers were then milled on the membrane using an automatic script written in Nanobuilder. Individual pores were made at a distance of at least 9 μm, in order to avoid later cross talk between the individual pores during the experiment. An additional marker pattern without pore was added for the identification of individual pores on the membrane. Subsequently, each membrane was examined on a JEOL JEM-1400 transmission electron microscope (TEM) for integrity and the minimum and maximum diameter was determined for each pore from the TEM images. The two diameters typically differed by less than 10 %. Pore sizes stated in this study are the arithmetic means of these two values.

Chemicals, protein purification and protein labeling

MUHEG ((11-Mercaptoundecyl)hexa(ethylene glycol)) with 90 % purity (Sigma-Aldrich) was dissolved at a concentration of 200 mM in degassed ethanol. Aliquots were prepared under nitrogen atmosphere and stored at -20 °C until use. 350 Da thiol-PEG (Polyethylene glycol) with more than 95 % purity (Nanocs Inc., New York) was aliquoted under nitrogen atmosphere and stored at -20 °C until use. Nsp1 protein (*Appendix 12*) was kindly provided by the Görlich lab (Göttingen, Germany) in lyophilized form and resuspended in denaturing buffer at 10 μM. For long term storage, samples were snap frozen in liquid

nitrogen and stored at -80°C . Alexa488 labeled BSA was purchased from Invitrogen, Thermo Fisher. On average one BSA molecule was labeled with 6 Alexa488 molecules. It was diluted in PBS to a final concentration of $72.6\ \mu\text{M}$. The diluted sample was dialysed on ice using 10K Slide-A-Lyzer Dialysis Cassettes for 3 mL for 24 h, exchanging the 250 mL PBS dialysis buffer four times until no free fluorophores were detectable in the dialysis buffer in an FCS experiment. The protein solution was snap frozen in aliquots and stored at -20°C until use in the experiment. Unlabeled BSA was purchased from Thermo Fisher (Ultra Pure BSA (50 mg/ml), Invitrogen), diluted to 5 mg/ml split into aliquots, snap frozen and stored at -20°C until use in the experiment. Kap95 (**Appendix 12**) was purified as described previously (*Fragasso et al., 2021*) and C-terminally labeled with AZDye647, which is structurally identical to AlexaFluor647, using sortase-mediated ligation. Sortase labeling was performed following published protocols at 50-fold excess of the dye-triglycine conjugate (Click Chemistry Tools, USA) for 1 h at room temperature in Tris buffer (50 mM Tris, 150 mM NaCl, pH 7.4) (*Guimaraes et al., 2013*). Unreacted dyes were removed by size exclusion chromatography on a Superdex S200 column pre-equilibrated with PBS buffer. To fully remove free fluorophores, labeled Kap95 was further dialyzed as described above. We used two separate preparations of the labeled Kap95 with 70 % and 62.5 % degree of labeling and $16.8\ \mu\text{M}$ and $5.9\ \mu\text{M}$ stock concentrations. The stock solutions were split into aliquots and stored at -80°C after snap-freezing. The purity of Nsp1 and Kap95 samples was assessed using sodium dodecyl sulfate-polyacrylamide gel electrophoresis (SDS-PAGE).

Cleaning and surface grafting of Pd

Grafting of thiols to Pd surface

In order to make Pd accessible for thiol binding, a cleaning procedure was performed. Two different cleaning methods were used depending on the grafting solution. For ethanol based grafting solutions we performed cleaning in hydrogen peroxide and for PBS based grafting solutions we performed cleaning in boiling ethanol.

For MUHEG grafting, chips were mounted in a custom built teflon holder, rinsed with DI water and submersed in $>99\%$ isopropylalcohol to remove bubbles. 30 % hydrogen peroxide was brought to 45°C in a water bath. The chip was rinsed in DI water and then submersed in the hot H_2O_2 for 15 min. MUHEG solution was prepared by diluting stock solutions in absolute ethanol to a final concentration of $250\ \mu\text{M}$. The solution was sonicated for 5 min to 15 min at 20°C . The chip was taken out of the teflon holder, washed in DI water and submersed fully in the MUHEG solution for grafting. During the grafting, the chips were gently shaken over night at 450 rpm for 11 h to 22 h at 20°C . Before mounting, the chip was washed in ethanol for 15 min, dried under a stream of nitrogen

720 and mounted within minutes after drying.

721 For Nsp1 grafting, chips were mounted in a teflon holder and rinsed with DI water.
722 Pure Ethanol was heated in a water bath until boiling to 78°. The chip was submersed
723 in boiling ethanol for 15 min and rinsed with DI water. Boiling ethanol was proposed to
724 efficiently remove organic residues from silver surfaces *Majid et al. (2003)*. Nsp1 aliquots
725 were diluted to 1 µM in PBS buffer. Tris-(2-Carboxyethyl)phosphine, Hydrochloride (TCEP,
726 Supelco, Sigma-Aldrich) was added until a final concentration of 1 mM to reduce potential
727 disulfide bonds. The solution was briefly vortexed and then incubated for 15 min at 20 °C.
728 Chips were incubated in the Nsp1 solution for 1 h while shaking at 450 rpm. The chips
729 were then transferred to a solution containing 2 mM 350-Da PEG in PBS buffer with 5 mM
730 TCEP for 1 h. Before mounting, the chip was washed in PBS for 15 min by shaking at
731 450 rpm, subsequently rinsed with DI water and dried under a flow of nitrogen. The chip
732 was reimmersed in buffer within minutes after drying.

733 QCM-D experiments

734 QSense Analyzer gold-coated quartz QCM-D chips were purchased from Biolin Scientific,
735 Västra Frölunda, Sweden. Similar to the freestanding Pd membranes, a 3 nm titanium
736 layer was deposited onto the Au surface at 0.05 nm/sec and a 100 nm layer of Pd was
737 evaporated at 0.1 nm/sec with a base pressure below 2×10^{-6} torr in a Temescal FC2000
738 e-gun evaporator. The cleaned chips were mounted in the flow cell in dried state. The
739 flow cell was filled with buffer or ethanol until a stable base line was detected, before the
740 respective grafting solution was applied. The experiments were conducted at 21 °C. See
741 *Appendix 1* for details.

742 Experimental setup and measurement

743 Freestanding Pd membranes were mounted in a modified flow cell as described in *Keyser*
744 *et al. (2006)* and are very comparable to what was used in *Klughammer and Dekker (2021)*.
745 The reservoir was made from a polydimethylsiloxane (PDMS) ring that was pressed onto
746 the membrane chip. The reservoir volume was approximately 3 µL. To avoid cross-
747 contamination, the reservoir ring was discarded after each experiment, while the flow
748 channel on the detection side was reused several times.

749 After drying, the chips were immediately mounted within minutes such that the Pd
750 membrane faced towards the flow channel and the microscope objective. Nsp1-coated
751 chips were immediately immersed in PBS buffer and contact with ethanol was avoided.
752 MUHEG coated chips were flushed with 1:1 ethanol:water mixtures to remove air bubbles.
753 The conductance of the chip was measured using Ag/AgCl electrodes and an Axopatch
754 200B amplifier (Molecular Devices) to check that they were properly wetted. The flow
755 cell was subsequently mounted onto the stage of the confocal microscope. We applied

a flow to the channel on the detection side using a Fluigent Microfluidic Flow Control System to prevent the accumulation of fluorophores. We applied 50 hPa of pressure to a vessel directly connected via 1 m of tubing (Masterflex Microbore Transfer Tubing, Tygon ND-100-80) to the flow cell. The outlet of the flow cell was connected to another tubing of the same length. Due to symmetry, this results in an estimated pressure of 25 hPa at the location of the membrane. The flow of buffer was measured to be 0.7 mL h^{-1} . Since the applied pressure induces a backflow through the pores against the concentration gradient, we ensured that the flow was constant between different experiments such that the relative event rates remain unchanged. Experiments were performed at $21 \pm 1^\circ \text{C}$ in a temperature and vibration controlled room.

After positioning the membrane in the field of view, markers were localized using transmitted light and the laser focus was centered on the nanopore between the markers. Data was acquired on a Picoquant Microtime 200 microscope using the Symphotime software. We used a 60x Olympus LUMFLN60XW water immersion objective which provides a working distance of 1.5 mm to enable imaging of the mounted chip. Excitation lasers at wavelengths of 640 nm and 485 nm were operated in pulsed interleaved excitation at a repetition frequency of 40 MHz and 10 μW power as measured at the imaging plane. Before each experiment, the collar ring of the objective was aligned by optimizing the molecular brightness of a solution of Alexa488 fluorophores. The emission light was passed through a 50 μm pinhole, split by a dichroic mirror, and filtered by either a 600/75 or 525/50 optical band pass filters (Chroma, USA) before being focused on single-photon avalanche-diode detector (PD5CTC and PD1CTC, Micro Photon Devices, Italy).

For each experiment the same measurement scheme was followed as shown in **Figure 3** and described in detail in **Appendix 4**. In this scheme, we continuously increased the Kap95 concentration during the experiment to avoid accumulation of Kap95 in the Nsp1 brushes. Before decreasing the BSA concentration, a wash with 5 % Hexane-1-6-diol was performed. For experiments involving pores of diameter larger than 70 nm, the labeled protein was mixed with unlabeled protein at a ratio of 1:4 to avoid that the event rate exceeded the detection limit. During the translocation experiment, the respective dilutions of proteins were prepared with PBS and kept on ice before pipetting them into the reservoir. After the experiment, translocations of free Alexa647 and Alexa488 were measured to exclude that pores were clogged (see **Appendix 3—Figure 1**).

Data analysis

Event rate detection was performed using a custom written python script based on several packages *Hunter (2007)*; *Virtanen et al. (2020)*; *Wes McKinney (2010)*; *van der Walt et al. (2011)*; *Perez and Granger (2007)*. The analysis pipeline was based on previously

published work (*Klughammer and Dekker, 2021; Klughammer, 2020*) and is deposited in an open repository *Klughammer et al. (2023a)*. In brief, photon bursts were detected using a change point detection algorithm (*Watkins and Yang, 2005*) that detects discrete changes of the photon statistics from the single-photon arrival times. Background events were discarded based on an empirical criterion. In previous work, we had interpreted subsequent events on the millisecond timescale as reentry events of the same molecule (*Klughammer and Dekker, 2021*). To avoid potential biases, no combination of closely spaced events was performed here. However, we could not exclude that molecules may re-enter the laser focus after translocation. Normalized event rates were calculated by dividing the measured event rate by the degree of labeling and the concentration of the respective protein. A purely statistical uncertainty of the event rate was estimated from the assumption that translocation events follow Poisson statistics.

Over the course of the study, several data sets had to be discarded based on the following criteria. First, we discarded a data set for which a lower excitation power was used (8 pores). Next, we discarded the data of 4 pores that showed negligible protein translocations due to clogging. For three full data sets totalling 24 pores, we found a significant reduction in the amount of photons detected per molecule which biased the event detection (see *Appendix 13*—Figures 1,2 for details). Further, in cases where the normalized Kap95 event rate differed significantly for one out of the three measurements for the same concentration, the condition was removed (17 conditions). When there was doubt about perfect focusing of the lasers for certain pores, these were discarded from further analysis (2 pores). Finally, if there was any indication of sticking of proteins to the pore surface, as visible from the FCS curve, these pores were removed (2 pores). In total, 46 pores (27 with Nsp1 coating, 19 open pores) with 400 time traces (248 for Nsp1-coated pore, 152 for open pores) from seven individual measurement days and chips were used for the final analysis.

Normalized event rates in *Figure 4* and *Figure 5* were fitted using *Equation 2* and *Equation 3* by optimizing the functions to the individual translocation datasets, taking into account their statistical errors using the least squares method (see *Appendix 6*—*Figure 1*).

Fluorescence Correlation Spectroscopy (FCS) and lifetime analyses were performed using the PAM software package (*Schrimpf et al., 2018*). For fitting of the FCS curves, the size of the confocal volume was determined from measurements of the free dyes Alexa647 and Alexa488 by fitting a single-component diffusion model with triplet state. The diffusion coefficients at 21 °C were set to 297 $\mu\text{m}^2/\text{s}$ for Alexa647 and 372 $\mu\text{m}^2/\text{s}$ for Alexa488, based on the values provided in (*Kapusta, 2020*). The axial and lateral sizes of the confocal volume, ω_z and ω_r , were fixed for further analysis. FCS amplitudes and diffusion coefficients were subsequently fitted for each dataset separately. For

829 Kap95–Alexa647 containing samples, the triplet state was fitted individually for each
830 FCS curve. Fluorescence lifetimes were determined by a single-exponential tail fit of the
831 fluorescence decays, ignoring the first 1160 ps of the decay in order to reduce variations
832 introduced by the instrument response function.

833 Coarse-grained molecular dynamics simulations

834 Coarse-grained molecular dynamics simulations were performed with the implicit-solvent
835 1BPA-1.1 model for intrinsically disordered proteins (*Ghavami et al., 2013, 2014; Jafarinia*
836 *et al., 2020, 2022; Dekker et al., 2022*). This residue-scale model discriminates between all
837 20 amino acids through residue-specific hydrophobic, charge and cation- π interactions,
838 and accounts for the sequence-specific backbone stiffness (see *Dekker et al. (2022)* for
839 a detailed description of the 1BPA-1.1 model). Simulations were performed with the
840 GROMACS (*van der Spoel et al., 2005*) molecular dynamics software (version 2019.4)
841 using a time step of 0.02 ps and inverse friction coefficient $\gamma^{-1} = 50$ ps for the Langevin
842 dynamics integrator. All nanopores were simulated at 294 K and a salt concentration of
843 150 mM KCl by setting the Debye screening constant $\kappa = 1.27 \text{ nm}^{-1}$. Nanopore scaffolds
844 were generated from partly-overlapping sterically inert beads with a diameter of 3.0 nm
845 with their centres placed 1.5 nm apart. Nsp1 proteins were then grafted to the scaffold
846 wall at their C-terminal Cys-residue, with the N-terminus of the Nsp1 proteins pointing
847 out of the nanopore occlusion. Nanopore systems were equilibrated for 1.0×10^8 steps
848 (2 μ s), followed by a production run of 2.5×10^8 steps (5 μ s) to generate the equilibrium
849 trajectories.

850 Axi-radial density maps were obtained from the equilibrium trajectories using the
851 *gmx densmap* utility of GROMACS, where a sample was taken every 5000 steps (100 ps).
852 The 2D number-density maps created by GROMACS (in nm^{-3}) were converted to mass
853 densities (in mg/mL) using the average mass of an Nsp1 residue (~ 100 Da). We note
854 that the obtained densities are slightly lower than observed previously for 20 nm-pores
855 (*Ananth et al., 2018*), as there a simplified average residue mass of 120 Da was used.

856 Void analysis method and calculation of translocation rates

857 Potential of mean force (PMF) curves for protein translocation across the Nsp1 pores
858 obtained using the void analysis method of *Winogradoff et al. (2022)*. The simulation
859 volume was converted into a 3D grid where each voxel has a side length of 6 Å. For each
860 instantaneous configuration of the Nsp1 mesh, we probed for each voxel whether a
861 spherical probe with the size of the translocating protein (BSA or Kap95, see *Appendix 10*)
862 could be placed at its center without sterically overlapping with an Nsp1 bead or the
863 pore scaffold. The resulting 3D void map was then converted into a 1D potential occu-
864 pancy map by calculating the percentage of available voxels for each slice along the pore

axis. The potential occupancy function was calculated for every 5×10^4 steps (1 ns) of the equilibrium trajectory. The trajectory average of the potential occupancy function was converted into an effective PMF curve through Boltzmann inversion, as shown in [Appendix 10](#)—Figures 1 and 2 (see [Winogradoff et al. \(2022\)](#) for a more detailed description of the procedure). The analysis was performed with the codes provided by the paper, where a custom constraint was used for each nanopore to exclude the Pd layer volume from the void analysis. Protein translocation rates were obtained from the PMF barriers, calculated by averaging the PMF over a specified range ([Appendix 10](#)—Figures 1 and 2), using an Arrhenius relation:

$$k = k_0 \exp(-\Delta E/k_B T), \quad (6)$$

in which ΔE is the energy barrier that the translocating protein has to overcome and k_0 is a proportionality constant that is obtained by fitting the calculated rates to the experimental event rates for open pores (see [Appendix 10](#)). This resulted in two independent scaling factors, $k_{0,BSA}$ and $k_{0,Kap95}$, for BSA and Kap95, respectively. We note that the use of protein-specific scaling factors follows from the observation that the void analysis method does not take into account any diffusion properties of the translocating protein. Nevertheless, the same scaling factor was used for both open and Nsp1-coated pores.

To assess the path that BSA proteins take through the Nsp1 mesh, we determined the time-averaged distribution of the ‘voids’ in the Nsp1 mesh. This was done by computing the 3D void map for each instantaneous configuration of the Nsp1 meshwork, and calculating the simulation average. This time-averaged void map represents the probability for each voxel to accommodate a BSA protein. The 3D void map was then circumferentially averaged around the pore’s axis to obtain the 2D (r, z) void map shown in [Figure 5 F](#).

Finite-difference time-domain (FDTD) simulations

Three-dimensional FDTD simulations were performed using Lumerical FDTD (ANSYS, Inc., USA). The surrounding medium was modeled as water with a refractive index of 1.33. The refractive index of the 100 nm thick palladium membrane was modelled according to [Palik \(1998\)](#). For the simulation of the excitation field, the ZMW was illuminated by a pulse from a total-field scattered-field source polarized in the x-direction, set as a plane wave source for widefield excitation and a Gaussian source with a numerical aperture of 1.2 for focused excitation. The simulation box size was $1 \times 1 \times 0.8 \mu\text{m}^3$ for widefield excitation. A larger box of $4 \times 4 \times 0.8 \mu\text{m}^3$ was required for the Gaussian source to correctly model the focused beam. The electromagnetic field intensity distribution was monitored in the xz and yz planes passing through the center of the pore and in the xy plane at the pore entry with a grid resolution of 5 nm ([Appendix 2](#)). To model the dipole emission in the proximity of the ZMW, a dipole emitter was placed at varying z-positions at the center of the pore.

For the estimation of the quantum yield, the radiated power was integrated over all sides of the box (see below). For the estimation of the detection efficiency, the emitted power was integrated only on the detection side of the ZMW. To model isotropic emission, all reported quantities were averaged over horizontal and vertical orientations of the dipole. The power was only weakly affected by the lateral position of the emitter with respect to the center of the pore (data not shown) (Levene *et al.*, 2003). The simulated electric field intensities $|E|^2$ are shown in **Appendix 2**—Figures 1–3.

Estimation of fluorescence lifetimes

In the absence of the ZMW, the decay rate of the excited molecule is given by $\gamma^0 = \gamma_r^0 + \gamma_{nr}^0$, where γ_r^0 and γ_{nr}^0 are the radiative and non-radiative decay rates. Note that γ_{nr}^0 accounts only for internal processes that lead to non-radiative relaxation to the ground state and was assumed to be unchanged in the presence of the ZMW. The intrinsic quantum yield is defined as $\Phi_0 = \gamma_r^0 / (\gamma_r^0 + \gamma_{nr}^0)$ and was estimated from the measured fluorescence lifetimes τ_0 for BSA–Alexa488 and Kap95–Alexa647 of 2.30 ns and 1.37 ns, respectively, as:

$$\Phi_0 = \frac{\tau_0}{\tau_{lit}} \Phi_{lit}, \quad (7)$$

where τ_{lit} and Φ_{lit} are reference values for the free dyes ($\tau_{lit} = 4.0$ ns and $\Phi_{lit} = 0.80$ for Alexa488, $\tau_{lit} = 1.37$ ns and $\Phi_{lit} = 0.33$ for Alexa647) (Sanabria *et al.*, 2020; Hellenkamp *et al.*, 2018). This led to quantum yields of $\Phi_0 = 0.46$ and 0.39 for BSA–Alexa488 and Kap95–Alexa647, respectively. Note that the quantum yield of Alexa647 increased slightly due to steric restriction when attached to the protein, an effect known as protein-induced fluorescence enhancement (Stennett *et al.*, 2015).

In the presence of the nanostructure, the radiative decay rate γ_r is modified and an additional non-radiative rate γ_{loss} is introduced because part of the power emitted by the dipole is absorbed by the metal nanostructure. The quantum yield Φ in the presence of the ZMW was given by Bharadwaj and Novotny (2007):

$$\Phi = \frac{\gamma_r / \gamma_r^0}{\gamma_r / \gamma_r^0 + \gamma_{loss} / \gamma_r^0 + (1 - \Phi_0) / \Phi_0}, \quad (8)$$

where γ_r^0 and γ_r are the radiative rates in the absence and the presence of the ZMW respectively. The absolute decay rates γ_r , γ_{loss} , and γ_r^0 cannot be obtained from FDTD simulations. However, relative rates with respect to the radiative rate in the absence of the ZMW, γ_r^0 , can be estimated from the power P radiated by the dipole (Novotny and Hecht, 2006) as:

$$\frac{\gamma_r}{\gamma_r^0} = \frac{P_{ff}}{P_r^0} \text{ and } \frac{\gamma_{loss}}{\gamma_r^0} = \frac{P_r}{P_r^0} - \frac{P_{ff}}{P_r^0}, \quad (9)$$

where P_r and P_r^0 are the powers radiated by the dipole in the presence and absence of the ZMW, and P_{ff} is the power that is radiated into the far-field in the presence of the

931 ZMW. The fluorescence lifetime τ is given by the inverse of the sum of all de-excitation
932 rates and can be obtained from eq. 8 using the relation $\tau = \Phi/\gamma_r$ as:

$$\tau = \frac{1}{\gamma_r + \gamma_{\text{loss}} + \gamma_{nr}^0} = \frac{1/\gamma_r^0}{\gamma_r/\gamma_r^0 + \gamma_{\text{loss}}/\gamma_r^0 + (1 - \Phi_0)/\Phi_0}, \quad (10)$$

933 Here, the intrinsic radiative rate γ_r^0 in the numerator was estimated as $\gamma_r^0 = \Phi_{\text{lit}}/\tau_{\text{lit}}$. The
934 detection efficiency η was estimated from the ratio of the power radiated towards the
935 lower (detection) side of the ZMW, P_r^{z-} , to the total radiated power:

$$\eta = \frac{P_{\text{ff}}^{z-}}{P_{\text{ff}}}. \quad (11)$$

936 Finally, the total detected signal as a function of the z-position of the emitter with respect
937 to the ZMW was computed as the product of the excitation intensity $I_{\text{ex}}(z)$, detection
938 efficiency $\eta(z)$, and quantum yield $\Phi(z)$ as:

$$S(z) \propto I_{\text{ex}}(z)\eta(z)\Phi(z) \quad (12)$$

939 and normalized to unity. The computed detection efficiency η , quantum yield Φ , detected
940 signal $S(z)$ and lifetime τ as a function of the z-position within the ZMW are shown in
941 **Appendix 2—Figure 4**. The average fluorescence lifetimes over the signal profile $S(z)$
942 correspond well to the experimental fluorescence lifetimes measured in the translocation
943 experiments (**Appendix 2—Figure 4**).

944 Data availability

945 All single photon counting data is deposited in the open Photon-HDF5 file format (*In-*
946 *gargiola et al., 2016*) together with the unprocessed TEM images of nanopores are in a
947 repository at (*Klughammer et al., 2023b*)).

948 Acknowledgments

949 We thank Eli van der Sluis, Ashmiani van den Berg, and Angeliki Goutou for support
950 with protein expression and purification. We thank Paola de Magistris, Xin Shi, Sonja
951 Schmid, and Biswajit Pradhan for fruitful discussions. The Nsp1 protein used in this study
952 was a kind gift from Dirk Görlich. Financial support was provided by the NWO program
953 OCENW.GROOT.2019.068, ERC Advanced Grant no. 883684, and the NanoFront and
954 BaSyC programs of NWO/OCW. A.B. acknowledges funding from the European Union's
955 Horizon 2020 research and innovation program under the Marie Skłodowska-Curie Grant
956 agreement no. 101029907.

Author Contributions

N.K.: Conceptualisation, Methodology (lead), Software, Validation, Formal Analysis, Investigation (lead), Data Curation, Writing – Original Draft Preparation (lead), Writing – Review & Editing, Visualization (lead), A.B.: Methodology, Software, Validation, Formal Analysis, Resources, Investigation, Writing – Original Draft Preparation, Writing – Review & Editing, Visualization, Funding Acquisition M.D.: Methodology, Software, Formal Analysis (lead), Investigation, Writing – Original Draft Preparation , Writing – Review & Editing, Visualization A.F.: Conceptualisation, Methodology, Resources, Writing – Review & Editing P.O.: Supervision, Funding Acquisition, Writing – Review & Editing C.D.: Conceptualization, Writing – Review & Editing, Supervision, Funding Acquisition

N.K. performed nanofabrication, translocation experiments and the data analysis. N.K. and A.B. developed and optimized the experimental protocol. A.B. and A.F. performed protein labeling and purification. M.D. performed coarse-grained molecular dynamics simulations. N.K., A.B., and M.D. designed figures. N.K. and A.B. wrote the initial draft.

References

- Adams RL**, Terry LJ, Wente SR. A Novel *Saccharomyces cerevisiae* FG Nucleoporin Mutant Collection for Use in Nuclear Pore Complex Functional Experiments. *G3 Genes|Genomes|Genetics*. 2016 01; 6(1):51–58. <https://doi.org/10.1534/g3.115.023002>, doi: 10.1534/g3.115.023002.
- Akey CW**, Singh D, Ouch C, Echeverria I, Nudelman I, Varberg JM, Yu Z, Fang F, Shi Y, Wang J, Salzberg D, Song K, Xu C, Gumbart JC, Suslov S, Unruh J, Jaspersen SL, Chait BT, Sali A, Fernandez-Martinez J, et al. Comprehensive structure and functional adaptations of the yeast nuclear pore complex. *Cell*. 2022; 185(2):361–378.e25. <https://www.sciencedirect.com/science/article/pii/S0092867421014537>, doi: <https://doi.org/10.1016/j.cell.2021.12.015>.
- Ananth AN**, Mishra A, Frey S, Dwarkasing A, Versloot R, van der Giessen E, Görlich D, Onck P, Dekker C. Spatial structure of disordered proteins dictates conductance and selectivity in nuclear pore complex mimics. *eLife*. 2018 feb; 7:e31510. <https://doi.org/10.7554/eLife.31510>, doi: 10.7554/eLife.31510.
- Andersson J**, Svirelis J, Ferrand-Drake del Castillo G, Sannomiya T, Dahlin A. Surface plasmon resonance sensing with thin films of palladium and platinum – quantitative and real-time analysis. *Phys Chem Chem Phys*. 2022; 24:4588–4594. <http://dx.doi.org/10.1039/D1CP05381G>, doi: 10.1039/D1CP05381G.
- Aramburu IV**, Lemke EA. Floppy but not sloppy: Interaction mechanism of FG-nucleoporins and nuclear transport receptors. *Seminars in Cell & Developmental Biology*. 2017; 68:34–41. <https://www.sciencedirect.com/science/article/pii/S108495211730294X>, doi: <https://doi.org/10.1016/j.semcdb.2017.06.026>, nuclear pores.

- 992 **Auger T**, Mathé J, Viasnoff V, Charron G, Di Meglio JM, Auvray L, Montel F. Zero-Mode Waveguide De-
993 tection of Flow-Driven DNA Translocation through Nanopores. *Phys Rev Lett*. 2014 7; 113:028302.
994 <https://link.aps.org/doi/10.1103/PhysRevLett.113.028302>, doi: 10.1103/PhysRevLett.113.028302.
- 995 **Beck M**, Hurt E. The nuclear pore complex: understanding its function through structural insight.
996 *Nature Reviews Molecular Cell Biology*. 2017 Feb; 18(2):73–89. [https://doi.org/10.1038/nrm.2016.](https://doi.org/10.1038/nrm.2016.147)
997 [147](https://doi.org/10.1038/nrm.2016.147), doi: 10.1038/nrm.2016.147.
- 998 **Bharadwaj P**, Novotny L. Spectral dependence of single molecule fluorescence enhancement.
999 *Optics Express*. 2007; 15(21):14266–14274.
- 1000 **Burdick RC**, Li C, Munshi M, Rawson JMO, Nagashima K, Hu WS, Pathak VK. HIV-1 uncoats
1001 in the nucleus near sites of integration. *Proceedings of the National Academy of Sci-*
1002 *ences*. 2020; 117(10):5486–5493. <https://www.pnas.org/doi/abs/10.1073/pnas.1920631117>, doi:
1003 10.1073/pnas.1920631117.
- 1004 **Celetti G**, Paci G, Caria J, VanDelinder V, Bachand G, Lemke EA. The liquid state of FG-nucleoporins
1005 mimics permeability barrier properties of nuclear pore complexes. *Journal of Cell Biology*. 2019
1006 11; 219(1). <https://doi.org/10.1083/jcb.201907157>, doi: 10.1083/jcb.201907157, e201907157.
- 1007 **Chowdhury R**, Sau A, Musser SM. Super-resolved 3D tracking of cargo transport through nu-
1008 clear pore complexes. *Nature Cell Biology*. 2022 Jan; 24(1):112–122. [https://doi.org/10.1038/](https://doi.org/10.1038/s41556-021-00815-6)
1009 [s41556-021-00815-6](https://doi.org/10.1038/s41556-021-00815-6), doi: 10.1038/s41556-021-00815-6.
- 1010 **De Magistris P**. The Great Escape: mRNA Export through the Nuclear Pore Complex. *International*
1011 *Journal of Molecular Sciences*. 2021; 22(21). <https://www.mdpi.com/1422-0067/22/21/11767>, doi:
1012 10.3390/ijms222111767.
- 1013 **Dechadilok P**, Deen WM. Hindrance Factors for Diffusion and Convection in Pores. *Industrial &*
1014 *Engineering Chemistry Research*. 2006; 45(21):6953–6959. <https://doi.org/10.1021/ie051387n>, doi:
1015 10.1021/ie051387n.
- 1016 **Dekker M**, van der Giessen E, Onck PR. Liquid-liquid phase separation of intrinsically disordered
1017 FG-Nups is driven by highly-dynamic hydrophobic FG-motifs. *bioRxiv*. 2022; [https://www.biorxiv.](https://www.biorxiv.org/content/early/2022/09/21/2022.09.20.508740)
1018 [org/content/early/2022/09/21/2022.09.20.508740](https://www.biorxiv.org/content/early/2022/09/21/2022.09.20.508740), doi: 10.1101/2022.09.20.508740.
- 1019 **Fragasso A**, de Vries HW, Andersson J, van der Sluis EO, van der Giessen E, Dahlin A, Onck PR, Dekker
1020 C. A designer FG-Nup that reconstitutes the selective transport barrier of the nuclear pore complex.
1021 *Nature Communications*. 2021 Mar; 12(1):2010. <https://doi.org/10.1038/s41467-021-22293-y>, doi:
1022 10.1038/s41467-021-22293-y.
- 1023 **Fragasso A**, de Vries HW, Andersson J, van der Sluis EO, van der Giessen E, Onck PR, Dekker
1024 C. Transport receptor occupancy in nuclear pore complex mimics. *Nano Research*. 2022 Jul;
1025 <https://doi.org/10.1007/s12274-022-4647-1>, doi: 10.1007/s12274-022-4647-1.

1026 **Frey S**, Görlich D. A Saturated FG-Repeat Hydrogel Can Reproduce the Permeability Properties
1027 of Nuclear Pore Complexes. *Cell*. 2007; 130(3):512 – 523. [http://www.sciencedirect.com/science/
1028 article/pii/S009286740700791X](http://www.sciencedirect.com/science/article/pii/S009286740700791X), doi: <https://doi.org/10.1016/j.cell.2007.06.024>.

1029 **Frey S**, Richter RP, Görlich D. FG-Rich Repeats of Nuclear Pore Proteins Form a Three-Dimensional
1030 Meshwork with Hydrogel-Like Properties. *Science*. 2006; 314(5800):815–817. [https://science.
1031 sciencemag.org/content/314/5800/815](https://science.sciencemag.org/content/314/5800/815), doi: 10.1126/science.1132516.

1032 **Ghavami A**, van der Giessen E, Onck PR. Coarse-Grained Potentials for Local Interactions in
1033 Unfolded Proteins. *Journal of Chemical Theory and Computation*. 2013 1; 9:432–440. <https://pubs.acs.org/doi/10.1021/ct300684j>, doi: 10.1021/ct300684j.

1034
1035 **Ghavami A**, Veenhoff L, van der Giessen E, Onck P. Probing the Disordered Domain of the Nu-
1036 clear Pore Complex through Coarse-Grained Molecular Dynamics Simulations. *Biophysical
1037 Journal*. 2014 9; 107:1393–1402. <https://linkinghub.elsevier.com/retrieve/pii/S000634951400808X>,
1038 doi: 10.1016/j.bpj.2014.07.060.

1039 **Görlich D**, Kutay U. Transport Between the Cell Nucleus and the Cytoplasm. *Annual Review of Cell
1040 and Developmental Biology*. 1999; 15(1):607–660. <https://doi.org/10.1146/annurev.cellbio.15.1.607>,
1041 doi: 10.1146/annurev.cellbio.15.1.607, PMID: 10611974.

1042 **Gregor I**, Chizhik A, Karedla N, Enderlein J. Metal-induced energy transfer. *Nanophotonics*. 2019;
1043 8(10):1689–1699. <https://doi.org/10.1515/nanoph-2019-0201>, doi: doi:10.1515/nanoph-2019-0201.

1044 **Guimaraes CP**, Witte MD, Theile CS, Bozkurt G, Kundrat L, Blom AEM, Ploegh HL. Site-specific C-
1045 terminal and internal loop labeling of proteins using sortase-mediated reactions. *Nature Protocols*.
1046 2013 Sep; 8(9):1787–1799. <https://doi.org/10.1038/nprot.2013.101>, doi: 10.1038/nprot.2013.101.

1047 **Hellenkamp B**, Schmid S, Doroshenko O, Opanasyuk O, Kühnemuth R, Rezaei Adariani S, Ambrose
1048 B, Aznauryan M, Barth A, Birkedal V, Bowen ME, Chen H, Cordes T, Eilert T, Fijen C, Gebhardt
1049 C, Götz M, Gouridis G, Gratton E, Ha T, et al. Precision and accuracy of single-molecule FRET
1050 measurements—a multi-laboratory benchmark study. *Nature Methods*. 2018; 15(9):669–676.

1051 **Hunter JD**. Matplotlib: A 2D graphics environment. *Computing in Science & Engineering*. 2007;
1052 9(3):90–95. <https://doi.org/10.1109/MCSE.2007.55>, doi: 10.1109/MCSE.2007.55.

1053 **Ingargiola A**, Laurence T, Boutelle R, Weiss S, Michalet X. Photon-HDF5: An Open File For-
1054 mat for Timestamp-Based Single-Molecule Fluorescence Experiments. *Biophysical Journal*.
1055 2016; 110(1):26 – 33. <http://www.sciencedirect.com/science/article/pii/S0006349515011704>, doi:
1056 <https://doi.org/10.1016/j.bpj.2015.11.013>.

1057 **Jafarinia H**, Van der Giessen E, Onck PR. Phase Separation of Toxic Dipeptide Repeat Proteins
1058 Related to C9orf72 ALS/FTD. *Biophysical Journal*. 2020 8; 119:843–851. [https://linkinghub.elsevier.
1059 com/retrieve/pii/S0006349520305324](https://linkinghub.elsevier.com/retrieve/pii/S0006349520305324), doi: 10.1016/j.bpj.2020.07.005.

1060 **Jafarinia H**, Van der Giessen E, Onck PR. Molecular basis of C9orf72 poly-PR interference with the
1061 β -karyopherin family of nuclear transport receptors. *Scientific Reports*. 2022; 12:21324. doi:
1062 10.1038/s41598-022-25732-y.

1063 **Janssen XJA**, Jonsson MP, Plesa C, Soni GV, Dekker C, Dekker NH. Rapid manufacturing of low-
1064 noise membranes for nanopore sensors bytrans-chip illumination lithography. *Nanotechnol-*
1065 *ogy*. 2012 oct; 23(47):475302. <https://doi.org/10.1088%2F0957-4484%2F23%2F47%2F475302>, doi:
1066 10.1088/0957-4484/23/47/475302.

1067 **Jiang X**, Bruzewicz DA, Thant MM, Whitesides GM. Palladium as a Substrate for Self-Assembled
1068 Monolayers Used in Biotechnology. *Analytical Chemistry*. 2004; 76(20):6116–6121. <https://doi.org/10.1021/ac049152t>, doi: 10.1021/ac049152t, PMID: 15481961.

1069

1070 **Jovanovic-Talisman T**, Zilman A. Protein Transport by the Nuclear Pore Complex: Simple Biophysics
1071 of a Complex Biomachine. *Biophys J*. 2017; 113(1):6–14.

1072 **Jovanovic-Talisman T**, Chait BT, Rout MP. NPC mimics: probing the mechanism of nucleocy-
1073 toplasmic transport. In: *Methods in cell biology*, vol. 122 Elsevier; 2014.p. 379–393. [https://](https://www.sciencedirect.com/science/article/pii/B9780124171602000175)
1074 www.sciencedirect.com/science/article/pii/B9780124171602000175, doi: 10.1016/B978-0-12-417160-
1075 2.00017-5.

1076 **Jovanovic-Talisman T**, Tetenbaum-Novatt J, McKenney AS, Zilman A, Peters R, Rout MP, Chait BT.
1077 Artificial nanopores that mimic the transport selectivity of the nuclear pore complex. *Nature*.
1078 2008 Dec; 457:1023 EP –. <https://doi.org/10.1038/nature07600>, doi: 10.1038/nature07600.

1079 **Kalita J**, Kapinos LE, Zheng T, Rencurel C, Zilman A, Lim RYH. Karyopherin enrichment and com-
1080 pensation fortifies the nuclear pore complex against nucleocytoplasmic leakage. *Journal of*
1081 *Cell Biology*. 2022 01; 221(3). <https://doi.org/10.1083/jcb.202108107>, doi: 10.1083/jcb.202108107,
1082 e202108107.

1083 **Kapinos LE**, Huang B, Rencurel C, Lim RYH. Karyopherins regulate nuclear pore complex barrier
1084 and transport function. *Journal of Cell Biology*. 2017 09; 216(11):3609–3624. [https://doi.org/10.](https://doi.org/10.1083/jcb.201702092)
1085 [1083/jcb.201702092](https://doi.org/10.1083/jcb.201702092), doi: 10.1083/jcb.201702092.

1086 **Kapinos L**, Schoch R, Wagner R, Schleicher K, Lim RH. Karyopherin-Centric Control of Nuclear Pores
1087 Based on Molecular Occupancy and Kinetic Analysis of Multivalent Binding with FG Nucleoporins.
1088 *Biophysical Journal*. 2014; 106(8):1751 – 1762. [http://www.sciencedirect.com/science/article/pii/](http://www.sciencedirect.com/science/article/pii/S0006349514002276)
1089 [S0006349514002276](http://www.sciencedirect.com/science/article/pii/S0006349514002276), doi: <https://doi.org/10.1016/j.bpj.2014.02.021>.

1090 **Kapusta P**. Absolute Diffusion Coefficients:Compilation of Reference Data for FCS Calibration.
1091 PicoQuant GmbH; 2020.

1092 **Keminer O**, Peters R. Permeability of single nuclear pores. *Biophys J*. 1999; 77(1):217–228.

1093 **Ketterer P**, Ananth AN, Trip DSL, Mishra A, Bertosin E, Ganji M, van der Torre J, Onck P, Dietz H, Dekker
1094 C. DNA origami scaffold for studying intrinsically disordered proteins of the nuclear pore complex.

1095 Nature Communications. 2018 12; 9:902. <http://www.nature.com/articles/s41467-018-03313-w>, doi:
1096 10.1038/s41467-018-03313-w.

1097 **Keyser UF**, van der Does J, Dekker C, Dekker NH. Optical tweezers for force measurements on DNA
1098 in nanopores. Review of Scientific Instruments. 2006; 77(10):105105. [https://doi.org/10.1063/1.](https://doi.org/10.1063/1.2358705)
1099 [2358705](https://doi.org/10.1063/1.2358705), doi: 10.1063/1.2358705.

1100 **Kim SJ**, Fernandez-Martinez J, Nudelman I, Shi Y, Zhang W, Raveh B, Herricks T, Slaughter BD, Hogan
1101 JA, Upla P, Chemmama IE, Pellarin R, Echeverria I, Shivaraju M, Chaudhury AS, Wang J, Williams
1102 R, Unruh JR, Greenberg CH, Jacobs EY, et al. Integrative structure and functional anatomy of a
1103 nuclear pore complex. Nature. 2018 Mar; 555(7697):475–482. <https://doi.org/10.1038/nature26003>,
1104 doi: 10.1038/nature26003.

1105 **Klughammer N**, Code from Paper Palladium Zero-Mode Waveguides for Optical Single Molecule De-
1106 tection with Nanopores; 2020. [https://data.4tu.nl/articles/software/Code_from_Paper_Palladium_](https://data.4tu.nl/articles/software/Code_from_Paper_Palladium_Zero-Mode_Waveguides_for_Optical_Single_Molecule_Detection_with_Nanopores/12888551)
1107 [Zero-Mode_Waveguides_for_Optical_Single_Molecule_Detection_with_Nanopores/12888551](https://data.4tu.nl/articles/software/Code_from_Paper_Palladium_Zero-Mode_Waveguides_for_Optical_Single_Molecule_Detection_with_Nanopores/12888551), doi:
1108 10.4121/12888551.v1.

1109 **Klughammer N**, Barth A, Dekker M, Code for paper Diameter Dependence of Transport through
1110 Nuclear Pore Complex Mimics Studied Using Optical Nanopores. 4TU.ResearchData; 2023.
1111 https://data.4tu.nl/articles/software/_/21027850/0, doi: 10.4121/21027850.

1112 **Klughammer N**, Barth A, Dekker M, Data from paper Diameter Dependence of Transport through
1113 Nuclear Pore Complex Mimics Studied Using Optical Nanopores. 4TU.ResearchData; 2023.
1114 https://data.4tu.nl/articles/dataset/_/22059227/0, doi: 10.4121/22059227.

1115 **Klughammer N**, Dekker C. Palladium zero-mode waveguides for optical single-molecule detection
1116 with nanopores. Nanotechnology. 2021 feb; 32(18):18LT01. [https://doi.org/10.1088/1361-6528/](https://doi.org/10.1088/1361-6528/abd976)
1117 [abd976](https://doi.org/10.1088/1361-6528/abd976), doi: 10.1088/1361-6528/abd976.

1118 **Kowalczyk SW**, Kapinos L, Blosser TR, Magalhães T, van Nies P, Lim RYH, Dekker C. Single-molecule
1119 transport across an individual biomimetic nuclear pore complex. Nature Nanotechnology. 2011
1120 6; 6:433. <https://doi.org/10.1038/nnano.2011.88>.

1121 **Levene MJ**, Korch J, Turner SW, Foquet M, Craighead HG, Webb WW. Zero-mode waveguides
1122 for single-molecule analysis at high concentrations. science. 2003; 299(5607):682–686. doi:
1123 10.1126/science.1079700.

1124 **Lim RYH**, Huang B, Kapinos LE. How to operate a nuclear pore complex by Kap-centric
1125 control. Nucleus. 2015; 6(5):366–372. <https://doi.org/10.1080/19491034.2015.1090061>, doi:
1126 10.1080/19491034.2015.1090061, pMID: 26338152.

1127 **Love JC**, Wolfe DB, Haasch R, Chabinc ML, Paul KE, Whitesides GM, Nuzzo RG. Formation
1128 and Structure of Self-Assembled Monolayers of Alkanethiolates on Palladium. Journal of the
1129 American Chemical Society. 2003; 125(9):2597–2609. <https://doi.org/10.1021/ja028692+>, doi:
1130 10.1021/ja028692+, pMID: 12603148.

1131 **Majid A**, Bensebaa F, Ecuyer PL, Pleizier G, Deslandes Y. Modification of the metallic surface of
1132 silver by the formation of alkanethiol self-assembled monolayers with subsequent reaction with
1133 chlorosilanes. *Rev Adv Mater Sci*. 2003; 4:25–31.

1134 **Wes McKinney**. Data Structures for Statistical Computing in Python. In: Stéfan van der Walt,
1135 Jarrod Millman, editors. *Proceedings of the 9th Python in Science Conference*; 2010. p. 56 – 61.
1136 <https://doi.org/10.25080/Majora-92bf1922-00a>, doi: 10.25080/Majora-92bf1922-00a.

1137 **Mohr D**, Frey S, Fischer T, Güttler T, Görlich D. Characterisation of the passive permeability barrier
1138 of nuclear pore complexes. *The EMBO Journal*. 2009; 28(17):2541–2553. [https://www.embopress.](https://www.embopress.org/doi/abs/10.1038/emboj.2009.200)
1139 [org/doi/abs/10.1038/emboj.2009.200](https://doi.org/10.1038/emboj.2009.200), doi: <https://doi.org/10.1038/emboj.2009.200>.

1140 **Ng SC**, Biswas A, Huyton T, Schünemann J, Reber S, Görlich D. Barrier properties of Nup98 FG
1141 phases ruled by FG motif identity and inter-FG spacer length. *bioRxiv*. 2022; .

1142 **Ng SC**, Güttler T, Görlich D. Recapitulation of selective nuclear import and export with a perfectly
1143 repeated 12mer GLFG peptide. *Nature Communications*. 2021 Jun; 12(1):4047. [https://doi.org/10.](https://doi.org/10.1038/s41467-021-24292-5)
1144 [1038/s41467-021-24292-5](https://doi.org/10.1038/s41467-021-24292-5), doi: 10.1038/s41467-021-24292-5.

1145 **Novotny L**, Hecht B. Principles of Nano-Optics. Cambridge University Press; 2006. doi:
1146 10.1017/CBO9780511813535.

1147 **Palik ED**. Handbook of optical constants of solids, vol. 3. Academic press; 1998.

1148 **Perez F**, Granger BE. IPython: A System for Interactive Scientific Computing. *Computing in Science*
1149 *Engineering*. 2007; 9(3):21–29.

1150 **Plesa C**, Kowalczyk SW, Zinsmeister R, Grosberg AY, Rabin Y, Dekker C. Fast Translocation of
1151 Proteins through Solid State Nanopores. *Nano Letters*. 2013; 13(2):658–663. [https://doi.org/10.](https://doi.org/10.1021/nl3042678)
1152 [1021/nl3042678](https://doi.org/10.1021/nl3042678), doi: 10.1021/nl3042678, PMID: 23343345.

1153 **Prime KL**, Whitesides GM. Adsorption of proteins onto surfaces containing end-attached
1154 oligo(ethylene oxide): a model system using self-assembled monolayers. *Journal of the Amer-*
1155 *ican Chemical Society*. 1993; 115(23):10714–10721. <https://doi.org/10.1021/ja00076a032>, doi:
1156 10.1021/ja00076a032.

1157 **Reichelt R**, Holzenburg A, Buhle J E L, Jarnik M, Engel A, Aeby U. Correlation between struc-
1158 ture and mass distribution of the nuclear pore complex and of distinct pore complex com-
1159 ponents. *Journal of Cell Biology*. 1990 04; 110(4):883–894. <https://doi.org/10.1083/jcb.110.4.883>,
1160 doi: 10.1083/jcb.110.4.883.

1161 **Rout MP**, Aitchison JD, Magnasco MO, Chait BT. Virtual gating and nuclear transport: the hole
1162 picture. *Trends in Cell Biology*. 2003; 13(12):622 – 628. [http://www.sciencedirect.com/science/](http://www.sciencedirect.com/science/article/pii/S0962892403002496)
1163 [article/pii/S0962892403002496](http://www.sciencedirect.com/science/article/pii/S0962892403002496), doi: <https://doi.org/10.1016/j.tcb.2003.10.007>.

1164 **Sanabria H**, Rodnin D, Hemmen K, Peulen T, Felekyan S, Fleissner M, Dimura M, Koberling F,
1165 Kühnemuth R, Hubbell W, Gohlke H, Seidel C. Resolving dynamics and function of transient states
1166 in single enzyme molecules. *Nat Commun*. 2020; 11(1):1231.

1167 **Schleicher KD**, Dettmer SL, Kapinos LE, Pagliara S, Keyser UF, Jeney S, Lim RYH. Selective transport
1168 control on molecular velcro made from intrinsically disordered proteins. *Nature Nanotechnology*.
1169 2014 Jul; 9(7):525–530. <https://doi.org/10.1038/nnano.2014.103>, doi: 10.1038/nnano.2014.103.

1170 **Schmidt HB**, Görlich D. Transport Selectivity of Nuclear Pores, Phase Separation, and Membrane-
1171 less Organelles. *Trends in Biochemical Sciences*. 2016; 41(1):46–61. <https://www.sciencedirect.com/science/article/pii/S0968000415002091>, doi: <https://doi.org/10.1016/j.tibs.2015.11.001>, special
1172 Issue: 40 Years of TiBS.
1173

1174 **Schmidt HB**, Görlich D. Nup98 FG domains from diverse species spontaneously phase-separate
1175 into particles with nuclear pore-like permselectivity. *eLife*. 2015 jan; 4:e04251. <https://doi.org/10.7554/eLife.04251>, doi: 10.7554/eLife.04251.
1176

1177 **Schrimpf W**, Barth A, Hendrix J, Lamb DC. PAM: A Framework for Integrated Analysis of
1178 Imaging, Single-Molecule, and Ensemble Fluorescence Data. *Biophysical Journal*. 2018;
1179 114(7):1518–1528. <https://www.sciencedirect.com/science/article/pii/S0006349518302959>, doi:
1180 <https://doi.org/10.1016/j.bpj.2018.02.035>.

1181 **van der Spoel D**, Lindahl E, Hess B, Groenhof G, Mark AE, Berendsen HJC. GROMACS: Fast, flexible,
1182 and free. *J Comput Chem*. 2005; 26(16):1701–1718. doi: 10.1002/jcc.20291.

1183 **Stennett E**, Ciuba M, Lin S, Levitus M. Demystifying PIFE: The Photophysics Behind the
1184 Protein-Induced Fluorescence Enhancement Phenomenon in Cy3. *J Phys Chem Lett*. 2015;
1185 6(10):1819–1823.

1186 **Strawn LA**, Shen T, Shulga N, Goldfarb DS, Wentz SR. Minimal nuclear pore complexes define
1187 FG repeat domains essential for transport. *Nature Cell Biology*. 2004 Mar; 6(3):197–206. <https://doi.org/10.1038/ncb1097>, doi: 10.1038/ncb1097.
1188

1189 **van der Walt S**, Colbert SC, Varoquaux G. The NumPy Array: A Structure for Efficient Numerical
1190 Computation. *Computing in Science Engineering*. 2011; 13(2):22–30.

1191 **Virtanen P**, Gommers R, Oliphant TE, Haberland M, Reddy T, Cournapeau D, Burovski E, Peterson P,
1192 Weckesser W, Bright J, van der Walt SJ, Brett M, Wilson J, Jarrod Millman K, Mayorov N, Nelson ARJ,
1193 Jones E, Kern R, Larson E, Carey C, et al. SciPy 1.0: Fundamental Algorithms for Scientific Computing
1194 in Python. *Nature Methods*. 2020; 17:261–272. <https://doi.org/10.1038/s41592-019-0686-2>, doi:
1195 10.1038/s41592-019-0686-2.

1196 **Wagner R**, Kapinos L, Marshall N, Stewart M, Lim RH. Promiscuous Binding of Karyopherin β 1 Modu-
1197 lates FG Nucleoporin Barrier Function and Expedites NTF2 Transport Kinetics. *Biophysical Journal*.
1198 2015; 108(4):918–927. <https://www.sciencedirect.com/science/article/pii/S0006349514048206>, doi:
1199 <https://doi.org/10.1016/j.bpj.2014.12.041>.

1200 **Watkins LP**, Yang H. Detection of Intensity Change Points in Time-Resolved Single-Molecule
1201 Measurements. *The Journal of Physical Chemistry B*. 2005; 109(1):617–628. <https://doi.org/10.1021/jp0467548>, doi: 10.1021/jp0467548, PMID: 16851054.
1202

- 1203 **Winogradoff D**, Chou HY, Maffeo C, Aksimentiev A. Percolation transition prescribes protein size-
1204 specific barrier to passive transport through the nuclear pore complex. *Nature Communications*.
1205 2022 9; 13:5138. <https://www.nature.com/articles/s41467-022-32857-1>, doi: 10.1038/s41467-022-
1206 32857-1.
- 1207 **Yamada J**, Phillips JL, Patel S, Goldfien G, Calestagne-Morelli A, Huang H, Reza R, Acheson J, Krishnan
1208 VV, Newsam S, Gopinathan A, Lau EY, Colvin ME, Uversky VN, Rexach MF. A Bimodal Distribution
1209 of Two Distinct Categories of Intrinsically Disordered Structures with Separate Functions in FG
1210 Nucleoporins. *Molecular & Cellular Proteomics*. 2010; 9(10):2205–2224. <https://www.mcponline.org/content/9/10/2205>, doi: 10.1074/mcp.M000035-MCP201.
- 1212 **Zila V**, Margiotta E, Turoňová B, Müller TG, Zimmerli CE, Mattei S, Allegretti M, Börner K, Rada J,
1213 Müller B, Lusic M, Kräusslich HG, Beck M. Cone-shaped HIV-1 capsids are transported through
1214 intact nuclear pores. *Cell*. 2021; 184(4):1032–1046.e18. <https://www.sciencedirect.com/science/article/pii/S0092867421000684>, doi: <https://doi.org/10.1016/j.cell.2021.01.025>.
- 1216 **Zimmerli CE**, Allegretti M, Rantos V, Goetz SK, Obarska-Kosinska A, Zagoriy I, Halavatyi A, Hummer
1217 G, Mahamid J, Kosinski J, Beck M. Nuclear pores dilate and constrict in cellulo. *Science*. 2021;
1218 374(6573):eabd9776. <https://www.science.org/doi/abs/10.1126/science.abd9776>, doi: 10.1126/sci-
1219 ence.abd9776.

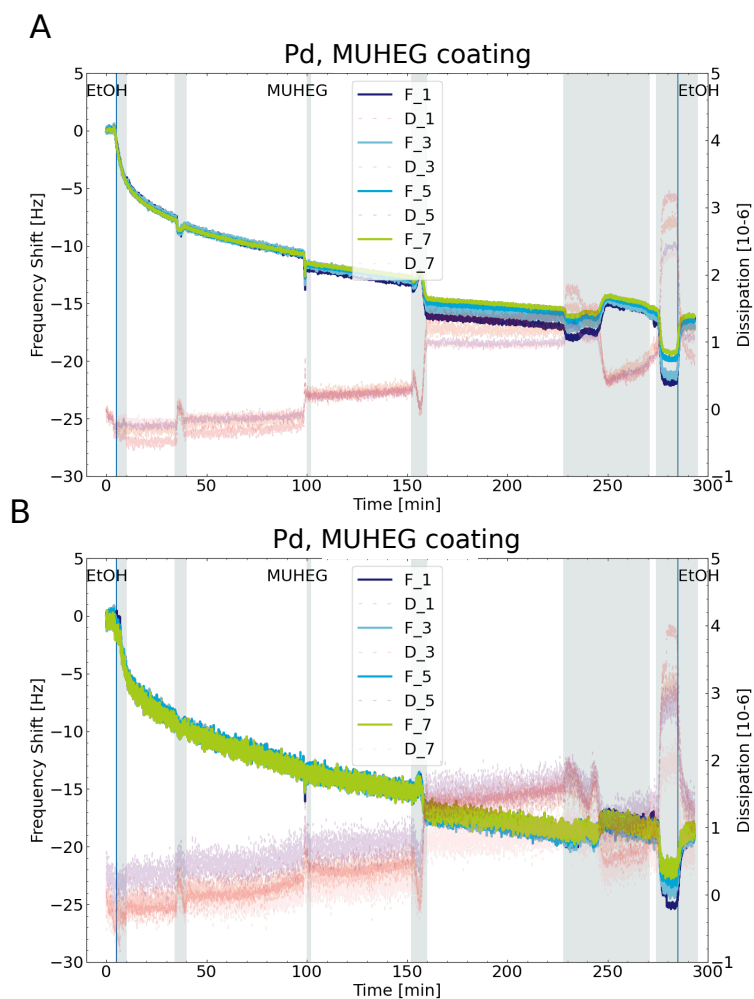
Appendix 1

Different cleaning methods tested

We encountered that after fabrication, the Pd surface inside the pores needed thorough cleaning to be accessible for thiol binding. During the study we tested cleaning with 100 W Oxygen plasma, 25 % and 5 % nitric acid, 1 h and 15 min RCA1, 15 min sulfuric acid piranha solution, 1 M potassium hydroxide solution, 10 min fuming sulfuric acid, 1 min 1 M sulfuric acid, 15 min hydrogen peroxide solution at 45 °C and 20 °C, 3 % and 37 % hydrochloric acid, 1 min gold etch (KI and I₂), 1:20 and 1:40 diluted commercial copper etch (Sigma Aldrich, comparable composition as commercial Pd etch), 30 % Ammonia, 2 min 1 M sodium hydroxide solution and boiling ethanol. Cleaning methods were evaluated based on two criteria. First, nanopores should remain intact, i.e, neither closed nor grew, and surfaces needed to be competent for thiol binding as monitored by QCM-D. Only hydrogen peroxide and ethanol boiling fulfilled both these conditions.

QCM-D experiments

In order to test how well MUHEG passivates a hydrogenperoxide-cleaned Pd surface, we coated two QCM-D chips with MUHEG and monitored their frequency and dissipation shifts. We found a resulting frequency shift of about 15 Hz when switching back to ethanol after incubating the chip with 250 µM of MUHEG in ethanol, indicating that mass had attached to the QCM-D chip and that the cleaning procedure thus allowed the thiols to bind to the surface (*Appendix 1—Figure 1*).



Appendix 1—figure 1. MUHEG grafting established on QCM-D. (A,B) The frequency (F1-F7) and dissipation (D1-D7) response of the different harmonics (numbers) for two QCM-D sensors versus time upon grafting of 250 μ M MUHEG in ethanol (see [Cleaning and surface grafting of Pd](#)). The blue vertical lines show when the solution was switched in the flow cell. The grey shaded regions show the time when the solution was flowed through the flow cell. Upon MUHEG binding a decreasing frequency can be observed, which shows that mass attaches to the sensor's surfaces.

Next, we switched the buffers to 150 mM of KCl in 1xTE and flushed 500 nM of BSA followed by TE buffer and 500 nM of Kap95. After switching back to TE buffer, we found a frequency shift of less than 5 Hz, which was much less than expected for untreated surfaces ([Appendix 1—Figure 2](#)). This result indicates that the surface had been passivated against proteins adhering to the surface. While this was a promising result, we knew from previous experiments that even if a surface is passivated well enough on QCM-D, we might still see considerable effects of protein sticking in translocation experiments. Thus we determined a real proof

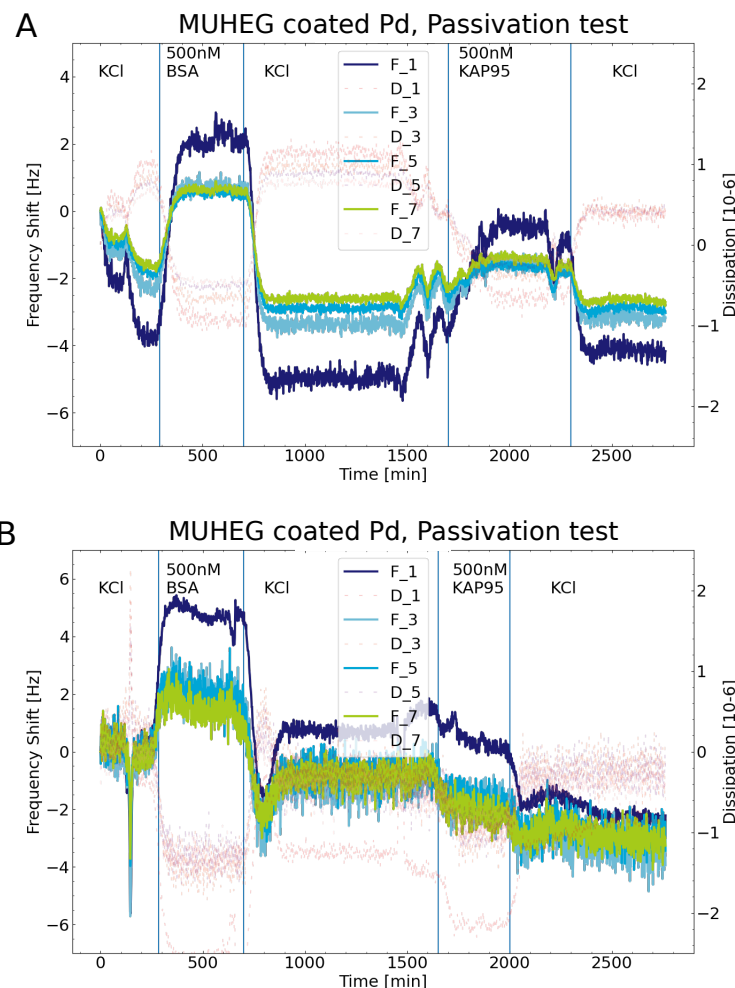
1256

1257

1258

1259

of good passivation to be a linear relationship of concentration versus event rate in open pore experiments.



1260

1261

1262

1263

1264

1265

1266

Appendix 1—figure 2. MUHEG passivation established on QCM-D. (A,B) Same chips and setup as in **Appendix 1—Figure 1** The frequency response of flushing 500 nM of BSA and 500 nM of Kap95 over the MUHEG passivated surface of the QCM-D chips only shows a minor frequency shift of less than 5 Hz (KCl level before and after flushing the proteins). This suggests that the Pd surface can be effectively passivated against adhering proteins by a MUHEG coating.

During our study, we noted that Pd nanopores could close upon incubation in PBS after peroxide cleaning. This effect was not observed for MUHEG coated pores that were incubated for extended time in ethanol after the peroxide cleaning. Thus we developed another cleaning strategy for Pd surfaces based on ethanol boiling, inspired from *Majid et al. (2003)*. In order to test the capability to bind Nsp1 after this treatment, we performed a QCM-D experiment. The cleaned chip was flushed

1272

1273

1274

1275

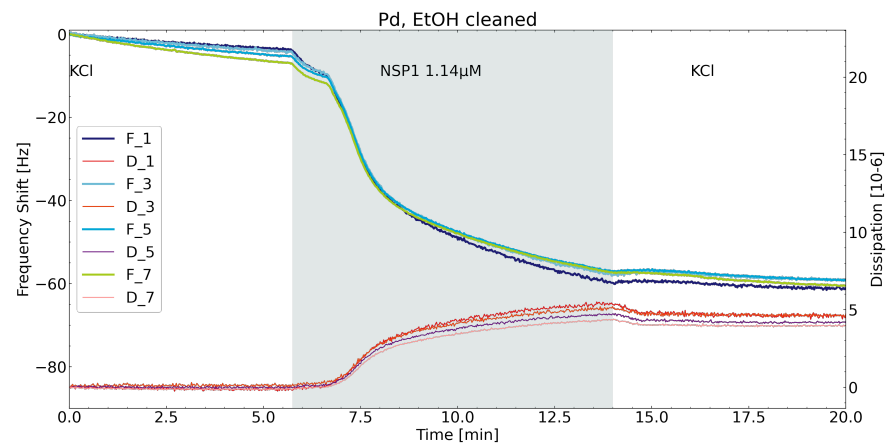
1276

1277

1278

1279

with 150 mM KCl + 1xTE buffer, then 1.14 μ M of Nsp1 and then TE buffer buffer again. The resulting frequency shift due to Nsp1 attachment was determined to be approximately 60 Hz (**Appendix 1—Figure 3**). This was comparable to previous experiments on piranha cleaned gold QCM-D chips. Since deducing a grafting density from QCM-D experiments was difficult, this serves more as a qualitative result and the actual test of sufficient grafting needed to be made in the nanopore.



1280

1281

1282

1283

1284

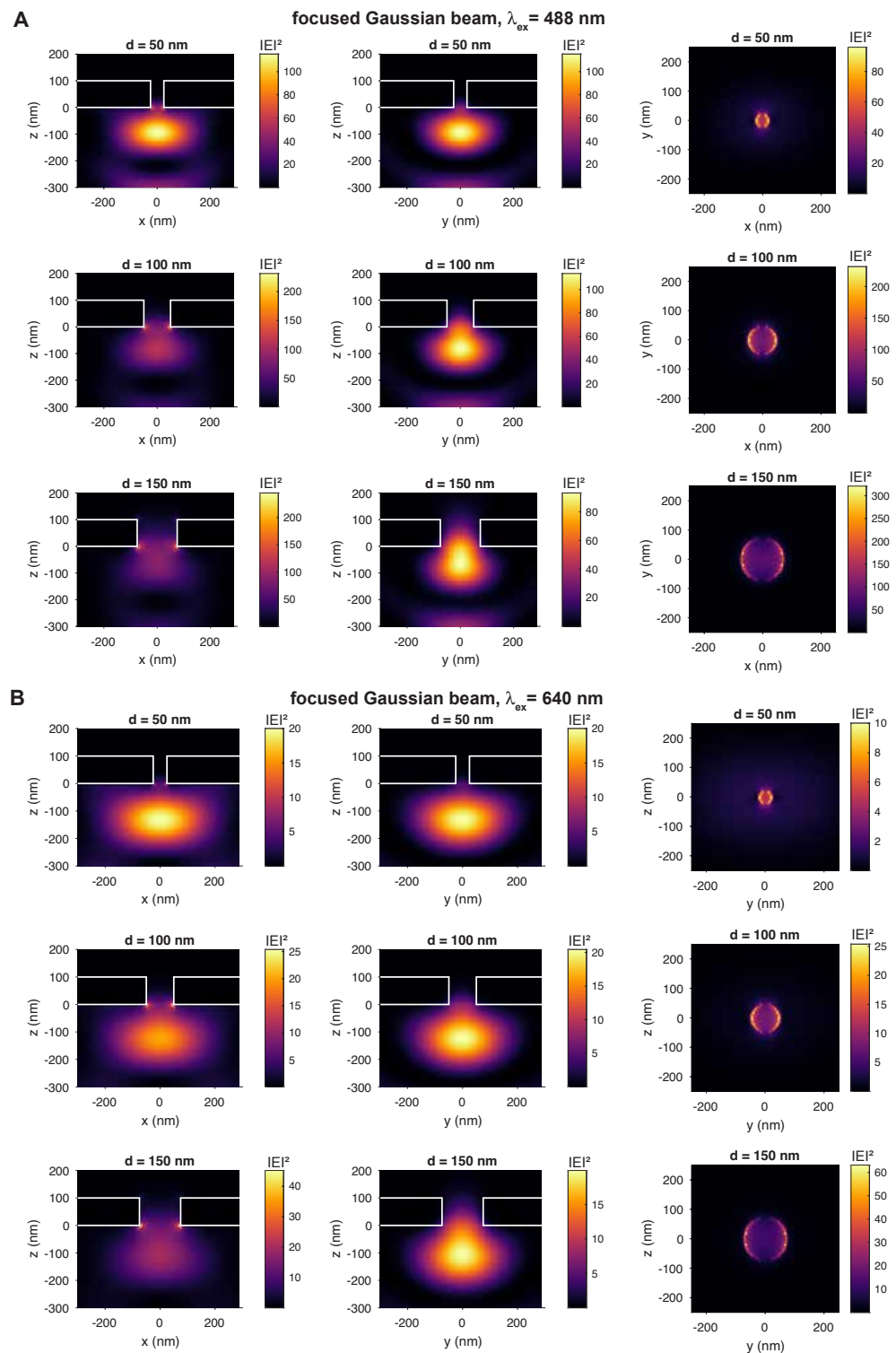
1285

1286

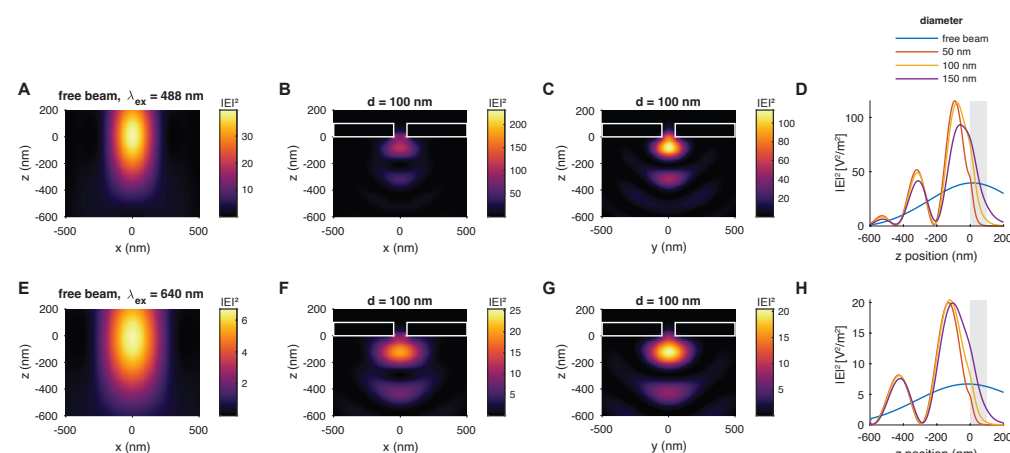
Appendix 1—figure 3. Nsp1 binding on QCM-D The frequency (F1-F7) and dissipation (D1-D7) response of the different harmonics (numbers) for a Pd coated QCM-D sensors versus time upon grafting of 1.14 μ M Nsp1 in PBS. The QCM-D chip was cleaned by boiling ethanol (see Cleaning and surface grafting of Pd). The frequency shift from before the Nsp1 coating to after was approximately 60 Hz which shows an acceptable coating efficiency. Nsp1 was flushed in the grey shaded area.

Appendix 2

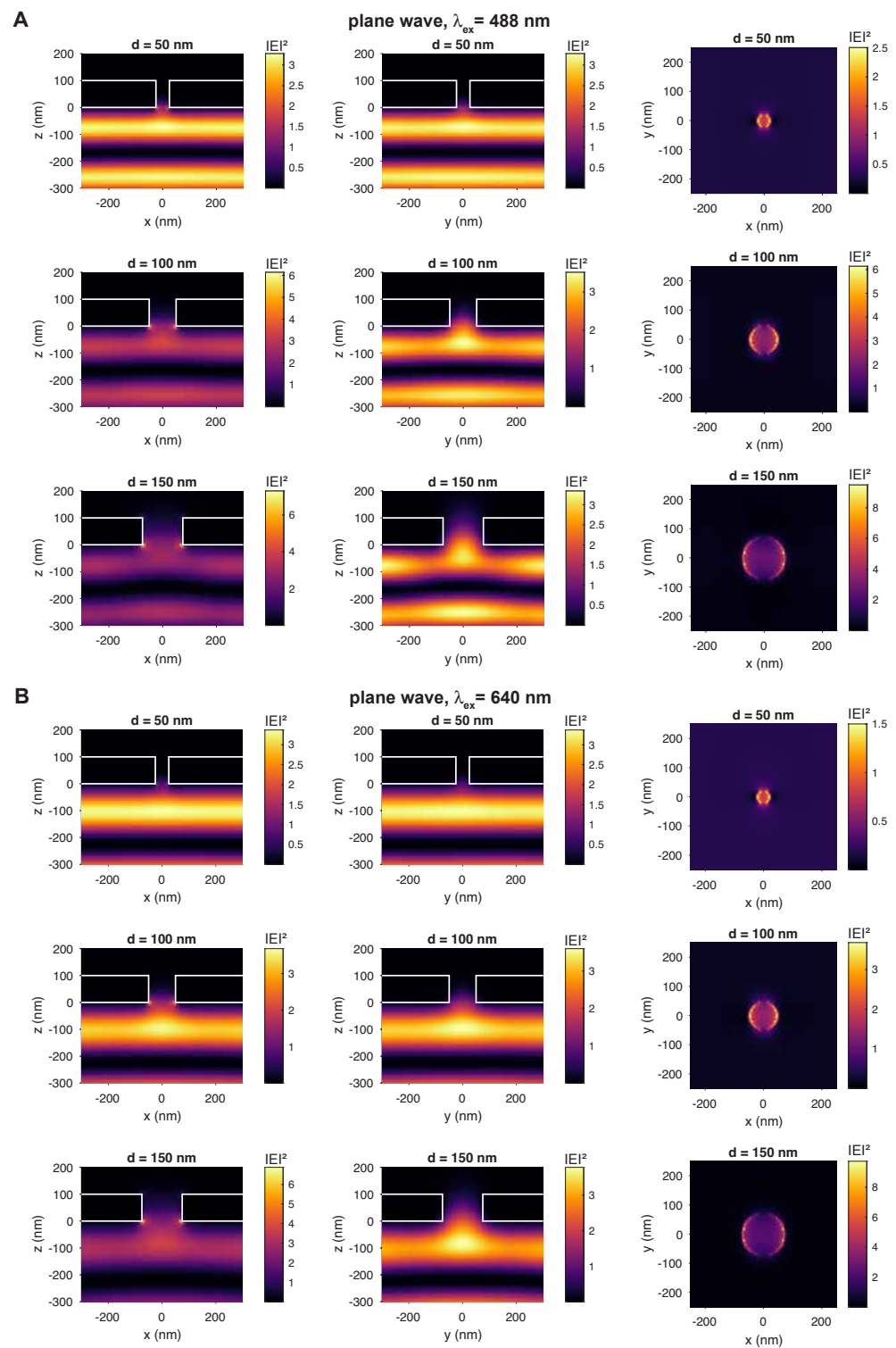
Finite-Difference Time Domain (FDTD) Simulations



Appendix 2—figure 1. Threedimensional finite-difference time-domain simulations of the electric field intensity distribution $|E|^2$ in units of V^2/m^2 in the proximity of the ZMW for excitation by a diffraction-limited focused Gaussian beam with wavelengths of 488 nm (A) and 640 nm (B). The lower side of the 100 nm thick palladium membrane is placed at $z = 0$ nm. The source is located at the bottom and the electric field is polarized in the x-direction. The electric field intensity distributions are shown for pores with a diameter of 50, 100, and 200 nm (from top to bottom) in the xz (left) and yz (middle) planes passing through the center of the pore, and the xy (right) plane at the entrance to the pore at $z = 0$ nm. See **Appendix 2—Figure 2** for a zoomed out representation of the intensity distribution.

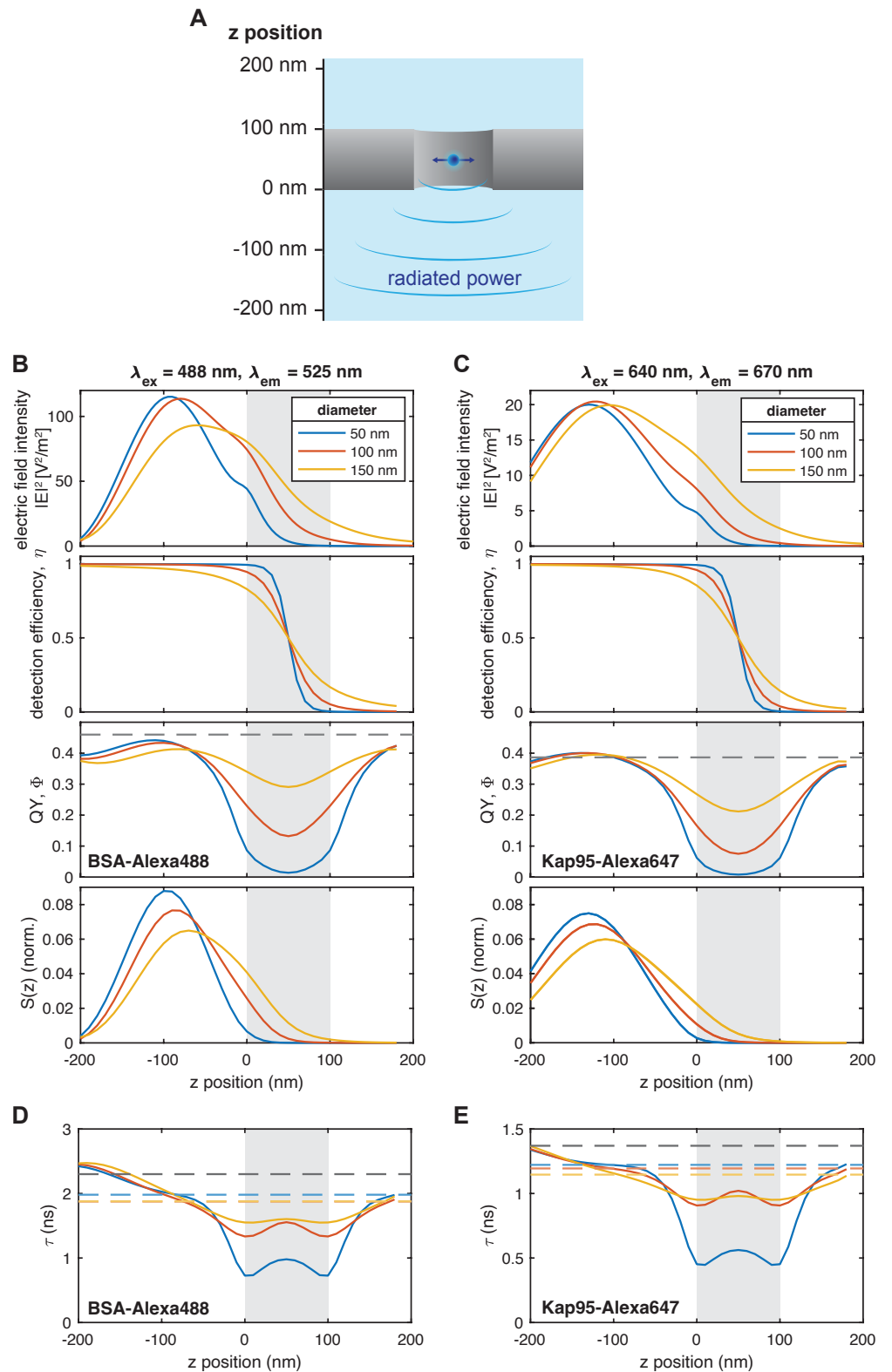


Appendix 2—figure 2. Threedimensional finite-difference time-domain simulations of the electric field intensity distribution of the excitation spot in the presence of a freestanding ZMW (compare **Appendix 2—Figure 1**), at excitation wavelengths of 488 nm (A-D) and 640 nm (E-H). Shown are the intensity distributions of the focused Gaussian beam in the absence (A,E) and presence (B-C,F-G) of the freestanding palladium ZMW. (D,H) The z-profiles of the intensity distribution along the center of the pore. The position of the palladium membrane is indicated as a gray shaded area.



1310

1311 **Appendix 2—figure 3.** Threedimensional finite-difference time-domain simulations of the
1312 electric field intensity distribution $|E|^2$ in units of V^2/m^2 in the proximity of the ZMW for
1313 excitation by a plane wave with wavelengths of 488 nm (A) and 640 nm (B). The lower side of
1314 the 100 nm thick palladium membrane is place at $z = 0$ nm. The source is located at the
1315 bottom and the electric field is polarized in the x-direction. The electric field intensity
1316 distributions are shown for pores with a diameter of 50, 100, and 200 nm (from top to
1317 bottom) in the xz (left) and yz (middle) planes passing through the center of the pore, and
1318 the xy (right) plane at the entrance to the pore at $z = 0$ nm.



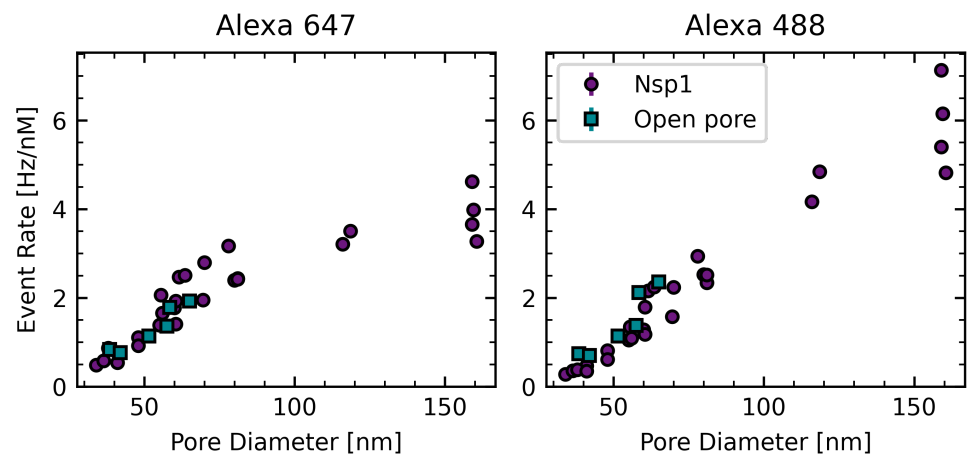
1320

Appendix 2—figure 4. Finite-difference time-domain simulations of the dipole emission in the proximity of the freestanding ZMW. (A) A scheme of the simulation setup. The dipole is placed in the center of the pore in the xy plane at varying z-positions. The detected signal is monitored on the detection (i.e., lower) side. (B-C) From top to bottom: The z-profiles of the excitation probability, the detection efficiency η , the emitter quantum yield Φ , and the total detected signal, along the center of the nanopore are shown for the blue (B, $\lambda_{ex}=488$ nm, $\lambda_{em}=525$ nm) and red (C, $\lambda_{ex}=640$ nm, $\lambda_{em}=670$ nm) channels. The total detected signal $S(z)$ is defined as the product of the excitation intensity, detection efficiency, and quantum yield. (D-E) Predicted fluorescence lifetimes τ of BSA-Alexa488 and Kap95-Alexa647. The position of the palladium membrane is indicated as a gray shaded area. The weighted averages of the fluorescence lifetime based on the detected signal $S(z)$ are shown as colored horizontal dashed lines. The gray dashed line indicates the measured fluorescence lifetime in the absence of the ZMW. The predicted lifetimes are 1.98, 1.88, and 1.88 ns for BSA-Alexa488, and 1.22, 1.95, and 1.15 ns for Kap95-Alexa647, for pore diameters of 50, 100, and 150 nm, respectively. The quantum yields and fluorescence lifetimes were estimated based on a literature values of $\Phi_0 = 0.8$ and $\tau_0 = 4.0$ ns for Alexa488 (*Sanabria et al., 2020*), and $\Phi_0 = 0.33$ and $\tau_0 = 1.17$ ns for Alexa647 (*Hellenkamp et al., 2018*), and measured lifetimes in the absence of the ZMW of 2.3 ns for BSA-Alexa488 and 1.37 for Kap95-Alexa647 (compare Appendix 7—*Figure 1*).

Appendix 3

Free Alexa fluorophore translocation

At the end of a full experiment with BSA and KAP95, mixtures of 50 nM or 100 nM Alexa 647 and Alexa 488 were flushed into the reservoir to detect clogged pores from the absence of events for the small fluorophores. As expected, small fluorophores were barely hindered in their diffusion from the Nsp1 molecules in the pore. Notably, this contrasts the findings of *Ananth et al. (2018)*, who reported only a residual conductance of (charged) ions through Nsp1-coated pores smaller than 40 nm, whereas we still found unhindered diffusion of free fluorescent dyes.



Appendix 3—figure 1. Free fluorophore translocations (A) Event rate versus pore diameter for Alexa 647. (B) Event rate versus pore diameter for Alexa 488. The event rate of both fluorophores does barely change between Nsp1-coated pores and open pores.

Influence of neighboring pores

In order to estimate an upper limit on the event rate that is found at a pore location due to analytes that diffused into the detection region from adjacent pores, we looked for an experiment where a closed pore was neighboured by two unblocked pores. In an open pore experiment, we encountered such a setting, where the closed pore was identified by its very low event rate. Specifically, in this case, pore 6 had a diameter of 56 nm, pore 7 was closed and pore 8 had a diameter of 70 nm. The respective BSA translocation rates at 250 nM were: 36 Hz, 0.8 Hz, 93 Hz. Assuming that all events found on pore 7 were due to diffusion from their neighboring pores, this gives that on any pore less than $2\% \approx \frac{0.8 \text{ Hz}}{36 \text{ Hz}}$ of the events

1363

1364

1365

1366

are not due to translocations through the pore itself but are due to diffusion from neighboring pores.

Appendix 4

Measurement scheme

The measurement scheme was the following:

- No Kap95
 - Measure PBS as a background reference
 - pre-incubate with 500 nM of BSA, wash it out with 250 nM of BSA
 - measure 250 nM of BSA
 - measure 500 nM of BSA
- Wash
 - wash with PBS
 - wash with 5 % Hexane-1-6-diol
 - wash with PBS
- 100 nM Kap95
 - measure 100 nM of Kap95
 - measure 100 nM of Kap95 and 250 nM of BSA
 - measure 100 nM of Kap95 and 500 nM of BSA
- Wash
 - wash with PBS
 - wash with 5 % Hexane-1-6-diol
 - wash with PBS
- For some experiments an additional 200 nM of Kap95 measurement was performed at this point.
- 1000 nM Kap95
 - measure 1000 nM of Kap95
 - measure 1000 nM of Kap95 and 250 nM of BSA
 - measure 1000 nM of Kap95 and 500 nM of BSA
- Wash with PBS
- Measure 50 nM of Alexa 488 and 50 nM of Alexa 647 in PBS.

Changing the analyte in the reservoir was done by replacing the volume at least three times. After changing the contents of the reservoir, a new transmission light

1395

1396

1397

1398

1399

1400

scan of all pores was performed to obtain the accurate locations. Subsequently each pore was measured one after another.

Hexane-1-6-diol (Sigma-Aldrich) was diluted to 5 % in 150 mM KCl with 1xTE buffer.

Appendix 5

Detailed diffusion model

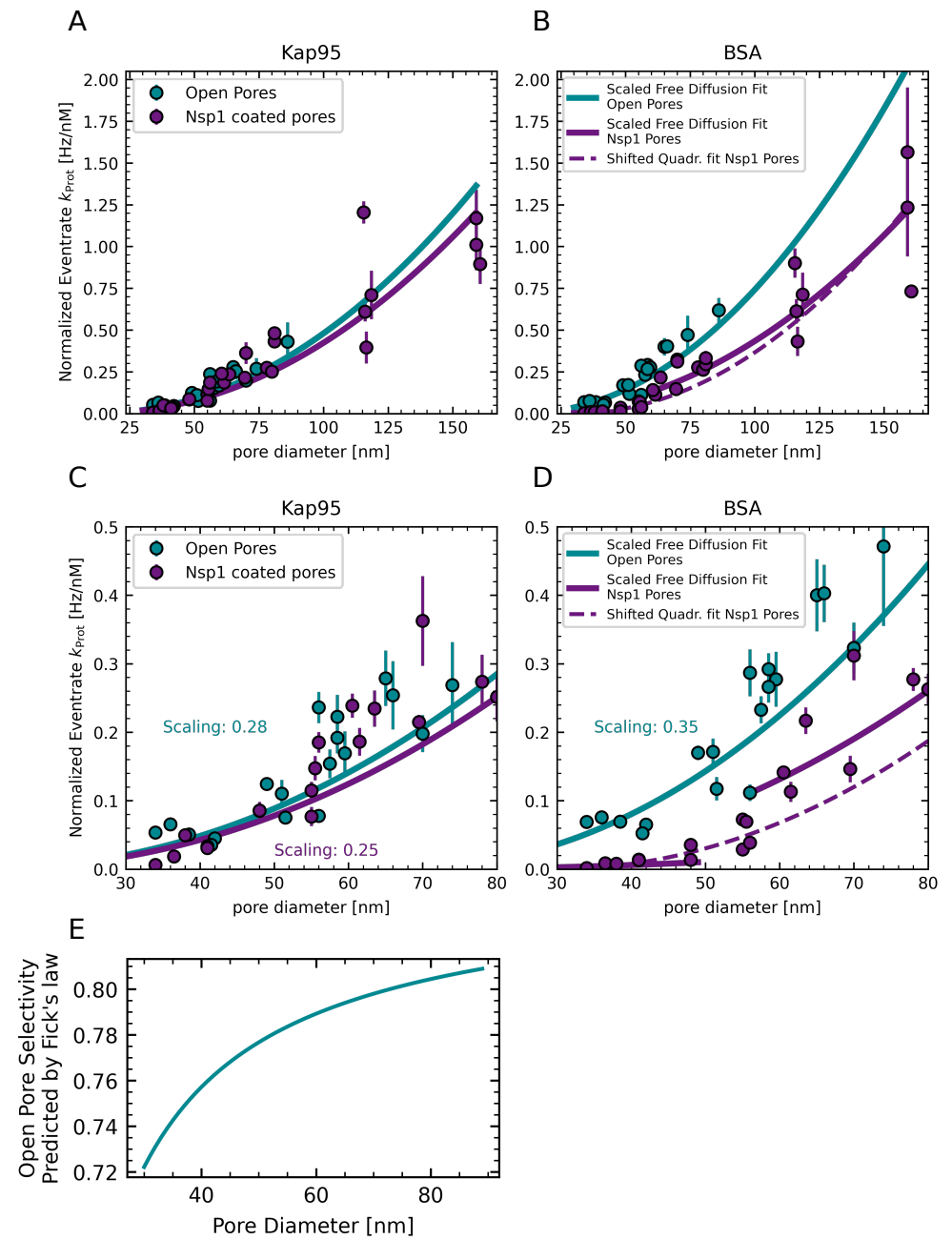
We explored how well the translocation rates can be accurately described by a diffusion model. In theory, the event rates should follow a diffusion model based on Fick's law. For reference, such a model was fit to the individual data points underlying the averages shown in **Figure 4** A-D based on Fick's law of diffusion:

$$k_{\text{Prot}} = \alpha \pi r^2 D_p(r) \frac{\Delta c}{L}, \quad (13)$$

where k_{Prot} is the translocation rate, r the pore radius, Δc the concentration difference between cis and trans, and L the length of the pore. The scaling factor α accounts for deviation from the ideal behavior due to protein pore interactions and events missed by the detection algorithm. $D_p(r)$ is the reduced diffusion coefficient due to confinement in the pore and is calculated as given by **Dechadilok and Deen (2006)**:

$$\begin{aligned} \frac{D_p(r)}{D} = & 1 + \frac{9}{8} \left(\frac{R_g}{r} \right) \ln \left(\frac{R_g}{r} \right) - 1.56034 \left(\frac{R_g}{r} \right) + 0.528155 \left(\frac{R_g}{r} \right)^2 + 1.91521 \left(\frac{R_g}{r} \right)^3 \\ & - 2.81903 \left(\frac{R_g}{r} \right)^4 + 0.270788 \left(\frac{R_g}{r} \right)^5 + 1.10115 \left(\frac{R_g}{r} \right)^6 - 0.435933 \left(\frac{R_g}{r} \right)^7, \end{aligned} \quad (14)$$

where R_g the radius of gyration of the protein ($R_g = 3.15$ nm for Kap95 and $R_g = 2.68$ nm for BSA as determined from their crystal structures) and D is the diffusion coefficient which was obtained from FCS measurements as $D = 46 \mu\text{m}^2/\text{s}$ for Kap95 and $D = 54 \mu\text{m}^2/\text{s}$ for BSA at 21 °C. As an alternative analysis, this model was fitted using the least-squares method to the individual data points underlying the averages from **Figure 4** in the main text, as shown in **Appendix 6—Figure 1**. The open pore data as well as the Nsp1-pore data for Kap95 can be well fitted by the diffusion model. The BSA-rates through Nsp1 pores, however, can not be described with a single diffusion model. Inspired by the opening of the Nsp1 mesh seen in the CGMD simulations, we introduced a threshold, where the translocation rates would follow a different diffusion regime. We note however, that in this transition region between 48 nm and 55 nm the data is better described by the shifted quadratic function.



Appendix 5—figure 1. (A,B) Normalized and averaged event rate vs. pore diameter as in Figure 4. Solid lines are fits of a diffusion model as described in this section. A single fit for BSA through Nsp1 would deviate both for small and large pore diameters. Therefore the dataset was split into two regimes: Below 50 nm and above 60 nm in order to fit the data. This threshold was inspired by the results of the CGMD simulations. The dashed line shows a fit of the shifted quadratic function to the BSA data through Nsp1 pores as described in the main text. (C,D) Zoom ins of (A,B). E: Selectivity of open pores, predicted by the diffusion model. The value is pore size dependent because of the different sizes of Kap95 and BSA.

Appendix 6

Fitting of translocation rates

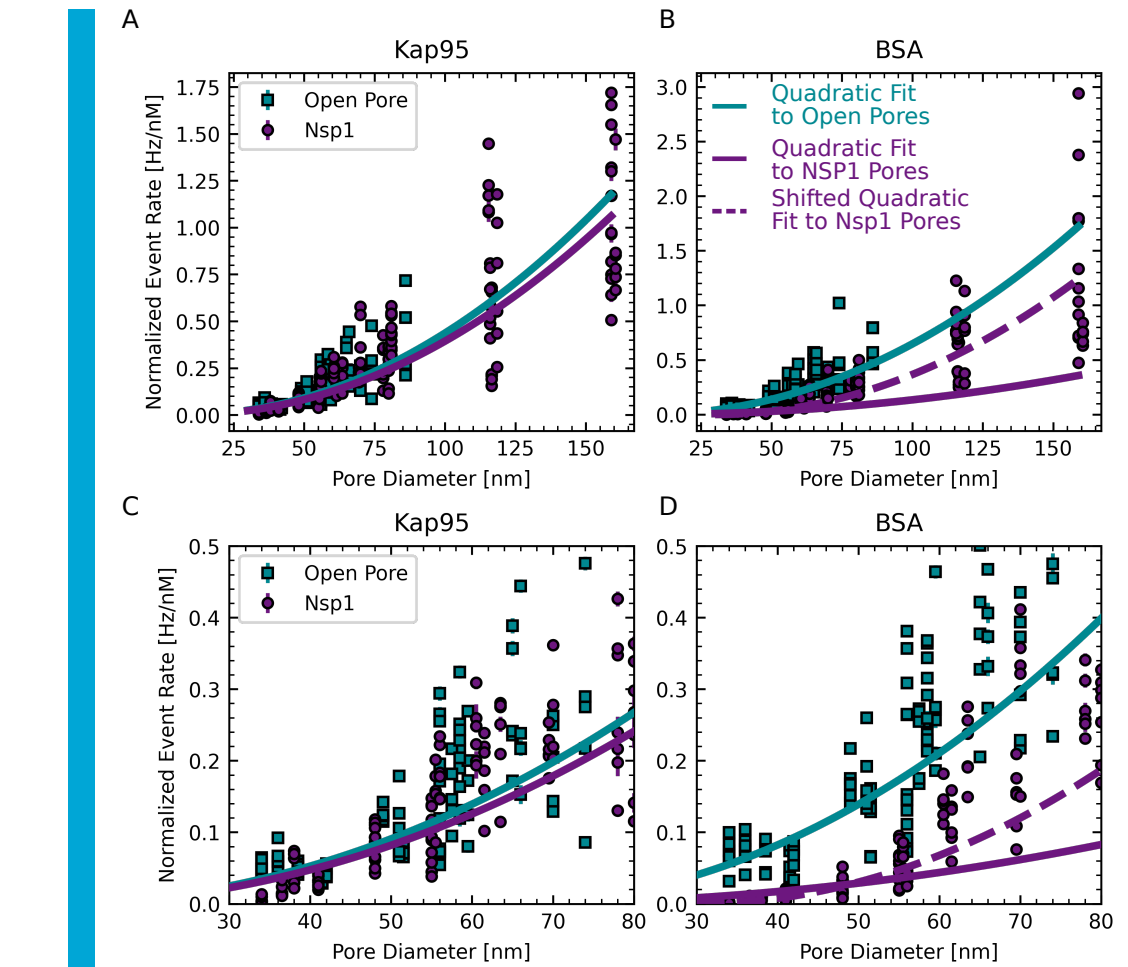
For congruence with the computational data, we fit a simplified diffusion model to the individual data points underlying the averages presented in **Figure 4** using a quadratic function:

$$k_{\text{Prot}} = \alpha (r - r_{\text{Prot}})^2, \quad (15)$$

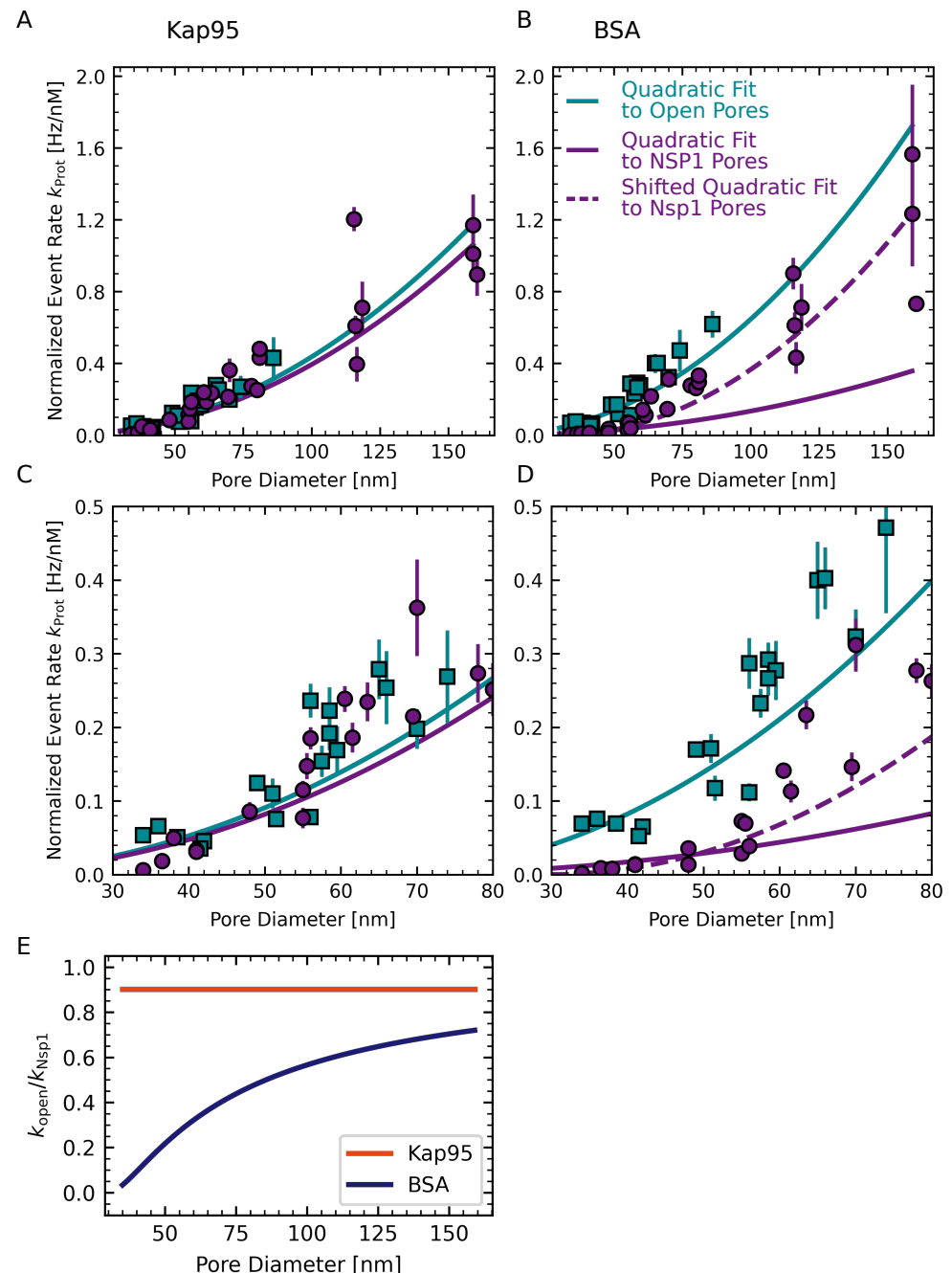
where k_{Prot} is the concentration-normalized translocation rate, r is the pore radius, r_{Prot} the protein's equivalent radius as proposed by **Winogradoff et al. (2022)** (see **Appendix 10** for details), and α a multiplicative scaling factor incorporating all factors such as concentration gradient, pore length, etc. All fits were performed using a least squares fitting, taking a statistical error on the individual event rates into account. This error was estimated from Poisson statistics, where the number N of events within a timetrace leads to $\Delta N = \sqrt{N}$. α was fitted individually on the event rates of Kap95 through open and Nsp1-coated pores. Additionally, the BSA event rates through open pores were fitted separately. The parameter α resulting from the BSA translocations for open pores, was used as a fixed parameter when fitting the BSA event rates through Nsp1-coated pores with a shifted and reduced quadratic function:

$$k_{\text{Prot}} = \alpha (r - r_{\text{Prot}} - b)^2, \quad (16)$$

where b is a shift parameter introduced to take into account a further reduction of the BSA event rate at small pore diameters.



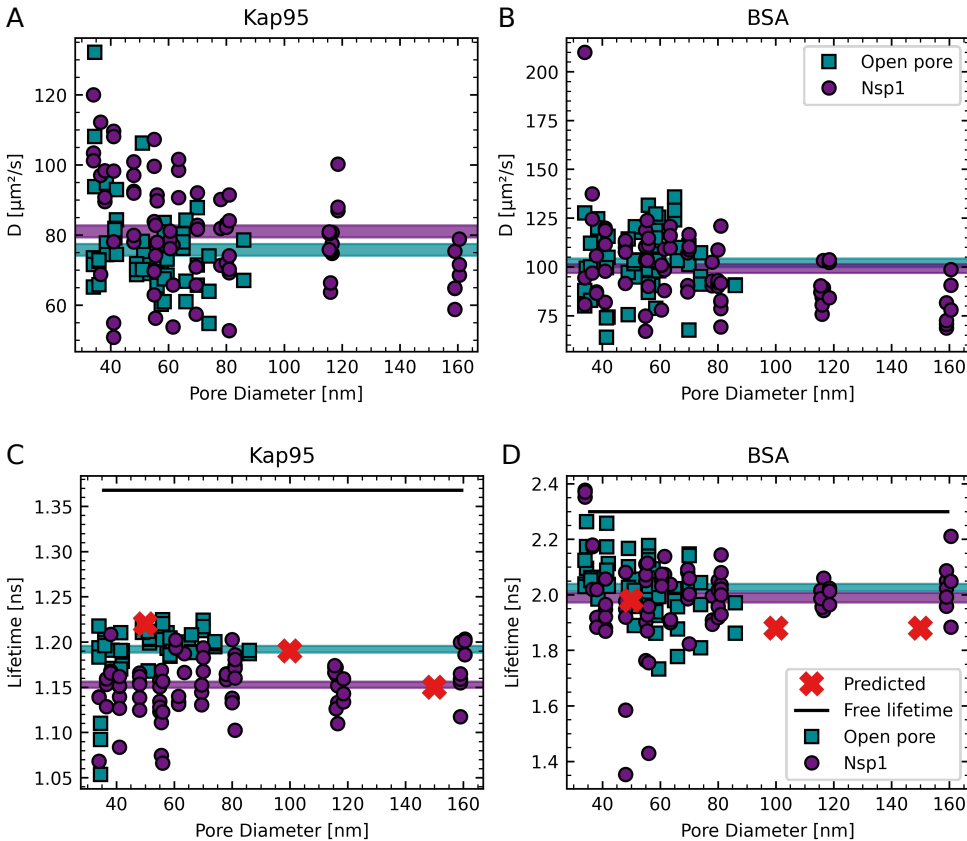
Appendix 6—figure 1. (A,B) Normalized event rate vs. pore diameter of the individual conditions underlying the points shown in *Figure 4*. Solid lines are fits of a quadratic function as given in *Equation 15*. The BSA event rates through Nsp1-coated pores were not well described by the quadratic function. Therefore, a shift parameter was introduced as given in eq. *Equation 16* (dashed line). (C,D) Zoom ins of (A,B).



Appendix 6—figure 2. (A,B) Normalized and averaged event rate vs. pore diameter as in **Figure 4**. Solid lines are fits of a quadratic function as given in **Equation 15**. The fit for BSA through Nsp1 deviates both for small and large pore diameters. Therefore a shift parameter was introduced as given in **Equation 16** to fit the data (dashed line). (C,D) Zoom ins of (A,B). (E) Open pore event rates obtained from the quadratic fit divided by Nsp1 pore event rates obtained from the quadratic fit vs. pore diameter. While there is barely any decrease of the event rate for Kap95 when Nsp1 is present, BSA experiences an approximately 10-fold decrease for small pores of 35 nm diameter. This ratio increases with pore diameter and approaches a value of 1 in the limit to very large pores.

1485 **Appendix 7**

1486 **Diffusion coefficients and fluorescence lifetimes**



Appendix 7—figure 1. (A,B) Plots of the diffusion coefficient vs. pore diameter for Kap95 and BSA, respectively. The diffusion coefficient is estimated by FCS analysis of the time traces obtained in the nanopore experiments at the highest protein concentration. The horizontal lines indicates the average diffusion coefficient and the width corresponds to twice the standard error of the mean. The average diffusion coefficient of both Kap95 and BSA shows no significant difference between open pores and Nsp1-coated pores. This indicates that interactions of the proteins with the Nsp1 mesh do not obstruct the diffusion. Alternatively, it is possible that the bound fraction is not detected in our experiments if it is close to the metal surface due to metal-induced quenching of the fluorescence signal. (C,D) Plots of the fluorescence lifetime vs. pore diameter for Kap95 and BSA, respectively. The fluorescence lifetime is calculated based on the individual time traces of the highest protein concentration. The mean (horizontal lines) with twice the standard error of the mean (width of the lines) gives an estimate of the spread. For both Kap95 and BSA, the average fluorescence lifetime is significantly lower than what is measured in open solution (black lines). This can be attributed to the influence of the nearby metal nanostructure on the radiative and non-radiative rates. The predicted lifetimes based on FDTD simulations are shown as red crosses (compare **Appendix 2—Figure 4**). Whereas for BSA the lifetime in Nsp1-coated pores and open pores does not differ significantly, there is a significant decrease of the fluorescence lifetime of Kap95 in Nsp1-coated pores compared to open pores. This suggests that Kap95 remains within the proximity of the pore for a longer time when Nsp1 is present.

Our measurements provide additional information on the diffusivity of the proteins and the fluorescence lifetime of the fluorophores (**Appendix 7—Figure 1**). From this, we can gain additional insight on the interaction of the proteins with the Nsp1 mesh within the pore. Interestingly, we do not observe a significant hindrance of the diffusivity for either BSA or Kap95, despite the known interaction of Kap95 with the FG repeats of the Nsp1 mesh. This indicates that the dynamic and multivalent interactions do not markedly slow down the diffusion of Kap95. Alternatively, it is possible that the fluorescence signal of the interacting species is quenched due to the close proximity to the metal surface due to metal-induced electron transfer (*Gregor et al., 2019*). This would render it impossible to detect the interactions because the detected signal would originate predominantly from freely diffusing molecules that have left the Nsp1 mesh.

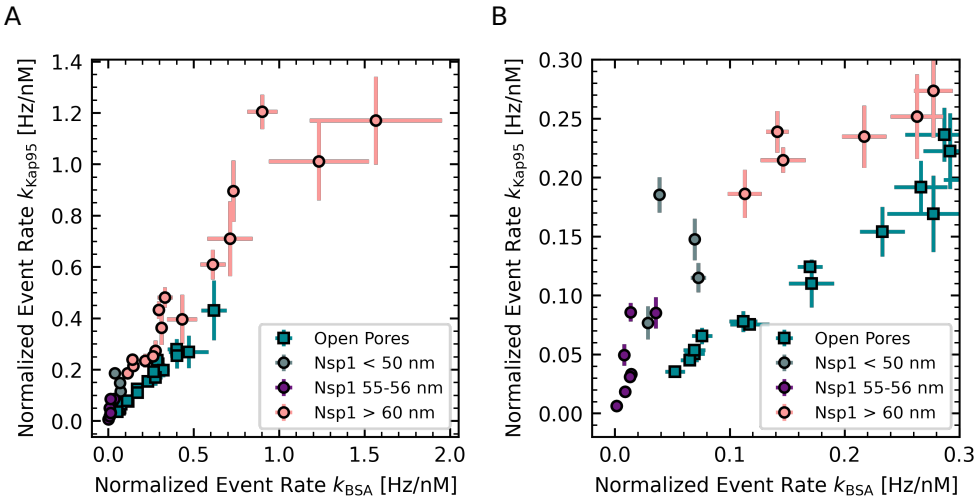
Additional information on the photophysics is obtained from the fluorescence lifetime. We find a significant decrease of the fluorescence lifetime in the presence of the metal nanostructure (compared to open focus measurements) both for the dyes Alexa488 on BSA and Alexa647 on Kap95. Note that this lifetime reduction can

1524
1525
1526
1527
1528
1529
1530
1531
1532
1533
1534
1535
1536
1537
1538
1539

originate both from metal-induced quenching (*Gregor et al., 2019*) or a radiative rate enhancement within the zero-mode waveguide (*Levene et al., 2003*). FDTD simulations of the dipole emission confirm that the fluorescence lifetime is shortened in the proximity of the metal nanostructure (*Appendix 2—Figure 4 D-E*) and provide good qualitative agreement with the measured fluorescence lifetimes of translocating molecules (see red crosses in *Appendix 7—Figure 1 C-D*).

Whereas for BSA there was no difference between the fluorescence lifetimes obtained for Nsp1-coated pores and open pores, we found a small but significant reduction of the fluorescence lifetime for Kap95 for Nsp1-coated pores. This indicates that, in the presence of Nsp1, Kap95 molecules either take a different path through the pore or spend more time in proximity of the metal nanoaperture. Intriguingly, it has recently been reported that Kap95 predominantly translocates along the periphery of the NPC (*Chowdhury et al., 2022*), which falls in line with our observation of a stronger coupling to the metal nanoaperture.

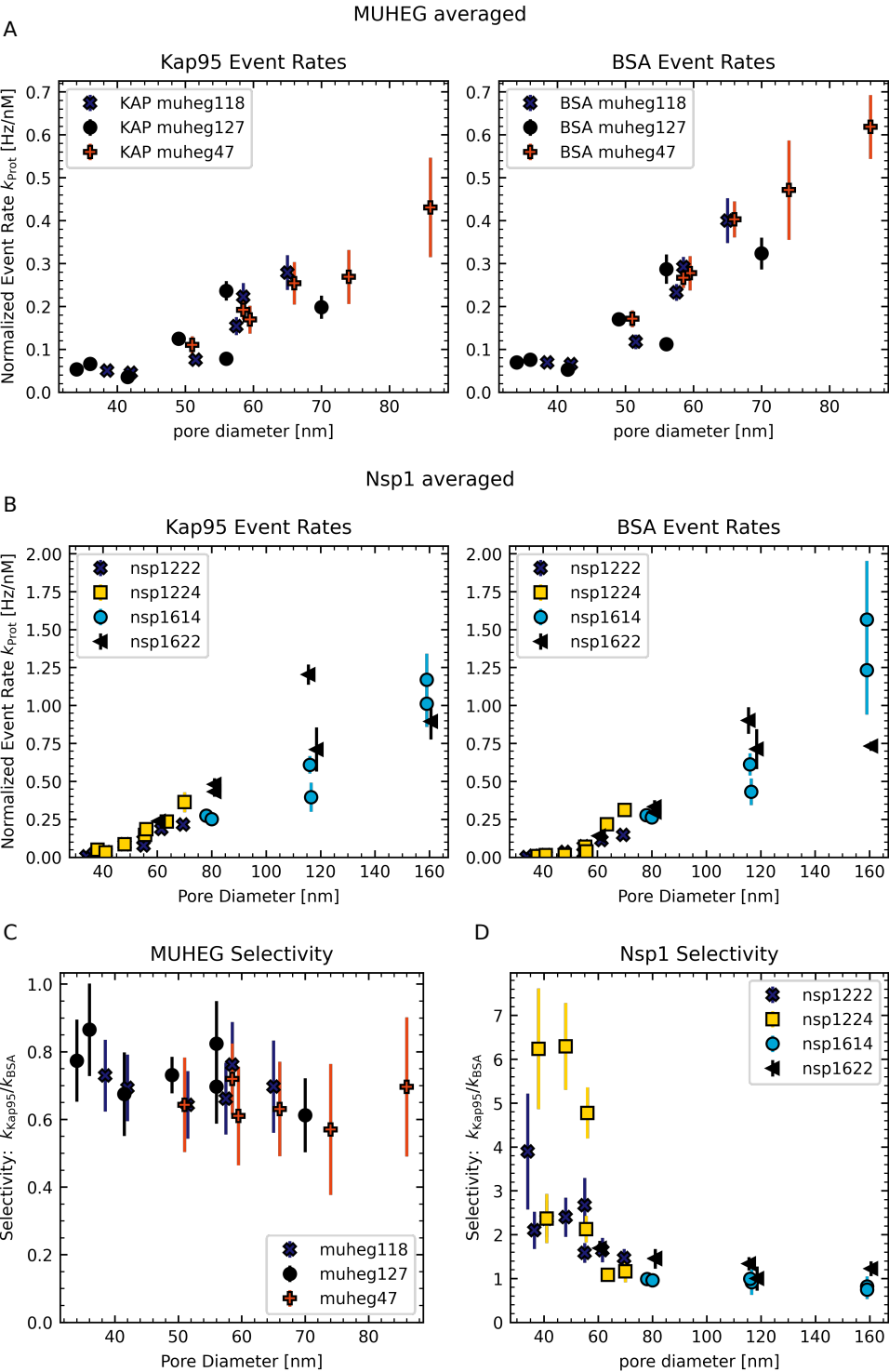
1540 **Appendix 8**



Appendix 8—figure 1. Correlation between event rates for Kap95 and BSA. (A) Normalized event rates of Kap95 vs. BSA for small (purple) and large (pink) Nsp1-coated pores and open pores (cyan). The event rates show a high degree of correlation with correlation coefficients of 0.72, 0.93, and 0.98 respectively. Additionally pores with diameters of 55 nm to 56 nm are shown in grey. (B) zoom in of (A).

1548

Appendix 9



1549

1550 **Appendix 9—figure 1.** (A, B) Normalized event rates for different open pore and Nsp1 pore
1551 experiments, respectively. The different data sets were highlighted according to their
1552 experimental day. A label for each experimental realisation is given in the legend. We don't
1553 observe any striking day-to-day variation. (C,D) Selectivity for different open pore and Nsp1
1554 pore experiments. Also in the selectivity we don't observe a striking difference between
1556 experimental repetitions.

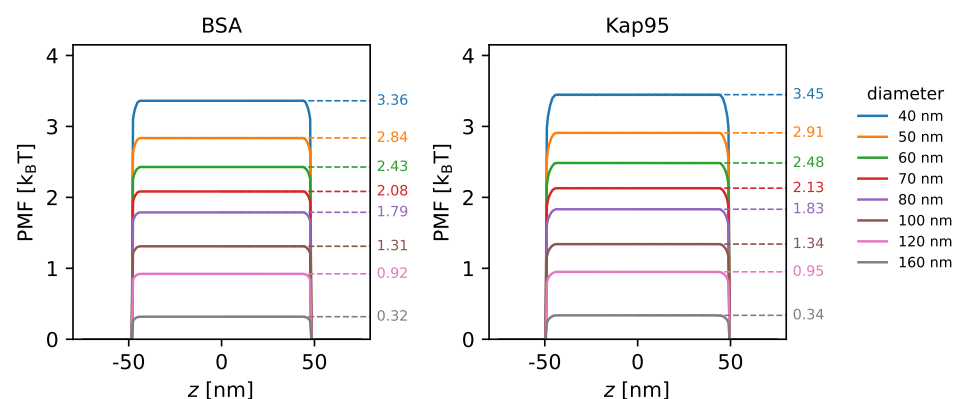
Appendix 10

Probe radius of BSA and Kap95

To determine the radius of a protein (used in the void analysis and for fitting the event rates), we used the procedure as described in (Winogradoff *et al.*, 2022). We started by computing the protein's moments of inertia, I_X , I_Y and I_Z , from the all-atom crystal structure. We then matched the moments of inertia of the protein with those of a constant density ellipsoid using $I_X = \frac{1}{5}m(b^2 + c^2)$, $I_Y = \frac{1}{5}m(a^2 + c^2)$ and $I_Z = \frac{1}{5}m(a^2 + b^2)$, where m is the total mass of the protein and a , b and c are the respective lengths of the three principal axes of the ellipsoid. To obtain the protein radius, we equated the volume of a sphere to the volume of the ellipsoid, i.e., $r_p = (abc)^{1/3}$. Using this method we find a probe radius of $r_p = 34 \text{ \AA}$ for BSA (PDB ID: 4F5S) and $r_p = 40 \text{ \AA}$ for Kap95 (PDB ID: 3ND2).

Fitting calculated event rates for open pores

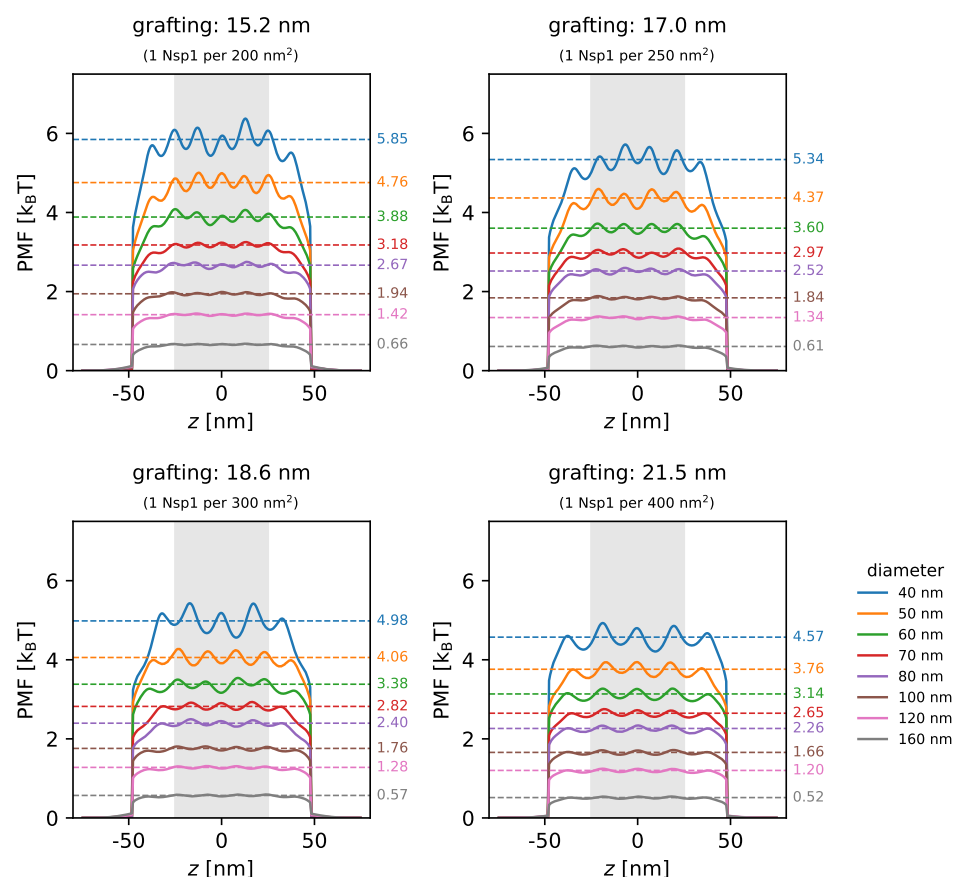
To obtain the scaling constant, k_0 , of the Arrhenius relation, we fitted the calculated event rates for open pores, obtained from the PMF barriers using the Arrhenius relation, to the (concentration-normalized) experimental open pore event rates (see Appendix 6 for fitting procedure). We note that the calculated event rates for open pores follow Equation 2 exactly. We therefore scaled the calculated event rates such that they align with the fits in Figure 4 A,B (cyan lines) and used the same constant $k_{0,BSA}$ to the Arrhenius relation for Nsp1-coated pores.



Appendix 10—figure 1. Potentials of mean force along the pore axis of open pores with various diameters derived from void analysis using a probe radius of r_{probe} of 34 \AA for BSA and 40 \AA for Kap95. The numbers next to the dashed lines indicate the permeability barriers ΔE .

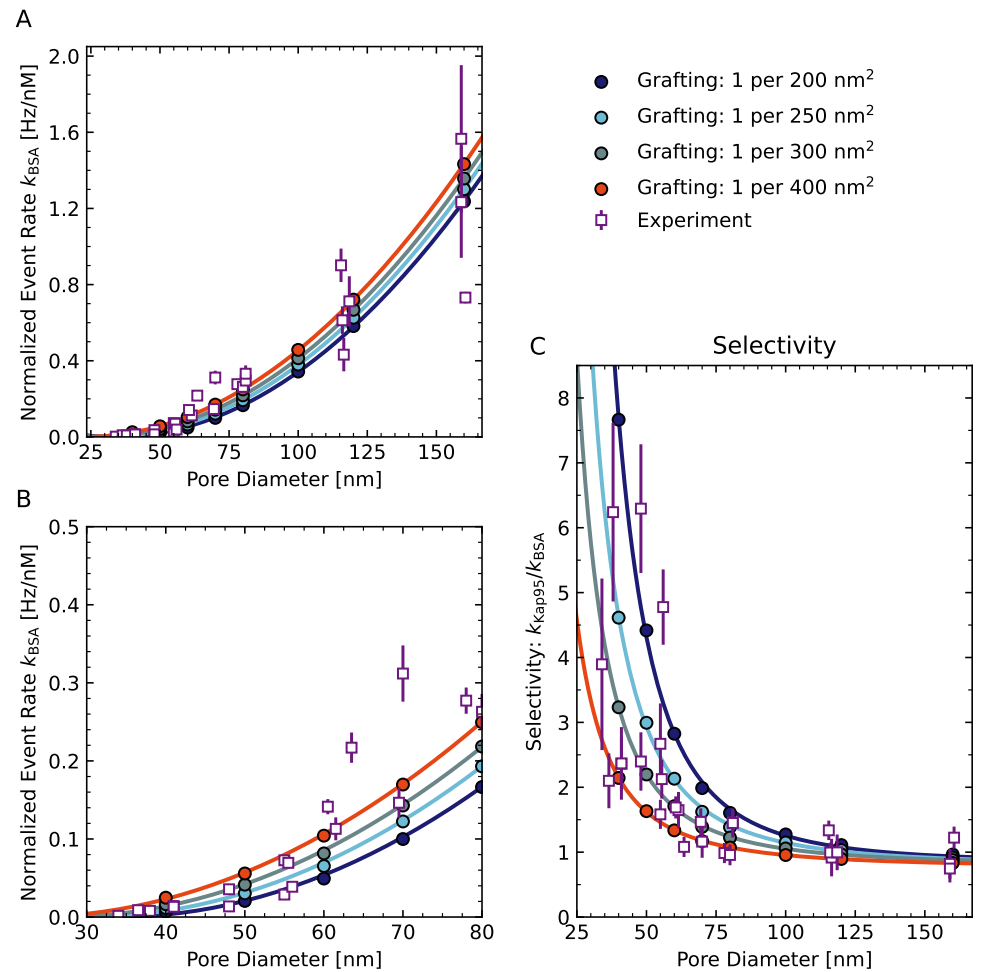
Potential of mean force for Nsp1-coated pores

The Nsp1 proteins in our simulations were anchored to the surface in a triangular fashion to achieve a homogeneous grafting density across the entire scaffold. We note that the location of the peaks in the PMF curves align with the z -coordinates of the Nsp1 anchor sites. Although the anchor sites clearly contribute to the translocation barrier, it would not be correct to use the maximum PMF as the energy barrier for translocation, as the idealized anchoring of Nsp1 on the scaffold is not a good approximation of the experiments (where Nsp1 is not anchored at discrete z -positions). Instead, to obtain a correct estimate of the energy barrier, ΔE , we used the average PMF for $-25 \text{ nm} \leq z \leq 25 \text{ nm}$.



Appendix 10—figure 2. Potentials of mean force along the pore axis of Nsp1-coated pores with various diameters and grafting densities using a probe radius of $r_{\text{probe}} = 34 \text{ Å}$ (BSA) derived from void analysis. The height of the PMF barrier, ΔE given on the right of the plots, is obtained by averaging the PMF between $-25 \text{ nm} \leq z \leq 25 \text{ nm}$ (gray region). The location of the peaks in the PMF curves are at the same z -coordinates as the anchoring points of the Nsp1 proteins.

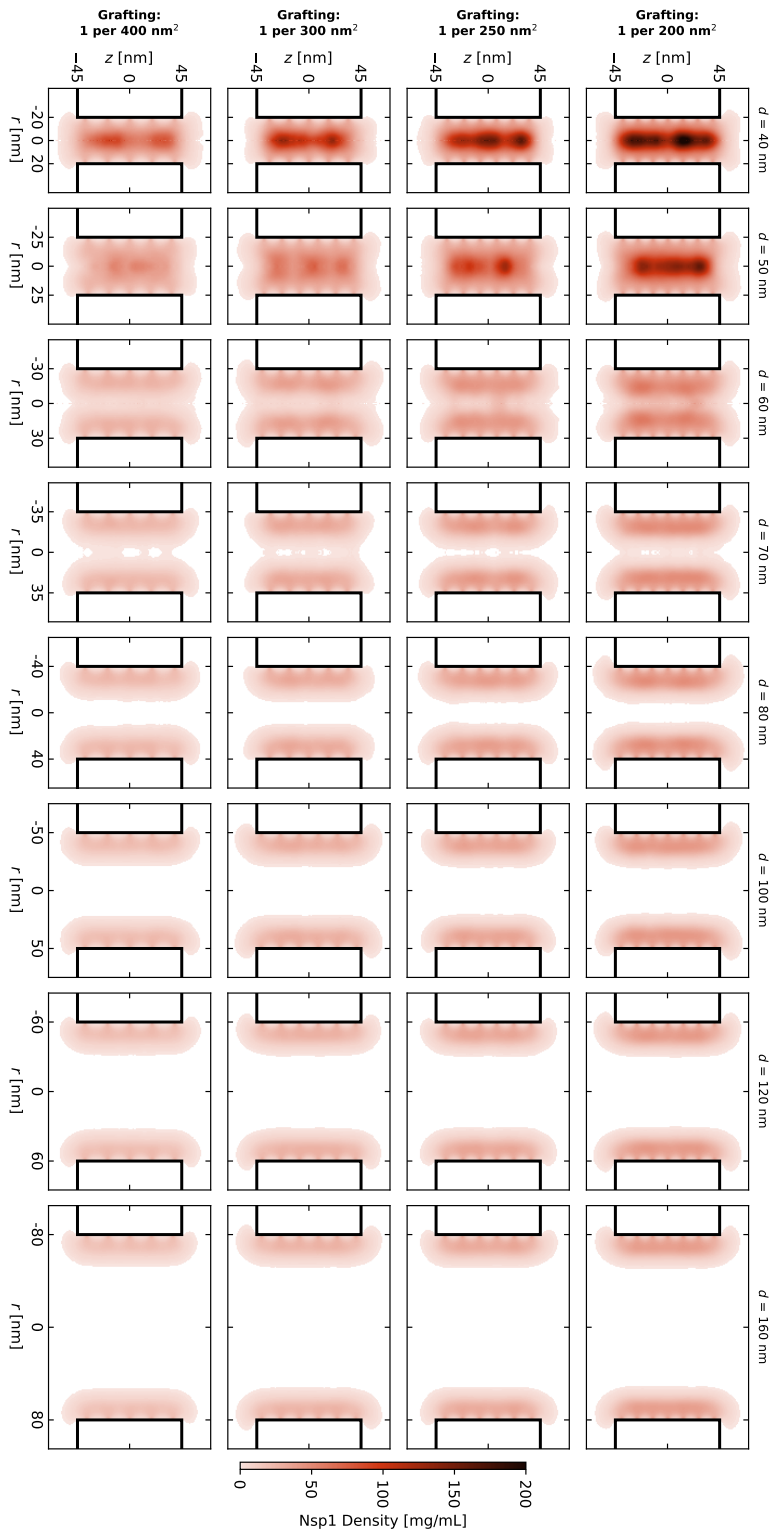
Dependence of selectivity on grafting density



Appendix 10—figure 3. Effect of grafting density on the selectivity of Nsp1 pores. (A) Calculated BSA event rates for Nsp1 pores for various grafting densities. (B) Zoom-in of A. (C) Apparent selectivity versus pore diameter, where the selectivity is calculated as the ratio of Kap95 to BSA event rates. For Kap95 we assumed that the event rate is the same for open pores and Nsp1 pores.

1609

Nsp1 density distributions



1610

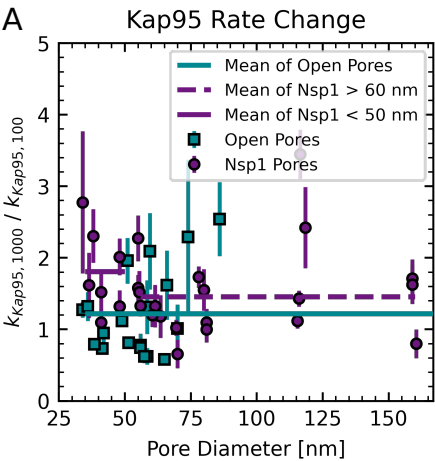
1611 **Appendix 10—figure 4.** Time-averaged r - z density distribution of Nsp1-coated nanopores
1612 for various diameters and grafting densities. Although there is a significant variation in the
1613 central channel densities for small diameter pores, the range of diameters at which the
1614 structural transition of the Nsp1 mesh takes place is largely independent of the Nsp1
1615 grafting density in the range that was tested.

1617

Appendix 11

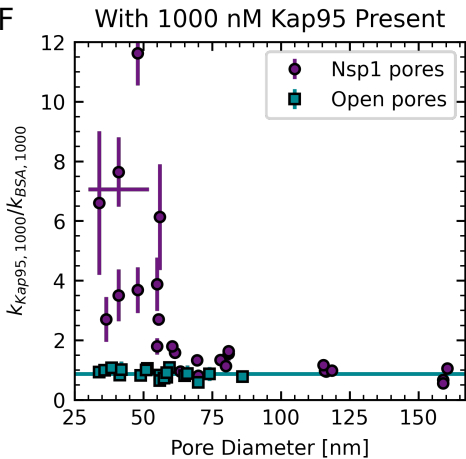
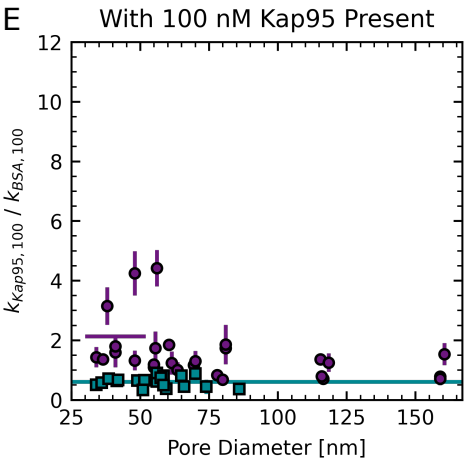
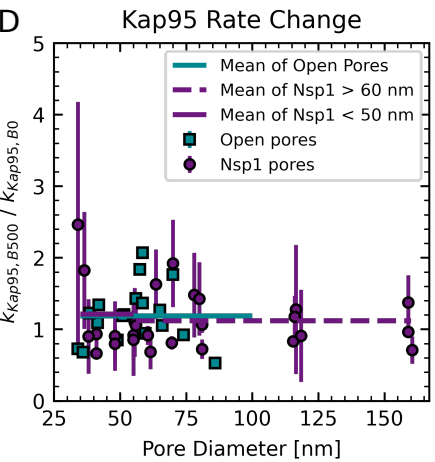
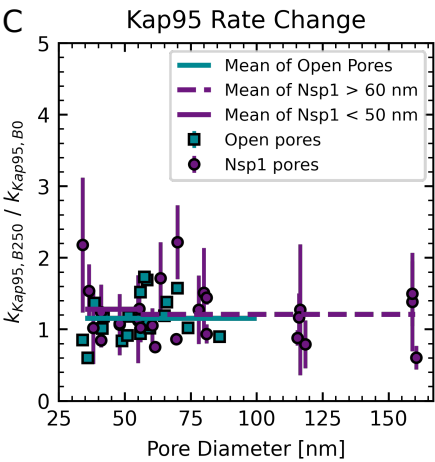
1618

Kap95 rate change



B

	Open Pores	Small Nsp1	Large Nsp1
$k_{Kap95,1000} / k_{Kap95,100}$	1.2 ± 0.1	1.8 ± 0.2	1.5 ± 0.2
$k_{Kap95,B100} / k_{Kap95,B0}$	1.2 ± 0.1	1.3 ± 0.2	1.2 ± 0.1
$k_{Kap95,B1000} / k_{Kap95,B0}$	1.2 ± 0.1	1.2 ± 0.3	1.1 ± 0.1
$k_{Kap95,100} / k_{BSA,100}$	0.61 ± 0.04	2.1 ± 0.4	
$k_{Kap95,1000} / k_{BSA,1000}$	0.87 ± 0.03	7.1 ± 1.6	



1619

Appendix 11—figure 1. (A) Rate change of Kap95 vs. pore diameter. Event rate of Kap95 at 1000 nM ($k_{\text{Kap95},1000}$) divided by the Kap95 event rate at 100 nM ($k_{\text{Kap95},100}$). At high Kap95 concentrations there is an increase in normalized event rate for both open and Nsp1 pores. It is largest for small Nsp1 pores. (B) The averages indicated in the plots by horizontal lines given with standard deviation estimated from fitting horizontal lines. (C,D) Influence of BSA concentration on Kap95 event rate. When dividing the Kap95 event rate with 250 nM of BSA being present $k_{\text{Kap95},\text{BSA}250}$ by the Kap95 event rate with 0 nM of BSA being present $k_{\text{Kap95},\text{BSA}0}$ (C) this shows that the Kap95 event rate is barely influenced by the presence of BSA, as expected. The same holds for the Kap95 event rate change with 500 nM of BSA to 0 nM being present. (E,F) Selectivity vs. pore diameter for different Kap95 concentrations. When switching from 100 nM of Kap95 to 1000 nM of Kap95, the selectivity of small Nsp1 pores increases by a factor of 3, whereas the selectivity of large pore decreases.

Model for the residual selectivity of large pores

The model as presented in **Figure 6** is based on the assumption a pore is occupied by two separate cross-sectional areas, a selective area and an unselective area, whereas no assumption over their location (such as a ring) is made. The full cross-sectional area A is thus divided as

$$A = A_{\text{open}} + A_{\text{Nsp1}}, \quad (17)$$

where A_{open} is the open (unselective pore area) and A_{Nsp1} is the selective (Nsp1-filled) area. Here, the selectivity S of a pore is defined as the ratio of Kap95 and BSA rates

$$S = \frac{k_{\text{Kap95}}}{k_{\text{BSA}}}, \quad (18)$$

which can be expressed in terms of the contributions of the two phases as

$$S = \frac{A_{\text{Nsp1}} l_{\text{Kap95}}^{\text{Nsp1}} + A_{\text{open}} l_{\text{Kap95}}^{\text{open}}}{A_{\text{Nsp1}} l_{\text{BSA}}^{\text{Nsp1}} + A_{\text{open}} l_{\text{BSA}}^{\text{open}}}, \quad (19)$$

where $l_{\text{protein}}^{\text{phase}}$ is the area normalized event rate constant for the respective protein in the different phases, i.e, open or Nsp1-filled.

Since we found experimentally the Kap95 event rates were unchanged by the presence of Nsp1, we approximate $l_{\text{Kap95}} \approx l_{\text{Kap95}}^{\text{open}} \approx l_{\text{Kap95}}^{\text{Nsp1}}$. The selectivity of a mixed phase pore is then given by:

$$S = \frac{l_{\text{Kap95}}}{l_{\text{BSA}}^{\text{Nsp1}} \frac{A_{\text{Nsp1}}}{A} + l_{\text{BSA}}^{\text{open}} \frac{A_{\text{open}}}{A}} = \frac{1}{\frac{l_{\text{BSA}}^{\text{Nsp1}}}{l_{\text{Kap95}}} \frac{A_{\text{Nsp1}}}{A} + \frac{l_{\text{BSA}}^{\text{open}}}{l_{\text{Kap95}}} \frac{A_{\text{open}}}{A}} = \frac{1}{\frac{1}{S_{\text{Nsp1}}} \frac{A_{\text{Nsp1}}}{A} + \frac{1}{S_{\text{open}}} \frac{A_{\text{open}}}{A}} \quad (20)$$

Note that this corresponds to the harmonic mean of the selectivities.

When considering the structure of the pore, the number of Nsp1 molecules in the pore is determined by the grafting density σ , the pore's radius r and length L as

$$N = 2\pi r\sigma L. \quad (21)$$

If we assume that each Nsp1 molecule renders a certain volume V selective, the effectively selective cross-sectional area can be calculated from the selective volume V_{Nsp1} as:

$$A_{\text{Nsp1}} = \frac{V_{\text{Nsp1}}}{L} = \frac{NV}{L} = 2\pi r\sigma V. \quad (22)$$

Thus, the selective area fraction depends on the pore radius as:

$$\frac{A_{\text{Nsp1}}}{A} = \frac{2\pi r}{\pi r^2} \sigma V = \frac{2}{r} \sigma V, \quad (23)$$

Combining both expressions for the selective area fraction, we obtain:

$$S = \frac{1}{\frac{1}{S_{\text{Nsp1}}} \frac{2}{r} \sigma V + \frac{1}{S_{\text{open}}} \left(1 - \frac{2}{r} \sigma V\right)} \quad (24)$$

where σV is the only fit parameter that we fit to the selectivities measured in **Figure 6**.

Note that, if each Nsp1 molecule occupies the same volume V , the rim thickness would depend on the pore radius and the ring thickness h can be calculated using $A_{\text{Nsp1}} = \pi r^2 - \pi (r - h)^2$ as:

$$h = r - \sqrt{r^2 - 2r\sigma V}, \quad (25)$$

which requires $\sigma V < \frac{r}{2}$. For flat surfaces, where $r \rightarrow \infty$ the parameter $\sigma V \rightarrow h$ and σV can be represents the Nsp1 layer height in these cases. In the case of curved surfaces, the layer height needs to be calculated using **Equation 25**. Notably, the assumption of constant volume that is applied here remains valid for situations where the Nsp1 phase is not localized in the rim, e.g. forming a central plug but is in contrast to previous models that assume a selective area (of whatever shape) similar in size to a ring of constant thickness, such as proposed by **Kowalczyk et al. (2011)**.

Appendix 12

Nsp1

The sequence of the Nsp1 used in this study was: MHHHHHHHHHHGSGENLYFQGT
SMGNFNTPPQNKTPFSFGTANNNSNTTNQNSSTGAGAFGTGQSTFGFNNSAPNNTNNA
NSSITPAFGSNNTGNTAFGNSNPTSNVFGSNSTTNTFGSNSAGTSLFGSSSAQQTksNGT
AGGNTFGSSSLFNNSTNSNTTKPAFGGLNFGGNNTPSSTGNANTSNNLFGATANANKP
AFSFGATTNDDKKTEPDKPAFSFNSSVGNKTDAPTTGFSFGSQLGGNKTVNEAAKPSLSF
GSGSAGANPAGASQPEPTTNEPAKPAISFGTATSDNKTTNTTPSFSFGAKSDENKAGATSKP
AFSFGAKPEEKKDDNSSKPAFSFGAKSNEDKQDGTAKPAFSFGAKPAEKNNNETSKPAFSFG
AKSDEKKDGDASKPAFSFGAKPDENKASATSKPAFSFGAKPEEKKDDNSSKPAFSFGAKSNE
DKQDGTAKPAFSFGAKPAEKNNNETSKPAFSFGAKSDEKKDGDASKPAFSFGAKSDEKKDS
DSSKPAFSFGTKSNEKKDSGSSKPAFSFGAKPDEKKNDEVSKPAFSFGAKANEEKESDESKSA
FSFGSKPTGKEEGDGAKAAISFGAKPEEQKSSDTSKPAFTFGAQKDNEKKTEC

Kap95

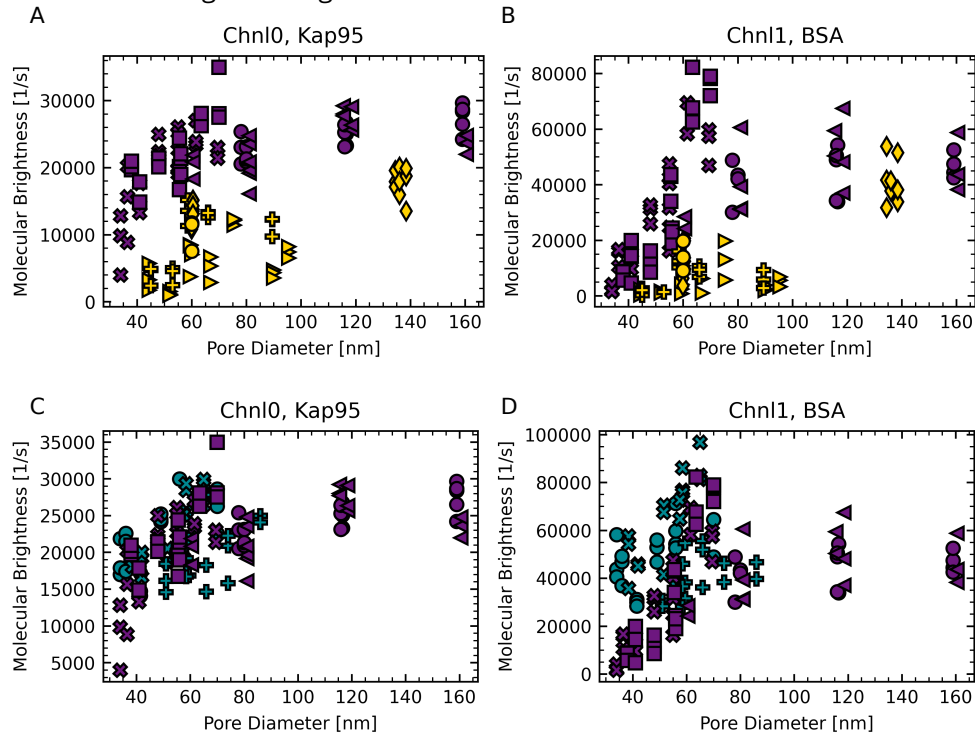
The sequence of the GST-3C-Kap95 before removal of the GST tag and before
labeling was: MSPILGYWKIKGLVQPTRLLLEYLEEKYEEHLYRDEGDKWRNKKFELGLEFP
NLPYYIDGDVKLTQSMARIYIADKHNMMLGGCPKERAISMLEGAVLDIRYGVSRAYSKDFT
LKVDFLSKLPEMLKMFEDRLCHKTYLNGDHVTHPDFMLYDALDVVLYMDPMCLDAFPKLV
CFKKRIEAIPIQIDKYLKSSKYIAWPLQGWQATFGGGDHPKSDLEVLFGQPASVGSMTAEF
AQLLENSILSPDQNI RL TSETQLKKLSNDNFLQFAGLSSQVLIDENTKLEGRILAALT LKNELVS
KDSVKTQQFAQRWITQVSPEAKNIKTNALTALVSI EPRIANAAAQLIAAIADIELPHGAWPEL
MKIMVDNTGAEQPENVKRASLLALGYMCESADPQSQUALVSSSNILIAIVQGAQSTETSKAV
RLAALNALADSLIFIKNNMEREGERNYLMQVCEATQAEDIEVQAAAFGCLCKIMSLYYTFM
KPYMEQALYALTIATMKSPNDKVASMTVEFWSTICEEII DIAYELAQFPQSPLQSYNFALSSIK
DVVPNLLNLLTRQNEDPEDDDWNVSMSAGACLQLFAQNCGNHILEPVLEFVEQNITADNW
RNREAAVMAFGSIMDGPDKVQRTYYVHQALPSILNLMNDQSLQVKETTAWCIGRIADSVAE
SIDPQQHLPGVVQACLIGLQDHPKVATNCSWTIINLVEQLAEATPSPIYNFY PALVDGLIGAA
NRIDNEFNARASAFSALTMMVEYATDTVAETSASISTFVMDKLGQTMSVDENQLTLEDAQSL
QELQSNILTVLAAVIRKSPSSVEPVADMLMGLFFRLLEKKDSAFIEDDVFYAISALAASLGKGFE
KYLETFSPYLLKALNQVDSPVSITAVGFIADISNSLEEDFRYS DAMMNVL AQMISNPNARRE
LKPAVLSVFGDIASNIGADFIPYLNDIMALCVAAQNTKPENGTL EALDYQIKVLEAVLDAYVGI
VAGLHDKPEALFPYVGTIFQFIAQVAEDPQLYSEDATSRAAVGLIGDIAAMFPDGSIKQFYGG
DWVIDYIKRTRSGQLFSQATKDTARWAREQQKRQLSLLPETGG

1728 After removal of the GST tag and sortase labeling the sequence of Kap95 as
1729 used during the experiment was:
1730 GPASVGSMSTAEFAQLLENSILSPDQNIRLTSETQLKKLSNDNFLQFAGLSSQVLIDENTK
1731 LEGRILAALTTLKNELVSKDSVKTQQFAQRWITQVSPEAKNQIKTNALTALVSIEPRIANAAAQL
1732 IAAIADIELPHGAWPELMKIMVDNTGAEQPENVKRASLLALGYMCESADPQSQUALVSSNNI
1733 LIAIVQGAQSTETSKAVRLAALNALADSLIFIKNNMEREGERNYLMQVVCEATQAEDIEVQAA
1734 AFGCLCKIMSLYYTFMKPYMEQALYALTIATMKSPNDKVASMTVEFWSTICEEEIDIAVELAQF
1735 PQSPLQSYNFALSSIKDVVPNLLNLLTRQNEDEDDWNVMSAGACLQLFAQNCGNHILE
1736 PVLEFVEQNITADNWRNREAAVMAFGSIMDGPDKVQRTYYVHQALPSILNLMNDQSLQVK
1737 ETTAWCIGRIADSVAESIDPQQHLPGVWQACLIQLDHPKVATNCSWTIINLVEQLAEATPSPI
1738 YNFYPALVDGLIGAANRIDNEFNARASAFSALTMMVEYATDTVAETSASISTFVMDKLGQTMS
1739 VDENQLTLEDAQSLQELQSNILTVLAAVIRKSPSSVEPVADMLMGLFFRLLEKKDSAFIEDDV
1740 YASALAASLGKGFKEYLETFSPLYLLKALNQVDSPPVSITAVGFIADISNSLEEDFRRYSDAMMN
1741 VLAQMISNPNARRELKPAVLSVFGDIASNIGADFIPYLNIDIMALCVAAQNTKPENGTLEAL
1742 DYQIKVLEAVLDAYVGIVAGLHDKPEALFPYVGTIFQFIAQVAEDPQLYSEDATSRAAVGLIG
1743 DIAAMFPDGSIKQFYGQDWVIDYIKRTRSGQLFSQATKDTARWAREQQKRQLSLLPETGG
1744 G-Alexa647

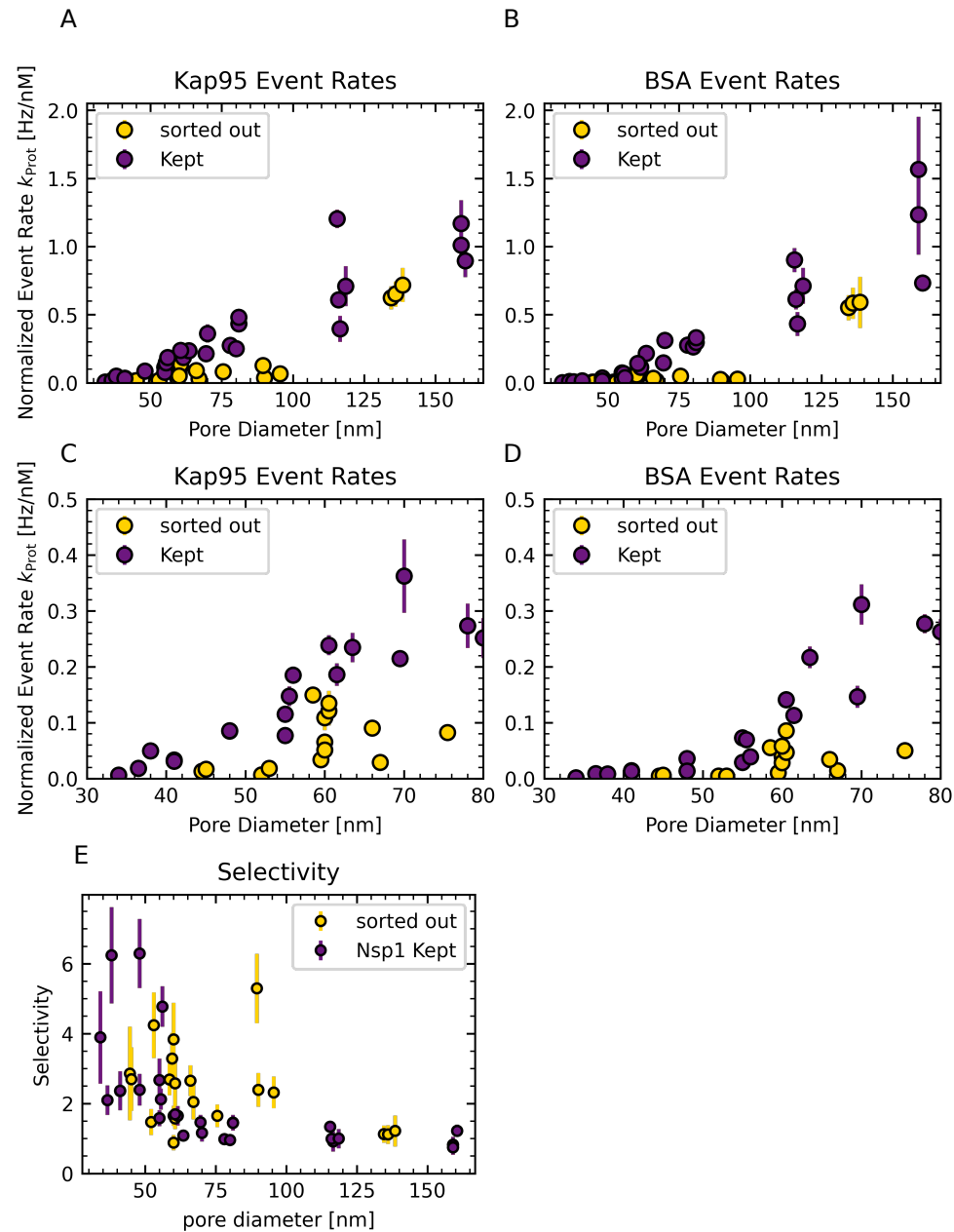
1745 **Appendix 13**

1746 **Data sanitation**

1747 As described in the methods section, some data sets were discarded due to a
1748 lower molecular brightness. In a plot of the molecular brightness against the
1749 pore diameter, these datasets were clearly identified as outliers (yellow markers in
1750 panels A and B of **Appendix 13- Figure 1**). We only used the molecular brightness
1751 of the Kap95 channel for discrimination because the low event rates for BSA at
1752 small pore diameters render the molecular brightness estimate unreliable. We
1753 additionally find a dependence of the molecular brightness on the pore diameter
1754 both for Nsp1-coated open pores, with a reduction of the molecular brightness at
1755 smaller pore diameters (panels C and D of **Appendix 13—Figure 1**). This effect was
1756 most evident for BSA in Nsp1-coated pores where event rates were low, where it
1757 most likely originates from a reduction of the correlation amplitude due to a larger
1758 contribution of background signal.



Appendix 13—figure 1. (A,B) Molecular brightness per time trace versus pore diameter on Nsp1 pores. We see two populations for Kap95, labeled in purple and yellow. The yellow data sets showed a decreased molecular brightness and therefore these data sets were removed from further analysis. (C,D) Comparison of molecular brightness between Open Pores (cyan) and Nsp1 pores (purple). For Kap95 there is barely any difference of distribution visible. For BSA there is a decrease observed in molecular brightness for small pores of Nsp1. This can be explained by the lower event rate in these pores. Different markers show different experiments.



Appendix 13—figure 2. (A,B) Event rates of discarded pores of Nsp1. For completeness, we show the event rates of pores that were not further considered in the analysis (yellow) due to their lower molecular brightness, as shown in the previous figure. As expected, these pores show a much decreased normalized event rate both for Kap95 and BSA compared to the Nsp1 pores that were kept in the analysis (purple). (C,D) Zoom in of (A,B). (E) Selectivity of discarded pores. The selectivity of discarded pores (yellow) deviates from the selectivity of the kept pores (purple). This can be explained when taking into account that a changed molecular brightness influences the event detection in each channel differently.